THESIS FOR THE DEGREE OF DOCTOR OF PHILOSOPHY

Determination of the Polaron Density in Chemically Doped Conjugated Polymers

EMMY JÄRSVALL

Department of Chemistry and Chemical Engineering

CHALMERS UNIVERSITY OF TECHNOLOGY

Göteborg, Sweden, 2024

Determination of the Polaron Density in Chemically Doped Conjugated Polymers

EMMY JÄRSVALL

ISBN 978-91-8103-018-1

Doktorsavhandlingar vid Chalmers tekniska högskola

Ny serie nr 5476

ISSN 0346-718X

Department of Chemistry and Chemical Engineering

Chalmers University of Technology

SE-41296 Göteborg

Sweden

Telephone: +46 (0)31 772 1000

Cover:
Polarons Unveiled: Navigating the Intricate Terrain of Conjugated Polymer Realms.

The cover was designed by Mariza Mone.

Chalmers Digitaltryck

Göteborg, Sweden 2024

Determination of the Polaron Density in Chemically Doped Conjugated Polymers

EMMY JÄRSVALL

Department of Chemistry and Chemical Engineering

Chalmers University of Technology

ABSTRACT

Semiconductors have become indispensable in modern electronics, playing vital roles across diverse devices such as computers, mobile phones, and solar cells. While inorganic semiconductors, such as silicon, currently dominates the industry, organic semiconductors offer promising alternatives. One of the most widely studied classes of organic semiconductors is conjugated polymers. Chemical doping is a critical tool that allows to tune their electrical conductivity through the introduction of positive or negative charge carriers, i.e. polarons, by the addition of dopants. The ability to adjust the polaron density is essential, as devices that employ conjugated polymers operate within distinct ranges of charge-carrier concentration. Therefore, accurately measuring and quantifying the number of polarons is paramount for both material development and device engineering.

This thesis explores methods for measuring the polaron density in the high doping regime. The results suggest that optical methods can be used to effectively estimate the polaron density in chemically doped conjugated polymers. The methodology is then used to demonstrate that chemical doping significantly effects the mechanical and rheological properties of conjugated polymers. Furthermore, it is found that the concept of double doping, which involves the transfer of two electrons between the polymer and the dopant molecule, is a generic concept that extends beyond quinodimethane-type dopants. The concepts elucidated in this thesis aid the development of an in-depth understanding of structure-property relationships relevant for doped conjugated polymers. Through addressing fundamental questions and establishing a foundation for future inquiry, this thesis contributes to the ongoing advancement of the dynamic field of organic electronics.

Keywords: organic semiconductors, conjugated polymers, chemical doping, molecular dopants polaron density, spectroscopy, double doping,

Nog finns det mål och mening i vår färd, men

det är vägen som är mödan värd.

– Karin Boye

ACKNOWLEDGEMENT

After many years at Chalmers, four as an undergraduate student and another four as a Ph.D. student, I have many people to thank who have supported me along the way.

Foremost, I would like to express my gratitude to my supervisor Christian Müller. Thank you for taking me on as a Ph.D. student and for all the support during these years.

I am equally grateful to Anja Lund, my co-supervisor during the initial stages of my Ph.D. Your support, both in academic and personal challenges, has been immensely appreciated.

To Anna Ström, my co-supervisor during the latter part of my studies, I extend heartfelt thanks. Your support during this period has been invaluable. Yet, beyond that I want to express my appreciation for your encouragement during my bachelor thesis and your recommendation for the startup job. These moments gave me confidence and made me believe in myself. Thank you.

My gratitude extends to the other amazing women who I had the privilege to work with before my Ph.D. studies: Patricia Lopez-Sanchez, and Jonna Hynynen. Your mentorship has been invaluable.

I extend warm thanks to Nina Kann for your encouragement and support during the writing process.

I extend my thanks to everyone at Chalmers with whom I had the privilege to collaborate closely: Renee K., for making that huge batch of polymer that I used for my thesis; Anna H., for all your help when I first started my PhD; Dorothea S., for all your support. I learnt a lot from you; Gustav P., for our excellent teamwork and for your patience explaining things; Mariavittoria C., for all the fun times in the processing lab and your constant kindness and assistance; Sandra H., your exceptional organizational skills and those delicious apple pies; Jian L., thank you for checking in on me and caring about how I was doing; Sri H. K. P., for being an outstanding fumehood mate and for sharing all those science memes; Joost K., for your expertise in the lab and the enjoyable hikes we had together; Sepideh Z., for being such a good team-mate. Our scientific discussions, whether in agreement or disagreement, have been incredibly enriching, and I learnt so much from you. On a personal level, I am deeply grateful for our friendship. Your support and that we can talk openly about anything have meant a great deal to me. And, of course, the story about the transformer will forever be etched in my memory.

Outside Chalmers, I am grateful for the collaborations with:
Till Biskup at Saarland University, for sharing your expertise on EPR and for the enjoyable research visit in 2019. Working with you has been a pleasure; Donghyun Kim and Igor Zozoulenko at Linköping University; Yadong Zhang, Stephen Barlow and Seth R. Marder at Georgia Institute of Technology; Dennis Derewjanko and Martijn Kemerink at Heidelberg University.

I want to thank my office mates for their support over the years:
Maria Q., your sense of humor always brightened my day, and thank you and for letting me adopt your office dog.; Lovisa K., thank you for your caring advice, your drive, and for keeping the office stocked with snacks.; Judith P. T., your humor and fun facts made work enjoyable, and your encouragement got me to the gym. Thanks!

Special thanks to the members of the Müller group, Anna P, Amin, Amir, Ida, Jan, Judy, Manta, Przemyslaw, Sozan, Veronica, Youngseok, Zerui, Zijin, for contributing to a vibrant and enriching research environment.

I am deeply grateful to the people on floor 8. A special thanks to Lotta for your continuous care and effort in encouraging the fantastic working atmosphere on our floor. I'd also like to extend my appreciation to everyone else on the 8th floor: Monika, Lidya, Krzysztof, Zewdeneh, Jessica V. M., Mathis, Megan, Alessia, Tadele, Hakan, Alexander G., Ranyella, Liang, Lorette, Alexandre H., Diego, Jessica O, Sara C, Sarah L., Xin, Anna A, Josue, Pablo, Helen, Adil, Jinhui, Qiaonan, Ulises M. R., Zhihang, Ulises M. C., Li, Jingnan, Pankaj, Guijun, Robson, Oscar, Jesika and everyone else who has been around during these years.

Shima G., thank you for all your support and your kindness. You always check in on how I am doing, and I love your impeccable fashion advice. You are a great friend, and it has been a pleasure being your “work wife”. Azadeh S., our chats in the lunchroom brightened my day, and I'm grateful for you always being there for me as a friend. Yingwei O., your humor, jokes, and memes (y tho) never failed to lift my spirits. I'll never forget the delicious pancakes you made for me every day when I was sick with Covid. Alicja S., your kindness and support have meant a lot to me. Mariza M., thank you for the enjoyable moments we shared in the lab and for creating the amazing cover for my thesis.

To my beloved family, I could never have done this without you. Från djupet av mitt hjärta, tack för ert stöd, er kärlek och uppmuntran.

Filip, thank you for your unconditional support and for believing in me. Du är mitt allt.

Thank you, everyone, for being part of this incredible journey.

NOMENCLATURE

A	Absorbance
B_0	Magnetic field
β	Bohr magneton
c	Concentration
CE	Counter electrode
CN	Cyano
CTC	Charge transfer complex
CW	Continuous wave
d	Thickness
DFT	Density functional theory
DOS	Density of states
EA	Electron affinity
E_C	Coulomb binding energy
E_g	Band gap
EPR	Electron paramagnetic resonance
ε_r	Dielectric constant
ε_0	Permittivity of vacuum
ε	Molar extinction coefficient
ΔE	Energy difference
F_2TCNQ	2,5-difluoro-7,7,8,8-tetracyanoquinodimethane
F_4TCNQ	2,3,5,6-tetrafluoro-7,7,8,8-tetracyanoquinodimethane
G'	storage modulus
g_e	Electron g-factor
h	constant
HOMO	Highest occupied molecular orbital
H-TFSI	bis(trifluoromethanesulfonyl)imide
I	Current
IE	Ionization energy
ICT	Integer charge transfer
IP	Ion pair
IR	Infrared

ITO	Indium tin oxide
l	Path length
LUMO	Lowest unoccupied molecular orbital
μ	Charge carrier mobility
Magic Blue	Tris(4-bromophenyl)ammoniumyl hexachloroantimonate
MIS	Metal-insulator-semiconductor
Mo(tfd-$COCF_3$)$_3$	Molybdenum tris[1-(trifluoromethylcarbonyl)-2-(trifluoromethyl)-ethane-1,2-dithiolene]
N_d	Number of dopant molecules
η_{diss}	Dissociation efficiency
η_{doping}	Doping efficiency
N_{free}	Number of free charges
η_{ion}	Ionization efficiency
NMR	Nuclear magnetic resonance
N_v	Number of charge carriers
v	Stretching vibrations
OFET	Organic field effect transistor
OLED	Organic light emitting diode
OTE	Organic thermoelectric
$P(\Theta)$	Carrier density
P3HT	Poly(3-hexylthiophene)
PDPP-3T	Poly{2,2′-[(2,5-bis(2-hexyldecyl)-3,6-dioxo-2,3,5,6-tetrahydropyrrolo[3,4-c]pyrrole-1,4-diyl)dithiophene]-5,5′-diyl-alt-thiophen-2,5-diyl}
p($g_4$2T-T)	Poly(2,5-bis(4-(tetraethylene glycol monomethyl ether)thiophen-2-yl)thiophene)
q	Elementary charge
Q	Number of injected charges
r	Coulomb binding radius
RE	Reference electrode
S_N	Site density
σ	Electrical conductivity
t	Time
THz	Terahertz
TQ1	Poly[[2,3-bis(3-octyloxyphenyl)-5,8-quinoxalinediyl]-2,5-thiophenediyl]

Θ	Polaron mole fraction
UV	Ultraviolet
V_{Ave}	Average site volume
V_S	Polymer site volume
v	Frequency of radiation
Vis	Visual
WE	Working electrode

PUBLICATIONS

This thesis consists of an extended summary of the following appended papers:

Paper I **Chemical Doping of Conjugated Polymers with the Strong Oxidant Magic blue**

Anna I. Hofmann, Renee Kroon, Sepideh Zokaei, Emmy Järsvall, Claudia Malacrida, Sabine Ludwigs, Till Biskup, and Christian Müller

Advanced Electronic Materials, **2020**, *6*, 202000249

Paper II **Tuning of the elastic modulus of a soft polythiophene through molecular doping**

Sepideh Zokaei,[†] Donghyun Kim,[†] Emmy Järsvall,[†] Abigail M. Fenton, Albree R. Weisen, Sandra Hultmark, Phong H. Nguyen, Amanda M. Matheson, Anja Lund, Renee Kroon, Michael L. Chabinyc, Enrique D. Gomez, Igor Zozoulenko and Christian Müller

[†] equal contribution

Materials Horizon, **2022,** *9*, 433-443

Paper III **Double doping of a low-ionization energy polythiophene with a molybdenum dithiolene complex**

Emmy Järsvall, Till Biskup, Yadong Zhang, Renee Kroon, Stephen Barlow, Seth R. Marder and Christian Müller

Chemistry of Materials, **2022***, 34*, 5673-5679

Paper IV **Visualisation of individual dopants in a conjugated polymer: sub-nanometre 3D spatial distribution and correlation with electrical properties**

Gustav Persson, Emmy Järsvall, Magnus Röding, Renee Kroon, Yadong Zhang, Stephen Barlow, Seth R. Marder, Christian Müller and Eva Olsson

Nanoscale, **2022***, 14*, 15404

Paper V **Delocalization enhances conductivity at high doping concentrations**

Dennis Derewjanko, Dorothea Scheunemann, Emmy Järsvall, Anna I. Hofmann, Christian Müller and Martijn Kemerink,

Advanced Functional Materials, **2022**, 202112262

Paper VI **Impact of oxidation-induced ordering on the electrical and mechanical properties of a polythiophene co-processed with bistriflimidic acid**

Sandra Hultmark, Mariavittoria Craighero, Sepideh Zokaei, Donghyun Kim, Emmy Järsvall, Furqan Farooqi, Sara Marina, Renee Kroon, Jaime Martin, Igor Zozoulenko and Christian

Journal of Materials Chemistry C, **2023***, 11*, 8091

CONTRIBUTION REPORT

Paper I — Co-author. Preparation of samples for comparison of optical and electron paramagnetic resonance measurements. A.H. and C. Müller. Planned the study and wrote the manuscript. A.H., C.M. and S.L performed spectro-electrochemical chronoamperometric measurements. T.B carried out EPR spectroscopy. A.H. and R.K. synthesized the polymers PDPP-TT and PDPP-ene. A.H. and S.Z. carried out chemical doping and electrical characterization.

Paper II — Shared main author. Carried out optical spectroscopy, electrical characterization and determined the oxidation level. A. F., A. W. and E. D. G. carried out oscillatory shear rheometric measurements. S. Z. and A. L. carried out thermomechanical analysis and WAXS characterization. S. H. carried out fast scanning calorimetry measurements. P. N. and M. C. carried out the GIWAXS characterization. D. K. and I. Z. carried out molecular dynamics simulations. R. K. synthesized the polymer. S. Z. and C. M planned the study and wrote the manuscript. All authors read and commented on the manuscript.

Paper III — Main author. Carried out sample fabrication, optical spectroscopy, electrical measurements, data analysis and estimation of ionization efficiency. Planned the study and wrote the manuscript together with C.M. EPR spectroscopy was carried out by T.B. R.K. synthesized the polymer p($g_4$2T-T). Y.Z., S.B. and S.M. synthesized the dopant species.

Paper IV — Co-author. Carried out the sample fabrication and performed the optical and electrical analysis. G.P. and E.O. conceived the study, performed the STEM and electron tomography experiments and analyses, contributed to the sample fabrication, and wrote the manuscript. M.R. performed the quantitative data analysis. R.K. synthesized the polymer. Y.Z., S.B. and S.M. synthesized the dopant species.

Paper V — Co-author. Collecting experimental data pertaining to conductivity in relation to charge density. Optical spectroscopy, determination of oxidation level and electrical characterization. D.D. and D.S. performed the modelling and wrote the manuscript supervised by M.K.. Spectro-electrochemistry and chronoamperometry was performed by A.H.

Paper VI — Co-author. Carried out optical spectroscopy and determination of oxidation level. S.H. carried out thermal analysis with FSC and DSC and wrote the manuscript together with M.C. and S.Z. supervised by C.M.. M.C. and S.Z. carried out electrical and mechanical measurements. D.K. and I.Z. carried out molecular dynamics simulations and S.M and J.M. carried out GIWAXS measurements. R.K. synthesized the polymer.

The author has published the following papers which are not included in the thesis:

Paper 7 **Enhanced Thermoelectric Power Factor of Tensile Drawn Poly(3-hexylthiophene)**

Jonna Hynynen, Emmy Järsvall, Renee Kroon, Yadong Zhang, Stephen Barlow, Seth R. Marder, Martijn Kemerink, Anja Lund, and Christian Müller

ASC Macro Letters, **2019***,* 8*, 70-76*

Paper 8 **Charge transport in doped conjugated polymers for organic thermoelectrics**

Dorothea Scheunemann, Emmy Järsvall, Jian Liu, Davide Beretta, Simone Fabiano, Mario Caironi, Martijn Kemerink, and Christian Müller

Chemical Physics Reviews, **2022**, 3, 021309

Paper 9 **Hexanary blends: a strategy towards thermally stable organic photovoltaics**

Sri Harish Kumar Paleti, Sandra Hultmark, Jianhua Han, YuanfanWen, Han Xu, Si Chen, Emmy Järsvall, Ishita Jalan, Diego Rosas Villalva, Anirudh Sharma, Jafar. I. Khan, Ellen Moons, Ruipeng Li, Liyang Yu, Julien Gorenflot, Frédéric Laquai, Christian Müller and Derya Baran

Nature Communications, **2023**, 14, 4608

Paper 10 **Electrically Programmed Doping Gradients Optimize the Thermoelectric Power Factor of a Conjugated Polymer**

Jian Liu, Mariavittoria Craighero, Vandna K. Gupta, Dorothea Scheunemann, Sri Harish Kumar Paleti, Emmy Järsvall, Youngseok Kim, Kai Xu, Juan Sebastián Reparaz, L. Jan Anton Koster, Mariano Campoy-Quiles, Martijn Kemerink, Anna Martinelli, and Christian Müller

Advanced Functional Materials, **2024**, 2312549

TABLE OF CONTENT

Chapter 1

INTRODUCTION

Semiconductors have evolved into integral materials of modern electronics, serving as ubiquitous elements in daily life. They form the foundational building blocks of transistors utilized in a wide array of applications, including computers, mobile phones, light-emitting diodes (LEDs), and solar cells. Presently, the manufacturing of electronic devices predominantly relies on inorganic semiconductors like silicon or gallium arsenide. However, organic semiconductors have emerged as a promising alternative to conventional inorganic materials. This shift is attributed to their favorable characteristics, which encompass solution processability, mechanical flexibility, and cost-effectiveness.

In the mid-1970s, Alan J. Heeger, Alan G. MacDiarmid, and Hideki Shirakawa discovered that doping of polyacetylene with iodine vapor led to metal-like conductivities, generating significant interest in organic semiconductors. This breakthrough later earned them the Nobel Prize in Chemistry for their work on conductive polymers.[1, 2] Today, organic electronics find applications in various fields such as energy harvesting, energy storage and lighting to bioelectronics, with organic light emitting diodes (OLEDs) being a notable example used for example in smartphone displays.[3, 4]

Organic semiconductors encompass small molecules or polymers with the ability to conduct electricity. This thesis will focus on polymeric semiconductors, i.e. conjugated polymers (Section 1.1), featuring extended π-conjugated systems along their backbones. Chemical doping (Chapter 2) serves as a valuable tool to tune the electrical conductivity of organic semiconductors through the introduction of positive or negative charge carriers, i.e. polarons, by the addition of dopants. The ability to tune charge carrier concentration per unit volume is essential, as devices that employ conjugated polymers operate within distinct ranges of charge carrier density (Fig. 1.1).

Thin-film devices, including organic light emitting diodes (OLEDs), organic photovoltaics (OPVs) and organic field-effect transistors (OFETs), utilize conjugated polymers. In OLEDs and OPV devices, the charge-carrier density typically reaches values of 10^{21} to 10^{23} m^{-3}.[5] OFETs on the other hand, reach higher values, ranging from 10^{23} to 10^{25} m^{-3}.[6] Bulk devices such as organic thermoelectric (OTE) generators employ conjugated polymers with much higher charge-carrier densities in the range of

10^{26} to 10^{27} m^{-3}, often achieved through chemical doping.[7] Other types of thin-film devices such as organic electrochemical transistors (OECTs), often exhibit a very high charge-carrier density of up to 10^{27} m^{-3} in their on state.[8]

Given that different applications operate at different carrier densities, the ability to tune the carrier density becomes crucial. Therefore, accurately measuring and quantifying the number of charges becomes paramount. While established techniques such as metal-insulator-semiconductor (MIS) and space charge-limited currents are suitable for low carrier densities (<10^{25} m^{-3}), emerging technologies require the capability to measure high carrier densities.[9]

This thesis explores methods for measuring high charge carrier concentrations, addressing the growing demand for defined measurement techniques in the field of organic semiconductors. The specific aims of this thesis are outlined in Section 4.6.

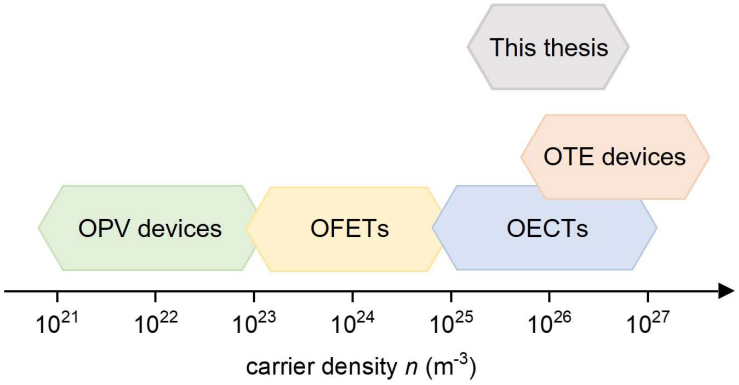

Figure 1.1. Approximate range of charge-carrier density *n* of organic photovoltaic (OPV) devices, organic field-effect transistors (OFETs), organic electrochemical transistors (OECTs) and organic thermoelectric (OTE) devices as well as the range of charge-carrier density studied in this thesis.

1.1 Conjugated polymers

Polymers are macromolecules, characterized by long chains composed of numerous repeating subunits linked by covalent bonds. Polymers are primarily known for their insulating properties, making them essential for various applications such as electrical insulation, e.g. as the protective coating of high voltage cables. However, not all polymers conform to the insulator stereotype. Conjugated polymers represent a fascinating class within this diverse group. Unlike their insulating

counterparts, conjugated polymers possess semiconducting properties resulting from π-conjugation. This unique feature arises from a backbone chain comprising alternating single and double bonds, creating overlapping π-orbitals along the chain. In this arrangement, π-electrons are delocalized throughout parts of the polymer backbone, rather than being part of one single valence bond. It is this overlap of π-orbitals that gives conjugated polymers their unique electrical characteristics.

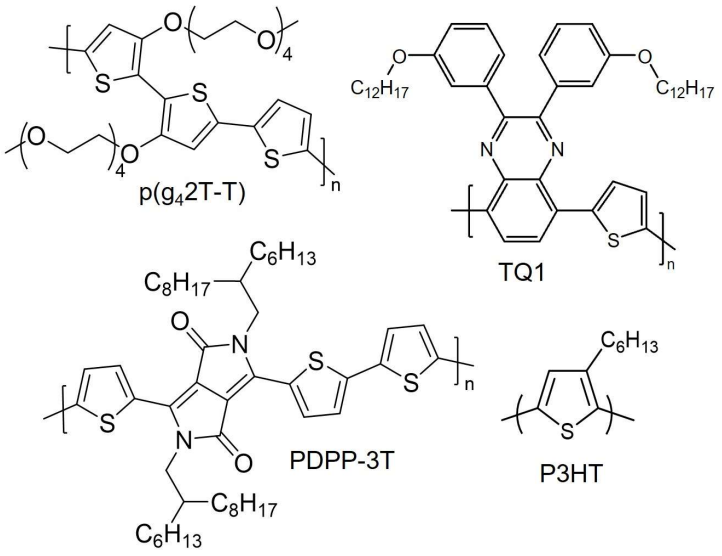

Figure 1.1. Chemical structure of conjugated polymers used in this thesis.

1.2 Energy levels and the density of states

In a conjugated small molecule like thiophene (the monomer shown in Figure 1.3a), the overlapping π-orbitals lead to the splitting of energy levels within the π-bonds, giving rise to the formation of bonding π-orbitals and an antibonding π*-orbitals referred to as the Highest Occupied Molecular Orbital (HOMO) and the Lowest Unoccupied Molecular Orbital (LUMO), respectively, as illustrated in Figure 1.3a. The energy difference between HOMO and LUMO is defined as the band gap (E_g). In the context of a single small molecule, the energy of the HOMO aligns well with the ionization energy (IE). The IE is defined as the energy needed in order to remove an electron from the molecule. Conversely, the energy of the LUMO corresponds to the electron affinity (EA), which represents the energy gained upon the addition of an electron to the molecule. However, as we join conjugated monomers like thiophene together through polymerization, the extension of the conjugated chain initiates the formation of new energy states with varying degree of bonding and antibonding character within the π- and π*-orbitals. This leads to the emergence of energy distributions of energy states often referred

to as the valence band and the conduction band. However, the energy landscape in conjugated polymers consist of discrete energy levels instead of bands.[10] In the following, these distributions of states will instead be referred to as the HOMO- and the LUMO manifold. The formation of new energy states also results in a pronounced convergence of the HOMO and LUMO, which effectively reduces the band gap. The resulting distribution of energy levels is termed the density of states (DOS), which provides insight into the number of energy levels within a defined region in energy space. Typically, a Gaussian function is used to show how the energy levels in the HOMO- and LUMO manifold are distributed. The central peak of the Gaussian function represents the mean energy level, while its standard deviation measures energy level dispersion. This DOS function offers a quantitative

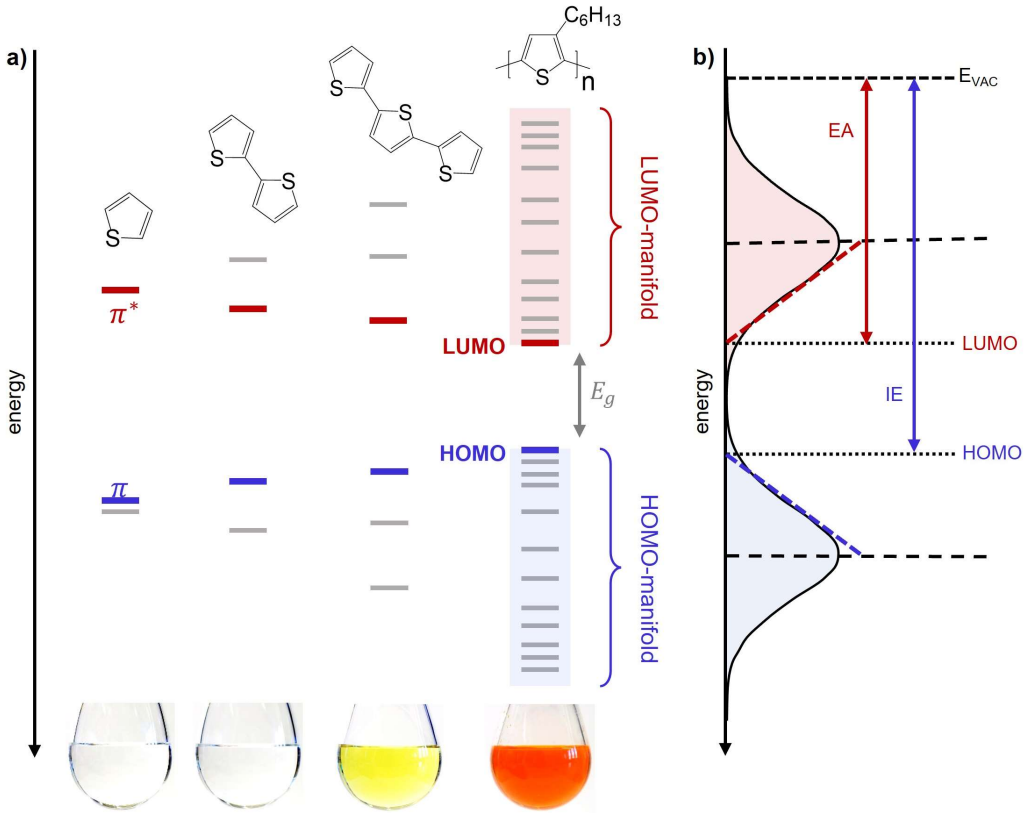

Figure 1.2. *a*) Evolution of the HOMO and LUMO levels as well as the bandgap E_g with increasing number of thiophene repeat units, resulting in valence and conduction bands for polythiophene. Reproduced from Ref. 11 with permission from the Royal Society of Chemistry. b) Gaussian approximation for the density of states (DOS) of a molecular solid. Two Gaussian distributions representing the occupied levels and the unoccupied levels. Adapted from Ref. 7.

representation of the available states within the system**,** and the standard deviation serves as a valuable metric for quantifying the disorder within the DOS, which indicates how broad the energy level distribution is. Using the Gaussian approximation of the DOS, the IE and EA can be estimated by drawing a line through the inflection point of the DOS curve with a y-axis intercept set at twice the standard deviation of the DOS from the DOS center as illustrated in Figure 1.3b. It is important to acknowledge that beyond the pronounced influence of increasing conjugation length, the disorder of the DOS is considerably influenced by an array of factors. These include the relative orientation of molecules (intermolecular effects), conformation, configuration, and the presence of chemical defects, each of which contributes to local variations in energy levels. Consequently, it is important to recognize that within a polymeric material the IE and EA may have distinct, localized values.[12] This perspective emphasizes the complexity of materials science in the context of molecules and polymeric systems.

1.3 Optical absorption of conjugated polymers

The band gap E_g is a critical parameter, significantly influencing the optical characteristics of conjugated polymers. Specifically, it determines the highest wavelength of light, i.e. the lowest energy, these materials can absorb. Absorption occurs when the energy of the incoming photons match or

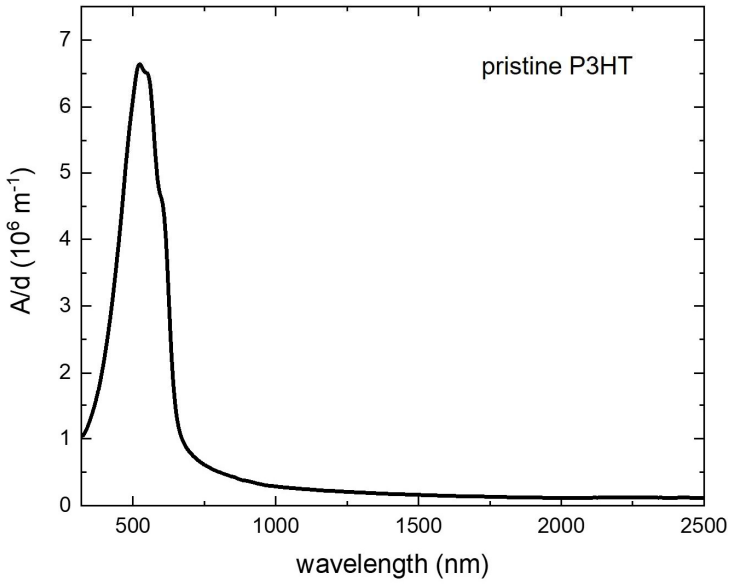

Figure 1.3. UV-vis-NIR absorption spectra showing the thickness normalized absorption (A/d) for pristine P3HT.

exceed the band gap, exciting an electron from a bonding to an antibonding orbital. As described in the previous section, the broadening of the DOS upon extension of the conjugation length of the polymer chain leads to a narrowing of the E_g.

Consequently, as the band gap becomes smaller, the polymer begins to absorb light with lower energy and will eventually absorb light in the visible spectrum, resulting in a colorful appearance (Fig. 1.3a). Typically, conjugated polymers feature band gaps ranging from 1.5 to 3 electronvolts (eV) which translates to wavelengths spanning from 800 to 400 nanometers.[13] In practical terms, it means these polymers absorb light in the visible spectrum and the nearby near-infrared region. This is illustrated in Figure 1.4 where an absorption spectrum of poly(3-hexylthiophene) (P3HT) is shown.

1.4 Semiconductors

A semiconductor is a material where the conductivity falls within the range between metals and insulators and in where the number of charge carries can be altered by external means.[14] The electrical conductivity (σ) is described by the formula below:

$$\sigma = N \cdot q \cdot \mu \qquad (1.1)$$

Here N represents the number of charge carriers, q stands for the charge of the carrier and μ is the charge carrier mobility. It is important to point out that the semiconducting characteristics of inorganic semiconductors such as silicon, germanium and GaAs differ from those of organic semiconductors, such as conjugated polymers. Conjugated polymers commonly feature a band gap between 1.5 and 3 eV.[15-18] This is considerably larger compared with a band gap <1.4 eV for conventional inorganic semiconductors.[13, 19] In the case of inorganic semiconductors, the creation of free charge carriers can occur through thermal excitation across the band gap at room temperature. However, the larger band of conjugated polymers prevents the creation of a substantial number of charge carriers by thermal excitation. Consequently, conjugated polymers lack intrinsic charge carriers. As stated in Equation 1.1, a low number of charge carriers results in low electrical conductivity. To enhance the electrical conductivity of conjugated polymers, the generation of charge carriers through external stimuli is necessary. This can be achieved either by the dissociation of photogenerated electron-hole pairs or by a process known as doping. The concept of doping will be explored in more detail in Chapter 2 and entails the introduction of either negative (n-type) charge carriers by the addition of electrons or positive (p-type) charge carriers by the removal electrons, ultimately resulting in the creation of holes.

Conjugated polymers typically exhibit a dielectric constant (ε_r) with a value around $\varepsilon_r \sim$ 3-4.[20] This is notably lower than the dielectric constant of inorganic semiconductors like silicon, where $\varepsilon_r \sim$ 11.[21]

The lower dielectric constant of conjugated polymers implies that Coulomb interactions have a significant impact, causing charge carriers to be more localized compared to inorganic semiconductors, owing to the lack of dielectric screening. The influence of Coulombic interactions will be discussed in further detail in Chapter 2. Due to the localized nature of the charge carriers, charge transport in conjugated polymers occurs through hopping transport, which compared to band transport, results in a lower charge carrier mobility and overall electrical conductivity which will be covered in Chapter 3.

Conjugated polymers offer distinct advantages compared to inorganic materials, such as mechanical flexibility, lightweight properties, and cost-effectiveness. Moreover, they are soluble in common solvents, allowing for processing through solution-based methods at low temperature like spin-coating and ink-jet printing. Conjugated polymers combine the advantageous electronic properties of semiconducting materials with the mechanical benefits of organic compounds. This makes them highly promising across a range of applications. These applications encompass thin-film devices such as OLEDs[3, 22-25], OFETs[26, 27], OECTs[28-30], and OPVs[31, 32], as well as bulk applications like OTEs[11, 33-36] and conducting fibers[37-40].

Chapter 2

CHEMICAL DOPING

Conjugated polymers lack intrinsic charge carriers. As a result, doping emerges as a powerful tool that allows tuning the charge carrier concentration within these materials. Doped conjugated polymers have found widespread applications, such as in organic photovoltaics, organic transistors, and sensors.[24-26, 41-50] Additionally, they are increasingly utilized in OTEs and have recently emerged in nanophotonics and plasmonics.[51-58] Chemical doping involves the addition of small molecules capable of undergoing charge transfer with the host material. This charge transfer results in the formation of polarons, which are radical cations (p-doping) or radical anions (n-doping) that delocalize over polymer segments representing a charge accompanied by an intramolecular distortion of the polymer backbone. Two prevailing mechanisms for achieving chemical doping are redox doping or acid/base doping. In redox doping, electron-donating or electron-accepting molecules are added to the conjugated polymer introducing either negative (n-type) charge carriers through the addition of electrons or positive (p-type) charge carriers, i.e. holes, through the removal of electrons (Fig. 2.2). In

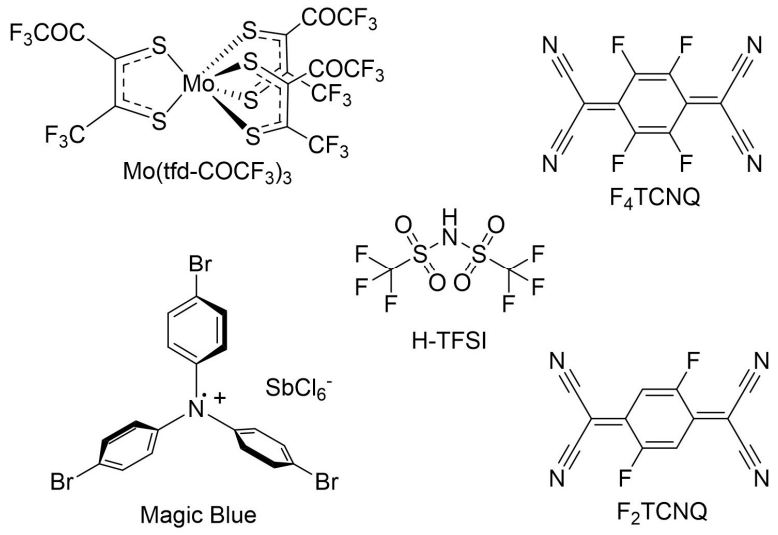

Figure 2.1. Chemical structure of p-dopants used in this thesis.

acid-base doping, a proton (H^+) or hydride (H^-) is transferred to the conjugated polymer backbone, resulting in p-doping or n-doping, respectively (Fig.2.2). This thesis primarily focuses on redox p-doping.

2.1 Redox doping

Redox doping entails a redox reaction where electrons are transferred between the dopant molecules and the polymer.[7, 10, 43, 55, 59] In case of n-doping, electrons are transferred from the dopant to the conjugated polymer, introducing negative (n-type) charge carriers. Conversely, for p-doping there is electron transfer from the polymer to the dopant, introducing positive (p-type) charge carriers, i.e. electron holes. Redox doping can also occur through the presence of atmospheric oxygen or water. In this case, the atmospheric oxygen or water can act as oxidizing agents (p-doping), or react with the dopant to first produce a radical that subsequently undergoes charge transfer with the polymer.[60-62] Dopants are selected based on their redox properties to facilitate electron transfer with the polymer. The charge transfer process between dopant and host can either be integer charge transfer (ICT) or partial charge transfer, the latter resulting in the formation of a charge transfer complex (CTC).

2.1.1 Integer charge transfer

In the case of ICT, there is electron transfer between the dopant and the conjugated polymer, resulting in the formation of a polaron on the polymer backbone which is counterbalanced by the oppositely charged dopant molecule. The polaron and the generated dopant counterion forms an ion pair (IP) that is Coulombically bound. IP formation occurs only if it is energetically favorable, determined by the energetic offset between the two materials. For p-doping, the polymer donates an electron from its HOMO to the LUMO of the (typically neutral) dopant, provided that the electron affinity of the dopant (EA_{dopant}) is equal to or higher than the ionization energy of the conjugated polymer ($IE_{polymer}$), i.e. $EA_{dopant} \geq IE_{polymer}$ (Fig. 2.2). For n-doping, the opposite scenario is required, where the electron affinity of the polymer ($EA_{polymer}$) should be equal to or greater than the ionization energy of the dopant (IE_{dopant}), i.e. $EA_{polymer} \geq IE_{dopant}$ (Fig. 2.2).

While many dopants are neutral species, charged species such as radical cation salts,[63, 64] like Magic Blue (Figure 2c), or radical anions[65] can be used to facilitate charge transfer provided that the energy levels involved in charge transfer is higher in energy or equal to $IE_{polymer}$ in case of p-doping. For n-doping the energy levels involved should be lower in energy or equal to $IE_{polymer}$ to facilitate charge transfer. For instance, in p-doping with a radical cation salt, the charge transfer occurs from the HOMO level of the polymer to the partially filled HOMO level of the radical cation.[63]

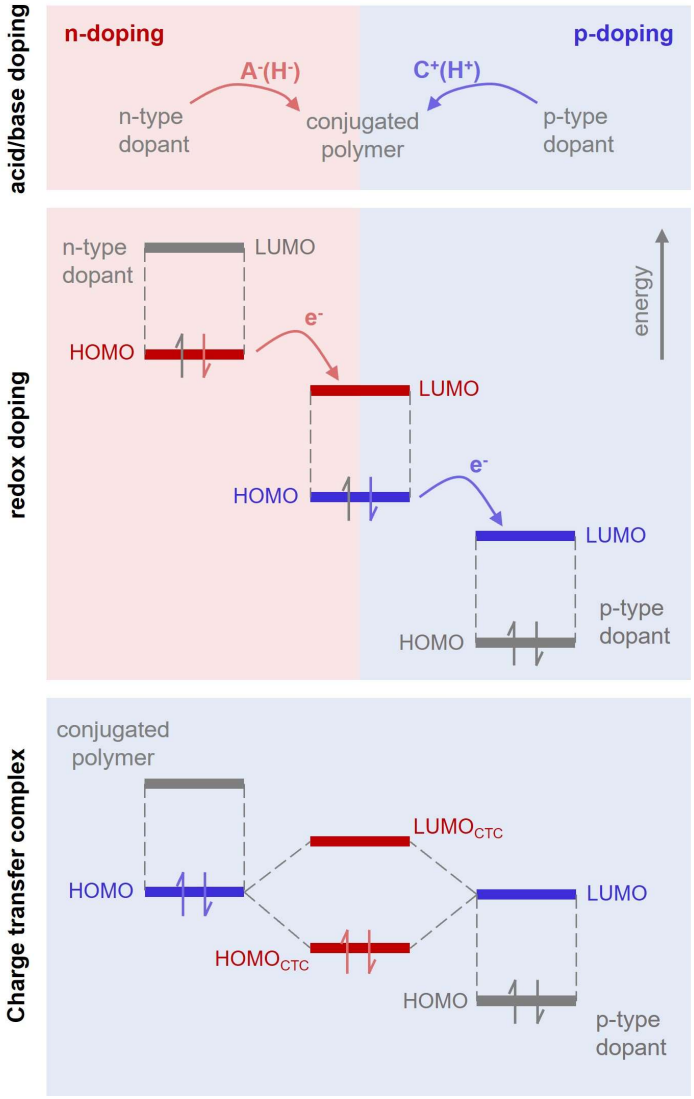

Figure 2.2. Basic principles of (a) acid/base-doping involving the transfer of a hydride(H^-) or a proton (H^+) to the conjugated polymer (b) redox doping involving the transfer of an electron (e^-) from the semiconductor HOMO to the dopant LUMO in case of p-doping; (c) the formation of a charge-transfer complex through fractional charge transfer. Reproduced from Ref. 11, with permission from Royal Society of Chemistry and from Ref. 51, Copyright 2022, A.P.

In some cases, charge transfer can take place between the polymer and the dopant, even if the energetic offset between EA and IE is not favorable. This is because these values are determined through cyclic voltammetry of both the polymer and the dopants dissolved in solution, and as a result, they can exhibit different values in their solid state. Furthermore, different parts within the same film

can have different energy levels. For instance, the IE is lower in the crystalline parts of a P3HT film compared to its amorphous regions.[66]

Furthermore, in specific conditions, double charge transfer can occur for certain polymer and dopant combinations, such as F_4TCNQ (Fig. 2.1) and polythiophenes with a low IE.[65] In this scenario, the initially neutral dopant molecule undergoes the initial exchange of an electron with the host, followed by subsequent exchange of a second electron between the generated counterion and another site within the host. It is important to keep in mind that the values for IE and EA are defined for neutral molecules. Nevertheless, for the sake of simplicity, the EA and IE of charged species are at times denoted as $EA^{+/-}$ and $IE^{+/-}$, where "-" designates the anionic state and "+" designates the cationic state, although this representation is not entirely correct.[7]

2.1.2 CTC formation

In instances of partial charge transfer, an overlap between donor and acceptor π-orbitals takes place, inducing hybridization of the frontier orbitals. This results in the formation of a CTC and the emergence of new local HOMO and LUMO states (Fig. 2.2). The newly formed local HOMO incorporates both electrons from the donor HOMO level, leading to fractional charge transfer between the polymer and the dopant. In this scenario, the charge is distributed between the polymer and dopant.[7, 51] The CTC is neutral and can undergo charge transfer with the polymer when thermally excited, although this process tends to be relatively inefficient.[67]

CTC formation can occur even when the electron affinity of the dopant is significantly smaller than the ionization energy of the polymer ($EA_{dopant} << IE_{polymer)}$, for p-type doping or if the ionization energy of the dopant is much greater than the electron affinity of the polymer ($EA_{polymer} << IE_{dopant}$) for n-type doping.[10] Additionally, CTCs can form even when the energy offset allows for ICT, and in specific circumstances, both ICT and CTC formation can occur simultaneously within the same system.[68] Predicting whether CTC formation will occur is hence a challenging task. To avoid CTC formation, bulkier dopants are sometimes preferred to reduce the π-overlap with the polymer orbitals.[7]

2.2 Acid/base doping by radical cations

Acid doping involves the transfer of a proton (H^+) from the dopant to the conjugated polymer backbone, resulting in p-doping (Fig. 2.2). The resulting net charge is redistributed via conjugation effects, and the corresponding anion enters the system to maintain charge neutrality.[69] In base doping, a hydride (H^-) is transferred to the conjugated polymer backbone, resulting in n-doping (Fig. 2.2).

2.3 Ionization

In the scenario of ICT, the polaron introduced to the polymer backbone is effectively counterbalanced by the oppositely charged dopant molecule, forming an ion pair that is coulombically bound (Fig. 2.3). The ionization efficiency, η_{ion}, of this process is expressed by the following equation:

$$\eta_{\text{ion}} = \frac{N_v}{N_d} \tag{2.1}$$

Here, N_d represents the number of dopant molecules per unit volume and N_v signifies the number of generated polarons. Determining N_d is typically straightforward when the dopant and host are co-processed, that is, processed from the same medium. In contrast, N_v can be estimated using various techniques, such as optical spectroscopy and electron paramagnetic resonance (EPR) spectroscopy, which will be further discussed in Chapter 4. If each dopant were to give rise to exactly one charge on the backbone, η_{ion} would be 100 %. However, not every introduced dopant molecule undergoes electron transfer, resulting in an ionization efficiency typically below 100%. Factors limiting η_{ion} include, for example, an unfavorable energetic offset between dopant and polymer or limited miscibility of the dopant and the host material, leading to dopant aggregation, resulting in reduced contact between the dopant and the host. In the case of double charge transfer, the same factors limit $\eta_{ion.}$ However, since in this case each dopant can give rise to two polarons, the maximum η_{ion} that can be achieved is 200 %.

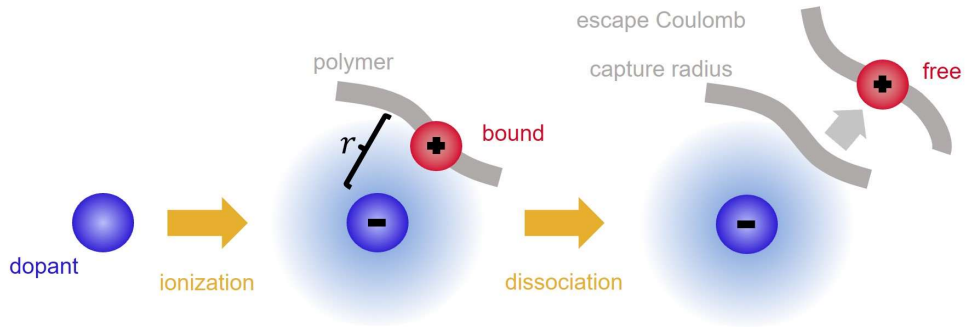

Figure 2.3. Schematic illustration of the two steps of a doping process. Reprinted with permission from Ref. 51, Copyright 2022, A.P.

2.4 Dissociation

For a polaron to contribute to charge transport, it must dissociate from the coulomb radius of the counterion to become a free charge (Fig. 2.3). The dissociation efficiency (η_{diss}) is described by the equation below:

$$\eta_{diss} = \frac{N_{free}}{N_v} \tag{2.2}$$

N_{free} represents the number of generated free charges. N_{free} can be studied through various techniques such as terahertz (THz) spectroscopy[70], ultrafast transient absorption spectroscopy[71, 72], admittance spectroscopy(X)[73-76], AC-Hall measurements[7, 77, 78] or with metal-insulator-semiconductor (MIS) devices[65, 79]. η_{diss} is typically much less than 100 % due to strong Coulomb interactions. To be able to dissociate from the ion pair, the polaron needs to escape the Coulomb binding exerted by the counterion. The Coulomb binding energy E_C is given by:

$$E_C(r) = \frac{q^2}{4\pi\varepsilon_0\varepsilon_r r} \tag{2.3}$$

Here, q is the elementary charge, ε_0 is the permittivity of vacuum, ε_r is the dielectric constant of the host and r is the distance between the polaron and the counterion.

2.5 Doping efficiency

Doping involves a two-step mechanism: ionization and dissociation. The doping efficiency (η_{doping}) is described by the combination of Equations 2.1 and 2.2:

$$\eta_{doping} = \eta_{ion} \times \eta_{diss} = \frac{N_{free}}{N_d} \tag{2.4}$$

Strategies, such as using large dopant molecules to increase the distance between the counterion and polaron, can reduce Coulomb binding. However, large dopants also occupy more space, limiting the volume for charge-conducting conjugated material and thus restricting polaron density. How the doping efficiency affects charge transport will be discussed in more detail in Chapter 3.

2.6 The density of states of doped conjugated polymers

Upon doping of conjugated polymers and the formation of a polaron on the polymer backbone, a new pair of bonding (π) and antibonding orbitals (π*) emerges in the band gap. According to the model proposed by Koch et. al.[80], in the context of p-doping, the removal of one electron induces a

downward shift of the HOMO- and LUMO-manifold (Fig. 2.4).[81] This shift is the consequence of the increased difficulty of removing a second electron from the same site, leading to an increase of the ionization energy (IE^+) of the charged site compared to the IE of the neutral site.[82] This increase in accessible energetic states directly influences the overall DOS, introducing an increased level of energetic disorder in the material. The polaron gives rise to two optical transitions in the material, the P1 and P2 transition. Both transitions start from the HOMO-manifold edge and lower lying occupied states. The P1 transition ends at the lower sub-bandgap state and higher lying unoccupied levels, whereas the P2 transition ends at the upper intra bandgap state and higher lying unoccupied levels.

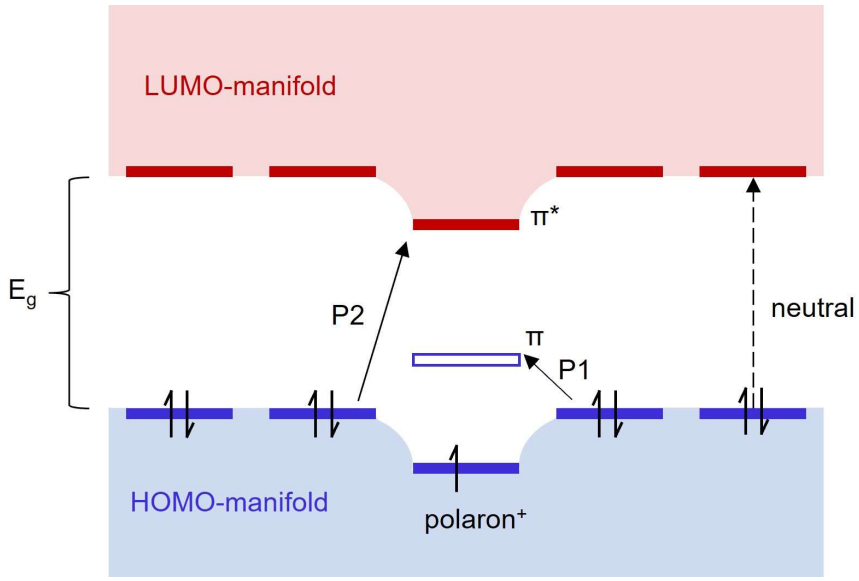

Figure 2.4. Energy diagram of a p-doped conjugated polymer depicting the optical transitions of the neutral polymer as well as the P1 and P2 polaron.

2.7 Optical absorption of doped polymers

As explored in the previous section, the generation of polarons through doping induces new optical transitions. These optical characteristics can be utilized for applications in various sensing scenarios, such as optical nanoantennas.[50, 56] The resulting optical transitions give rise to absorption features at lower energies compared to those of the neutral polymer. Figure 2.5 illustrates this phenomenon, depicting two distinct peaks emerging at higher wavelengths upon doping P3HT with the dopant Magic Blue (dopant structure presented Fig. 2.1) and at the same time the neutral peak is bleached. The P1 transition results in a broad peak arising in the far infrared, while the P2 transition produces a peak

close to the neutral peak but at slightly lower energy. These two peaks serve as characteristic features of the polaron, enabling both identification and quantification. At high charge concentrations, polarons

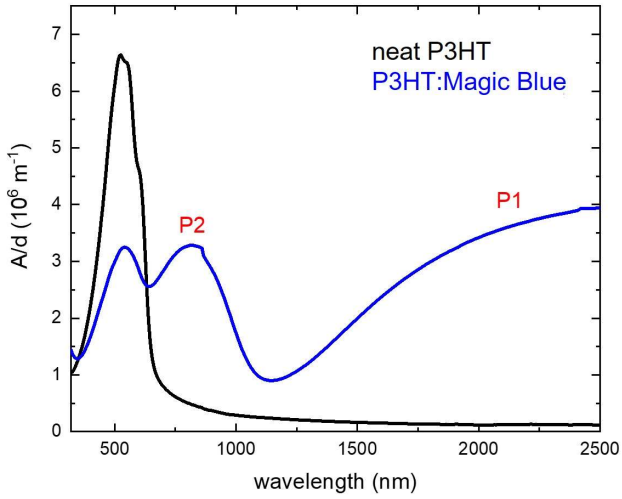

Figure 2.5. UV-vis-NIR absorption spectra showing the thickness normalized absorption (A/d) for neat P3HT and P3HT chemically doped with Magic Blue.

tend to couple and form bipolarons/polaron pairs. Several studies have focused on modeling and quantification of the optical absorption of polarons and bipolarons/polaron pairs.[70, 83-87] These include spectro-electrochemical measurements, spectral fitting and multivariate curve resolution as well as density functional theory (DFT) calculations.[87, 88] However, the identification of bipolaron/polaron pair formation in the system can be achieved by monitoring deviations of the absorption spectra from the isosbestic point between the neutral polymer and the P2 polaron absorption. An isosbestic point represents a point on a spectral curve where two or more species have the same molar extinction coefficient, suggesting no net change in concentration at that particular wavelength. In Figure 2.6a, which displays a series of UV-vis absorption spectra for the polymer p($g_4$2T-T) doped with varying concentration of H-TFSI, an isosbestic point is evident where several spectra intersect, indicating the coexistence of two primary species. These include neutral backbone segments that are increasingly replaced by oxidized segments with one positive charge (polarons). If the absorption curve of the doped polymer diverges from this intersection point, it indicates the presence of more than two absorbing species in the sample, and the formation of bipolarons/polaron pairs in the system is a likely explanation. In Figure 2.6b, the wavelength for where the doped spectra cross the neat spectra is plotted vs. the molar concentration of the dopant H-TFSI. Up to a molar concentration of 10 % H-TFSI, the crossover wavelength is 712 nm. This is the isosbestic point. For higher dopant concentration, the

crossover increases to higher wavelengths, indicating bipolaron/polaron pair formation. Nevertheless, the visualization of the isosbestic point between the neutral polymer and the polaron, as well as between the polaron and the bipolaron/polaron pair, is most effectively achieved with spectro-electrochemical measurements.[89]

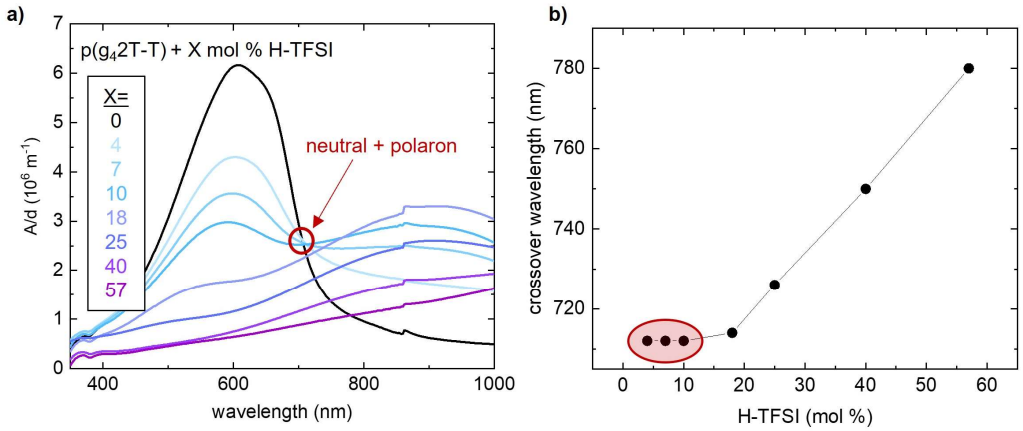

Figure 2.6. a) UV-vis absorption spectra of p(g42T-T) doped with varying concentration of H-TFSI displaying the emergence of an isosbestic point. b) Crossover wavelength between the absorption spectra of the neat and doped samples vs. mol % of the dopant H-TFSI.

Chapter 3

CHARGE TRANSPORT IN CONJUGATED POLYMERS

Charge transport in semiconductors is a critical aspect that significantly influences their applications in various fields. The electrical conductivity of a material is directly proportional to the product of the charge carrier concentration and mobility, as indicated by equation 1.1. Conjugated polymers, characterized by a low dielectric constant compared to inorganic semiconductors, exhibit strong Coulomb interactions between the charge carriers and the dopant counterions, resulting in a pronounced localization of charge carriers. Thus, it becomes essential to distinguish between bound and free charges, as only mobile charge carriers contribute to charge transport. This can be done through techniques such as metal-insulator-semiconductor (MIS) devices, THz spectroscopy and ultra-fast transient absorption spectroscopy.[65, 70-72, 87, 90]

The localized nature of the charge carriers in conjugated polymers leads to charge transport occurring through thermally activated hopping, a mechanism prevalent in disordered structures like organic semiconductors. Unlike band transport, where carrier mobility decreases with increasing temperature, hopping transport exhibits a contrary behavior, with carrier mobility increasing as the temperature rises.[7] This transport mechanism involves charge carriers moving between localized sites or energy levels, making conjugated polymers sensitive to the distribution of available states. Considering the density of states and disorder, the energetic disorder and resulting distribution of accessible states plays a pivotal role in determining the overall charge transport properties of conjugated polymers.

Doping introduces changes in the shape of the DOS due to the long range of the Coulomb potential of ionized dopants and the low dielectric constants inherent to most organic semiconductors. Experimental confirmation of the broadening of the DOS upon doping has been conducted through photoelectron spectroscopy.[91-93] The numbers of charge carriers that are dissociated (at a given point in time) are able to contribute to charge transport. At low dopant concentrations, a polaron can escape the Coulomb capture radius of the counterion with minimal chance of being captured by another counterion, resulting in a high dissociation efficiency approaching 100%. However, at intermediate dopant concentrations the dissociation efficiency decreases as polarons experience Coulomb

interactions with counterions. For P3HT doped with F_4TCNQ it has been shown that only 5% of carriers contribute to transport at a given point in time. At high dopant concentrations, the Coulomb capture radius of counterions start to overlap, preventing the polaron to move sufficiently far enough from the dopant counterion without feeling the influence of another counterion. However, overlap of the Coulomb capture radius concurrently induces charge screening. Consequently, the charge carriers can move through the material without encountering significant traps, as the Coulomb attraction is uniform. This interplay leads to charge transport primarily governed by collective interactions among all charges and counterions within the conducting material.

The degree to which a charge feels the presence of counterions in its vicinity partly depends on the dielectric constant of the host material. In line with Equation 2.3, an increase in the dielectric constant mitigates the Coulomb binding energy felt by the polaron in close proximity and this partial electrical screening results in a less strongly bound polaron. The dielectric constant of the conjugated polymer can be increased through side chain engineering. For example, the polar tetraethylene glycol side chains of p($g_4$2T-T) provide the polymer with $\varepsilon_r = 4.4$ as compared to $\varepsilon_r = 2.7$ for P3HT which has alkyl side chains.[94] Dopant anions such as F_4TCNQ (di)anions, reside between the side chains of the polymer and hence the higher dielectric constant of p($g_4$2T-T) can improve charge screening. As a consequence, the polarons on the polymer backbone experience a reduced impact from the surrounding counterions, potentially leading to a higher charge-carrier mobility and improved electrical conductivity.

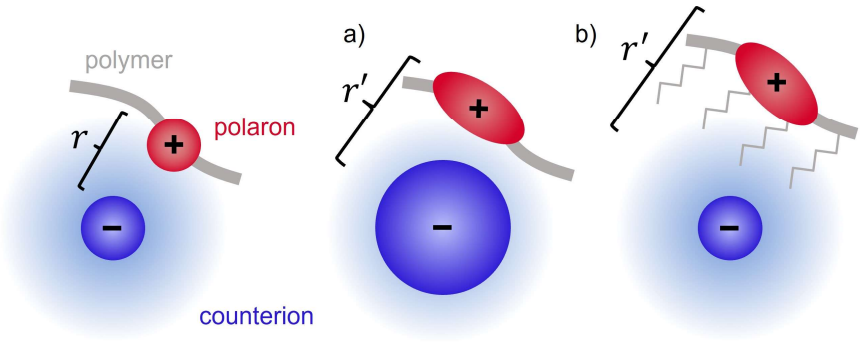

Figure 3.1. a) An increase in the size of the counterion or b) suitable polymer side chains will increase the effective distance between a counterion and an adjacent polaron from $\boldsymbol{r}$ to $\boldsymbol{r'}$, resulting in a less strongly bound polaron due to a lower Coulomb interaction. As a result, the polaron will delocalize to a greater extent along the conjugated polymer backbone. Reprinted with permission from Ref. 51, Copyright 2022, A.P.

The Coulomb binding between the dopant counterion and the polaron can also be reduced by increasing the distance between them. For example, as discussed in Section 2.5, using large dopant molecules increases the distance between the counterion and polaron. However, large dopants also occupy more space, restricting the volume for charge-conducting conjugated material and thus limiting the polaron density. The total DOS in polymers is approximately 10^{27} m^{-3}, implying that the material can, at best, accommodate one charge per cubic nanometer. Taking P3HT as an example, with a density of 1.1 g cm^-3, there are approximately 4 thiophene rings per nm^{-3}. Each thiophene serves as a potential redox site, and assuming a maximum oxidation level of 33%, common for PEDOT, the resulting maximum charge-carrier density is around 10^{27} m^{-3}.[95] However, considering that each charge is accompanied by a dopant, such as the relatively large molybdenum dithiolene complex Mo(tfd-$COCF_3$)$_3$ that has an effective size of about 11 to 14 Å,[96] the highest achievable charge-carrier density is on the order of $5x10^{26}$ m^{-3}. Another strategy to increase the distance between the dopant counterion and the polaron is to modify the polymer side chains (Fig. 3.1). However, extending the side chains could potentially limit the amount of charge conducting material as charge transport occurs on the polymer backbone.[97]

3.1 Influence of nanostructure on the nanostructure

Doping can strongly influence the nanostructure and texture of conjugated polymers, such as the degree of structural order, the size of ordered domains, and the connectivity between these domains. The introduction of a high concentration of dopant molecules can disrupt the nanostructure of the polymer, leading to a decrease in the degree of ordering, which negatively impacts the carrier mobility.[98-100] Conversely, at low dopant concentrations, doping has the potential to enhance the degree of π-stacking in less ordered polymers[100, 101], and alter the conjugation length of polymer chains in the amorphous regions.[99] The presence of structural disorder within the material is connected with electronic localization, leading to the formation of electronic traps. These traps, in turn, act as constraints, limiting the overall charge transport.

Achieving high carrier mobility requires the capability of charge carriers to be able to move on a macroscopic level. As most conjugated polymers consist of both ordered and disordered regions, both inter- and intramolecular transport is necessary. Long-range charge transport can be facilitated by long-range order of the polymer chains, contributing to low energetic disorder.[12] However, efficient long-range charge transport can also be achieved with short-range intermolecular aggregation or nanometer-sized ordered domains.

Two primary methods are employed to chemically dope conjugated polymers: co-processing, involving simultaneous processing of the polymer and dopant from the same solution, and sequential doping, where a polymer film is initially cast, and subsequently, a doping step occurs where the solidified film is brought into contact with a dopant solution or vapor (Fig. 3.2). Co-processing allows precise control over the specific ratio between the polymer and dopant.[65, 101] Nonetheless, the simultaneous dissolution of polymer and dopant presents challenges. Premature ionization of polymers in solution can decrease their solubility, resulting in the formation of aggregates characterized by fewer tie chains.[7] This reduced connectivity between crystalline domains leads to a lower charge-carrier mobility. Therefore, the selection of processing solvents significantly impacts the solid-state nanostructure of films. Sequential processing involves dopant diffusion into the already solidified polymer. Thin polymer films experience rapid doping,[96] while thicker structures require prolonged exposure to a dopant solution or vapor.[99] In the two-step process, the nanostructure of the polymer is largely preserved during the doping step, allowing for the selection of an optimal nanostructure before doping. However, a disadvantage of sequential doping is the challenge of precisely determining

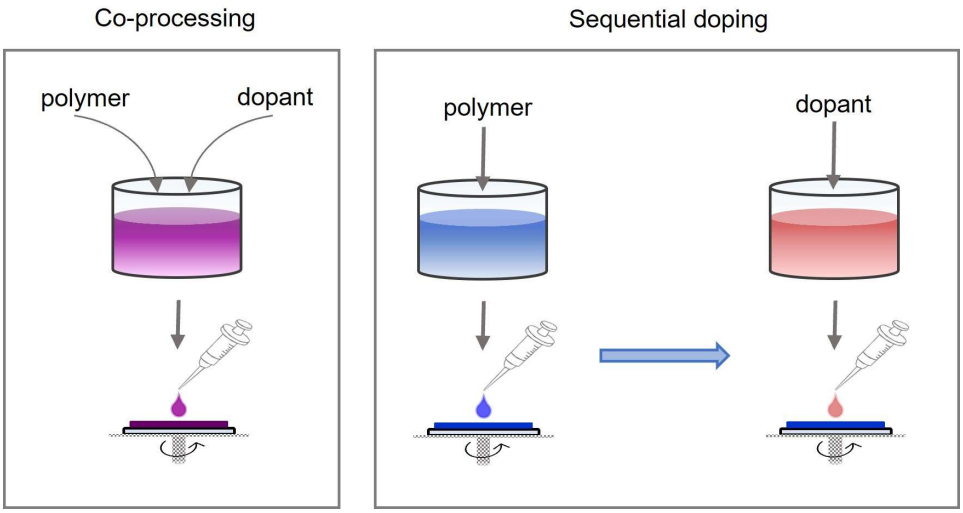

Figure 3.2 Illustration of co-processing (right) which involves the deposition of the organic semiconductor and molecular dopant from the same solution. The right part of the figure illustrates sequential doping process (left), which is a two-step method where the conjugated polymer is initially cast from a solution, followed by doping through contact with a molecular dopant dissolved in an orthogonal solvent or dopant vapor. Both illustrations show deposition through spin coating.

the amount of dopant molecules that have entered the material. In addition to the methods described above, ion-exchange doping represents an additional approach to achieve doping.[102, 103] In this procedure, charge transfer occurs between the dopant and the polymer, and the resultant dopant counterion is substituted with another counterion. This replacement counterion is unable to undergo charge transfer with the polymer and serves solely to counterbalance the opposite charge of the charge carrier in the polymer. This method increases the temperature stability of the doped system.[104]

3.2 Interplay between conductivity and carrier density

Doping increases the charge carrier concentration, with the goal of simultaneously improving conductivity and charge carrier mobility. The charge carriers in conjugated polymers exhibit strong Coulomb interactions with the dopant counterions, resulting in a pronounced charge carrier localization in the low-doping regime (<1 mol%), and the enhancement of electrical conductivity and carrier mobility primarily occurs through the filling of deep-lying trap states.[105] However, at high concentrations, the electronic landscape is flattened due to the overlapping Coulomb potentials of the counterions, reducing the dependence of conductivity on carrier-dopant interactions and thereby improving charge transport.[106, 107]

The conductivity of organic semiconductors is directly proportional to the product of carrier density and mobility. In the high doping regime (N >10^{26}), a power-law trend between conductivity and charge carrier density across various doped organic semiconductors, is observed as:

$$\sigma \propto N^{\gamma} \tag{3.1}$$

where γ typically falls within the range of 2-5. This behavior can be explained by a variable range hopping model with an energy dependent delocalization length.[108] The aggregate plot in Figure 3.3 compiles experimental data from literature and this thesis, depicting conductivity versus charge density. The consistent adherence to the power-law trend across all presented data emphasizes the robustness and applicability of this relation in understanding the conductivity behavior in highly doped organic semiconductors. Notably, the exception found in p($g_4$2T-T) doped with H-TFSI adds nuance to this observation.

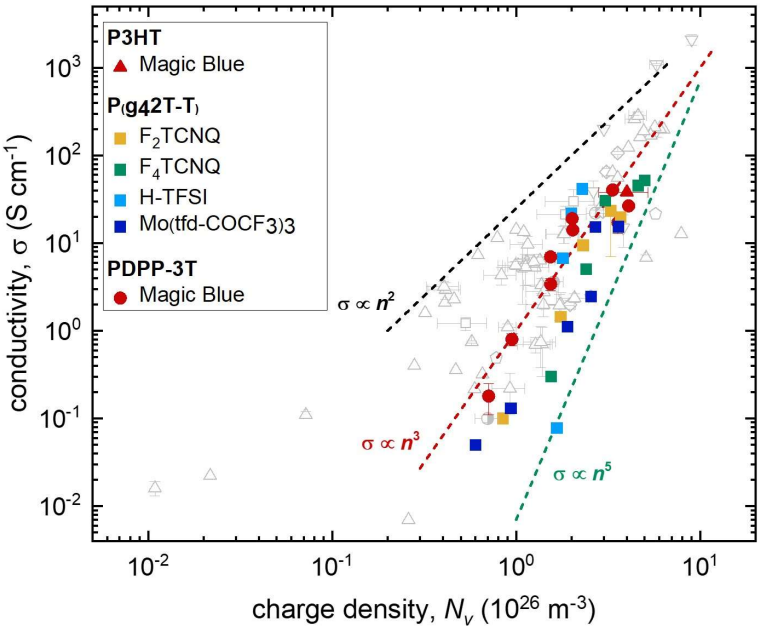

Figure 3.3. Conductivity σ as a function of charge density molecularly doped conjugated polymers. The closed colored symbols represent data from this thesis work. Faded gray symbols were collected from literature (for references see paper VI of this thesis). The dashed lines are power laws of varying slopes that were added to guide the eye. Reprinted with permission from Paper VI.[108]

Chapter 4

DETERMINATION OF POLARON DENSITY

To optimize the performance of electronic devices, fine control over the charge carrier density becomes essential. Hence it is crucial to be able to accurately quantify the number of polarons (bound and free). This chapter explores a variety of techniques that can be used to assess the polaron density in chemically doped conjugated polymers.

4.1 Spectro-electrochemistry and chronoamperometry

Electrochemistry serves as a valuable tool for analyzing reactions involving electron transfer processes, notably redox reactions. Despite its utility, traditional electrochemical methods often lack the capability of identifying the specific electroactive species present and offer limited insights into structural changes resulting from redox events. In response to these limitations, spectro-electrochemistry has emerged as a powerful approach, combining spectroscopic and electrochemical methods to simultaneously explore electronic and structural changes occurring in chemical species during electrochemical processes. Spectroscopy enables the acquisition of molecular information including vibrational frequencies, molar absorptivities, luminescence intensities, and electronic or magnetic resonance frequencies. The combination of electrochemical and spectroscopic techniques can contribute to the elucidation of electron transfer reaction mechanisms and to the understanding of fundamental molecular states at interfaces.

In the context of conjugated polymers, spectro-electrochemical techniques stand out as valuable tools for studying the doping process. For example, Banerji and coworkers performed electrochemical doping of P3HT in tandem with Vis/NIR-, Raman-, and THz spectroscopy to investigate the correlation between the generation dynamics of charged species (polarons/bipolarons) and nanoscale conductivity at different doping levels.[87] Moreover, spectro-electrochemistry proves instrumental in determining the molar absorptivity of the P2 polaronic transition, ε_{p2}, by employing UV-vis spectroscopy in combination with chronoamperometry. If ε_{p2}, representing the strength of absorption of the polaronic state, is known, the charge carrier density of the doped polymer can be estimated

from the optical spectra (Section 2.7). It is important to note that alterations in the texture and orientation of polymer chains impact the extinction coefficient. For instance, polymer chains may exhibit a preferential alignment with the substrate, either parallel or perpendicular to it, resulting in anisotropic optical constants characterized by greater in-plane values compared to out-of-plane values.[109, 110]

Chronoamperometry, a technique within electrochemistry, involves stepping the potential of the working electrode and monitoring the resulting current over time. Prior to conducting chronoamperometric measurements, cyclic voltammetry is performed to establish the oxidation or reduction potential of the polymer. In the case of p-doping, chronoamperometry measurements are conducted by applying static positive potentials above the oxidation potential, leading to oxidation of the polymers, and generating a transient current *I(t)*. Integration of the transient current over time facilitates the determination of the number of charges (Q) injected to the sample (eq. 4.1).

$$Q = \int_{t=0}^{\infty} I(t)dt \qquad (4.1)$$

Upon normalizing Q with the sample volume, the carrier density Q_v is obtained. Following the completion of the oxidation reaction at each potential, an absorbance spectrum is recorded and normalized by the sample thickness. The difference in absorbance between the doped and undoped polymer at the wavelength where the polaron absorbs is then plotted against the charge density. Assuming no other absorbing species exist in the system at this wavelength, this results in a linear trend, and the slope of this linear trend represents the molar extinction coefficient. Within the scope

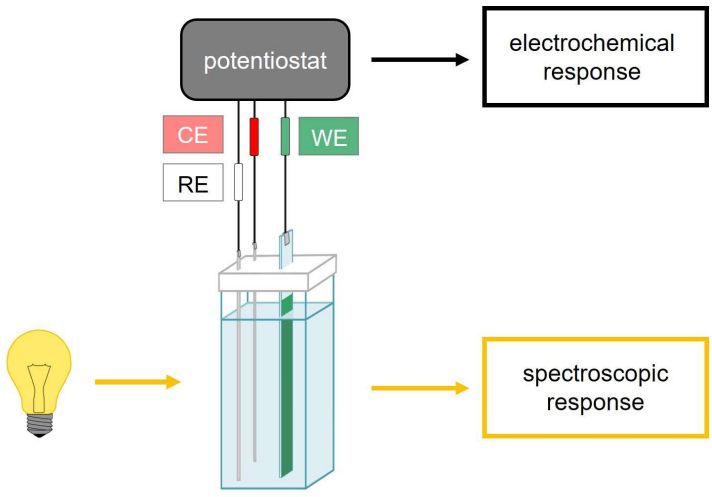

Figure 4.1. Typical three electrode experimental setup in a spectro-electrochemical measurement combining chronoamperometry and optical absorption spectroscopy.

of this thesis, this spectro-electrochemistry in combination with chronoamperometry was used to estimate ε_{p2} for the conjugated polymer PDPP-3T, and a more comprehensive discussion will be presented Chapter 5.

The experimental configuration typically consists of a three-electrode setup comprising a working electrode (WE), counter electrode (CE) and a reference electrode (RE), as depicted in Figure 4.1. The working electrode is typically composed of a conductive transparent material, like indium tin oxide (ITO)-coated glass, with a thin polymer film deposited on top. These electrodes are connected to a potentiostat, responsible for regulating electrochemical potential to either oxidize or reduce the polymer film, while also recording the electrical response. Simultaneously, the polymer film undergoes exposure to electromagnetic radiation, and the spectroscopic response is recorded.

4.2 UV-Vis-NIR spectroscopy

UV-vis spectroscopy studies light absorption or transmission as a function of wavelength, providing information about electrical transitions in the material. This method involves measuring the intensity of light in the UV range (200-400 nm) and the visible range (400-800 nm). Some instruments have a broader range including the near-infrared (NIR) spectra, ranging from 800 to 2500 nm. The fundamental principle underlying UV-vis spectroscopy is the absorption of light, where the amount of absorbed light is directly proportional to the quantity of analyte present in a sample. The amount of light that is absorbed is described by the Beer-Lambert law, which is expressed as follows:

$$A = \varepsilon \cdot c \cdot l \tag{4.2}$$

Here, *A* denotes absorbance, *ε* represents the molar extinction coefficient of the material, *c* is the concentration of the absorbing species, and *l* signifies the path length of light through the sample. The measurement of light absorption across wavelengths provides valuable insights into the electronic transitions within a material. In the context of conjugated polymers, UV-vis spectroscopy serves as a powerful tool in assessing the charge density in chemically doped conjugated polymers. The charge-carrier density (N_v) can be estimated by analyzing the optical spectra of the polymer (Fig. 4.2). The method involves using the difference in absorption between the pristine and doped polymer (A_{P2}) at the wavelength corresponding to the emergence of the P2 polaron peak upon doping. The estimation of carrier density is achieved through the application of the Beer-Lambert law, expressed as follows:

$$A_{P2} = \varepsilon_{P2}\, N_v\, d \tag{4.3}$$

Here, ε_{P2} is the molar extinction coefficient of the P2 polaronic transition (see Section 4.1) and *d* is the sample thickness.

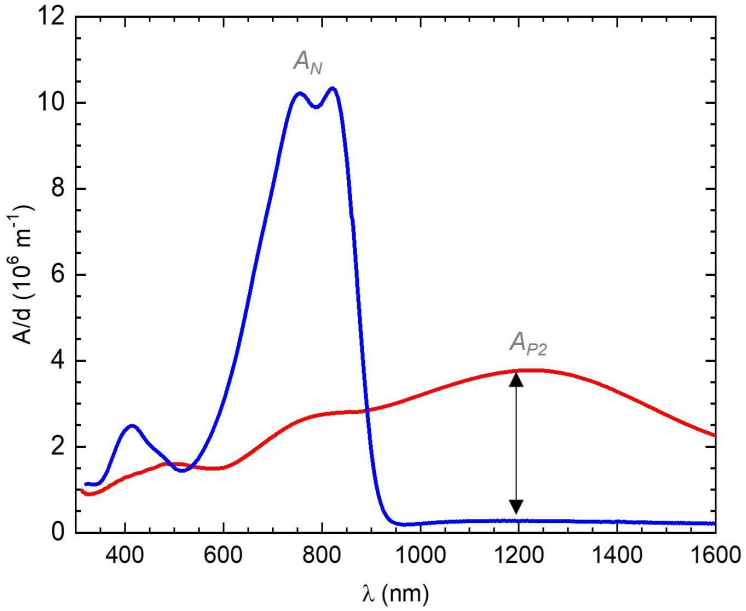

Figure 4.2. UV–vis spectrum of a 149 nm thin PDPP-3T film showing only absorbance by the neat polymer A_N (blue), and a 126 nm thin PDPP-3T film sequentially doped with Magic Blue, dominated by the polaronic absorbance A_{P2} (red). Reprinted with permission from Ref. 64. CC BY 4.0

Moulé and colleagues have proposed an alternative approach for quantifying the carrier density in chemically doped polymers, employing UV-vis spectroscopy.[83] Their study focuses on sequentially doped samples, where they calculate the polaron mole fraction (Θ) by comparing the peak area of the neutral polymer absorption and the polaron absorption. This fraction represents the proportion of polymer sites occupied by polarons in a sequentially doped polymer film. Employing a Langmuir isotherm model, they fit the dependence of the dopant solution concentration on Θ, enabling the characterization of sequential doping through an equilibrium constant.[111] The carrier density, *P(Θ)* in the sample is then estimated by using the following equation:

$$P(\Theta) = S_N \cdot \Theta \cdot \frac{V_S}{V_{Ave}(\Theta)} \tag{4.4}$$

Where S_N is the site density of the undoped polymer, V_S is the polymer site volume and V_{Ave} is the average site volume considering the volume of the dopants.

In both presented methods for assessing the polaron density, it is crucial to ensure that the dopant employed does not exhibit any absorption peak in the same range of wavelengths as the polaron P2 peak. Notably, dopants like Magic Blue and H-TFSI as well as the cyclopropane based dopants used in study from the Moulé group[83] are deemed suitable, as they do not absorb in the same spectral region as the polymer polaron P2 peak. However, estimating charge density using these methods is unsuitable for the widely used dopant F_4TCNQ, as its anion absorbs in the same range of wavelengths as the P2 peak in most conjugated polymers.

4.3 Infrared spectroscopy

Fourier Transform Infrared Spectroscopy (FTIR) spectroscopy, a powerful analytical tool, relies on the absorption of infrared radiation due to molecular vibrations. With this technique, two primary vibration types are observed: stretching vibrations (ν), indicative of alterations in bond length along chemical bonds, and bending vibrations (δ-in plane, π-out-of-plane), which involve changes in bond angles. What sets FTIR apart from other optical spectroscopy techniques, is its approach to measuring absorption of radiation. The common practice in for example UV-vis spectroscopy, is to use a monochromatic light beam to measure the absorption for each wavelength individually. FTIR, on the other hand, utilizes a beam that incorporates multiple wavelengths simultaneously and measures how much of the beam is absorbed. The sample is scanned numerous times within a short time span and each iteration modifies the beam to include a different combination of wavelengths. Subsequently, a computer processes the output data from these scans, employing the mathematical technique Fourier transform to convert it into the infrared absorption spectrum. The resulting absorption spectrum is expressed in wavelength^{-1}, typically in units of cm^{-1}.

In the investigation of chemically doped conjugated polymers, FTIR is a valuable tool for determining the polaron density. In the scope of this thesis, FTIR was found to be particularly useful when estimating the polaron density of conjugated polymers doped with quinodimethane type dopants, such as F_4TCNQ. A challenge arises when attempting to estimate polaron density of F_4TCNQ doped films using the P2 polaron peak analyzed by UV-vis spectroscopy. This difficulty stems from the fact that neutral and anionic species of F_4TCNQ absorb within the same spectral region where the P2 polaron peak conventionally arises upon doping (Fig. 4.3). FTIR spectroscopy, however, offers a distinct advantage in this scenario. The stretching frequencies of the cyano groups (CN) in F_4TCNQ give rise to distinct absorption peaks in the infrared (IR) region, detectable through FTIR spectroscopy (Fig. 4.4a). Furthermore, the CN-stretch vibrations of F_4TCNQ generate characteristic absorption features depending on the molecular state — neutral, anionic or dianionic. This distinction allows for the

estimation of not only polaron density but also facilitates the determination of the number of anions relative to the number of dianions. The molar absorption of the CN-stretch of neutral F_4TCNQ is too weak to be used for characterization. Upon doping a conjugated polymer with F_4TCNQ, these absorption features become detectable on top of the P1 polaron peak (Fig. 4.4b) enabling the estimation of the polaron density. A more detailed discussion of using FTIR for estimating the polaron density in conjugated polymers doped with quinodimethane type dopants will be described in Chapter 7.

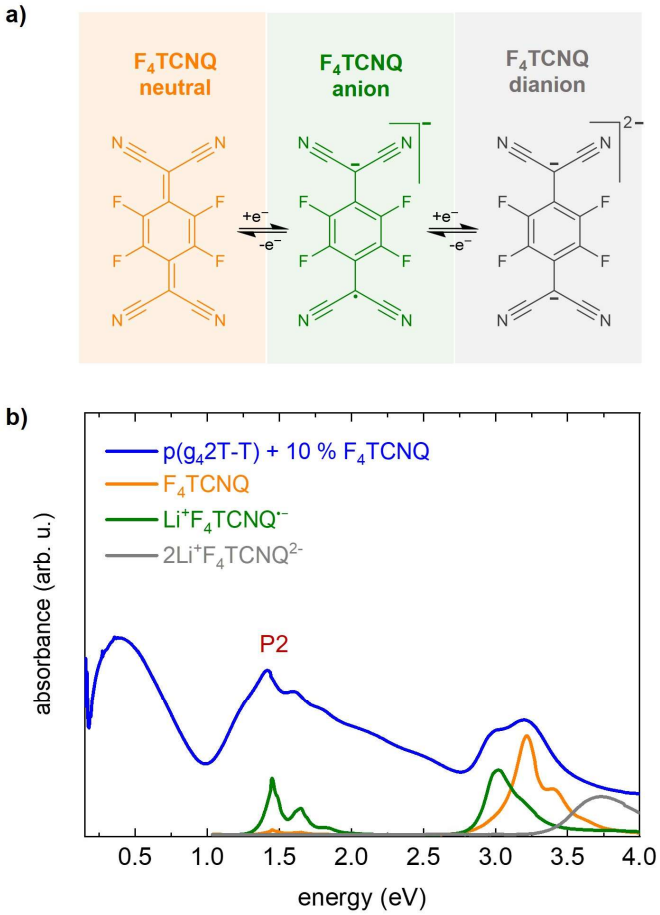

Figure 4.3. a) Chemical structures of neutral F_4TCNQ, $F_4TCNQ^{\bullet-}$ and F_4TCNQ^{2-}. b) UV-vis absorption spectra of neutral F_4TCNQ, $Li^+F_4TCNQ^{\bullet-}$and $2Li^+F_4TCNQ^{2-}$ recorded in solution. UV-vis-IR absorption spectra of p($g_4$2T-T) doped with 10 mol % F_4TCNQ per thiophene unit. The UV-vis absorption spectra of neutral F_4TCNQ, $Li^+F_4TCNQ^{\bullet-}$and $2Li^+F_4TCNQ^{2-}$ were taken from Ref. 65.

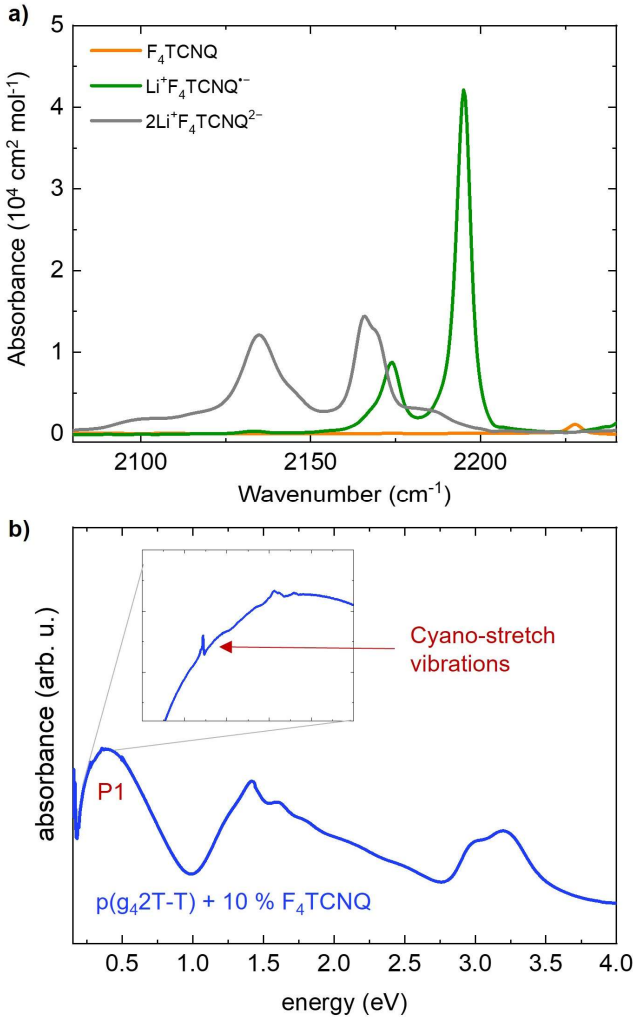

Figure 4.4. a) FTIR absorption spectra of neutral F_4TCNQ, $Li^+F_4TCNQ^{\bullet-}$ and $2Li^+F_4TCNQ^{2-}$ dissolved in acetonitrile. b) UV-vis-IR absorption spectra of p($g_4$2T-T) co-processed with 10 mol % F_4TCNQ per thiophene. The inset shows the position of the cyano-stretch vibrations atop the P1 polaron peak. The FTIR absorption spectra of neutral F_4TCNQ, $Li^+F_4TCNQ^{\bullet-}$ and $2Li^+F_4TCNQ^{2-}$ was taken from Ref. 65.

4.4 Electron paramagnetic resonance spectroscopy

Electron paramagnetic resonance (EPR) spectroscopy,[112-117] also known as electron spin resonance (ESR) spectroscopy, is a technique which like nuclear magnetic resonance (NMR) spectroscopy is used to study the interaction of spins with external magnetic fields. The focus of EPR spectroscopy lies in the interaction of electron spins with an external magnetic field. Like other spectroscopic techniques,

EPR spectroscopy relies on the absorption of electromagnetic radiation, inducing a transition between a lower energy state and a higher energy state. In accordance with Planck's equation (eq. 4.5), electromagnetic radiation is absorbed when:

$$\Delta E = h\nu \tag{4.5}$$

where *ΔE* represents the difference between the low energy and the high energy states, *h* is Planck's constant and ν is the frequency of radiation. The energy differences probed with EPR spectroscopy result from the interaction of unpaired electron spins with an applied magnetic field, B_0. Therefore, the species of interest must contain unpaired electron spins, i.e. the material must be paramagnetic, such as a dopant monoanion or a polymer containing polarons.

EPR exploits the Zeeman effect, which entails the alignment of an unpaired electron spin with B_0. In a classical picture, an electron, being a charged particle, generates a magnetic field due to the angular momentum resulting from its spinning around its axis. In essence, the electron, possessing both angular momentum and charge, behaves like a small bar magnet or magnetic dipole with a magnetic moment, μ. When exposed to an external magnetic field, the unpaired electron spin aligns with the external field, producing two energy states for its magnetic moment. There is a lower energy state when the electron spin aligns parallel with B_0 and a higher energy state when the spin aligns in the opposite direction (anti-parallel). The energy difference, *ΔE*, signifies the amount of energy required to induce a transition between the two spin states. Without the applied magnetic field, both spin states have the same energy, and hence *ΔE*=0. With increasing magnetic field strength, the energy difference between the two states increases (see illustration in Figure 4.5), according to

$$\Delta E = g_e \beta B_0 \tag{4.6}$$

where β is the Bohr magneton, and g_e is the electron g-factor. The electron g-factor contains chemical information about the electronic structure of the molecule and is often used as a "molecular fingerprint", similar to the chemical shift in NMR spectroscopy. Combining Equation 4.6 with Planck's equation (eq. 4.5.), the equation can be expressed as:

$$\Delta E = g_e \beta B_0 = h\nu \tag{4.7}$$

In a measurement of the EPR, the sample is irradiated with microwaves at a constant frequency, typically in the range of 9-10 GHz, while scanning the magnetic field. An absorption peak occurs when the condition in Equation 4.7 is satisfied, i.e., when the magnetic field tunes to the two electronic spin states, matching their energy difference with the energy of the radiation (Fig. 4.5). This magnetic field is termed the "field of resonance". The measured energy difference between the two electronic spin

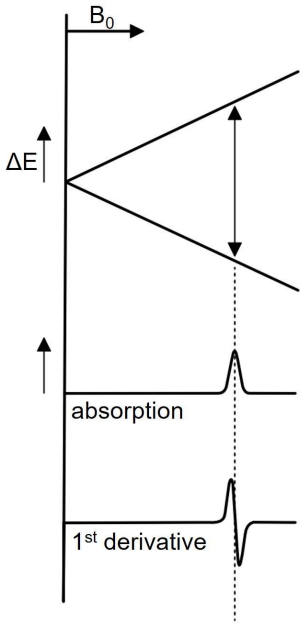

Figure 4.4. Illustration of the relationship between magnetic field strength and the energy difference ΔE between the two spin states and the corresponding absorption signal. The figure is adapted from Ref. 118.

states depends linearly on the magnetic field (eq. 4.7 and Fig. 4.5). Upon absorption, all parameters in Equation 4.7 are known except g_e, which can then be calculated. Electron spins with different electronic surroundings exhibit different electron g-factors, resulting in absorption at different magnetic fields. Hence, determination of the g-factor enables the identification of different species.

In the experimental configuration, the sample is positioned in a resonant cavity that allows microwaves to enter through an iris. The cavity, situated in the middle of an electromagnet, serves to amplify the weak signals from the sample. The majority of EPR spectrometers operate at a microwave frequency of around 9.5 GHz. The radiation can either be continuous (continuous wave, CW) or pulsed. Here, the focus is on EPR spectrometers utilizing CW radiation.

Most spectroscopic techniques yield an absorption spectrum similar to the one depicted in Figure 4.5. In EPR spectrometers employing CW radiation, field modulation combined with a phase-sensitive detector is employed to get a sufficiently high signal-to-noise ratio. This results in the detection of the slope of the absorption peak, and hence the absorption of microwave radiation is presented in its first derivative form (Fig. 4.5). As the EPR signal is recorded in its first derivative form, the point at which the first derivative of spectrum intersects zero corresponds to the maximum of the absorption peak. This point is used to determine the center of the signal. Additionally, an advantage of recording the

absorption in its first derivative form is that it amplifies minor asymmetries, facilitating a more detailed analysis of the results.

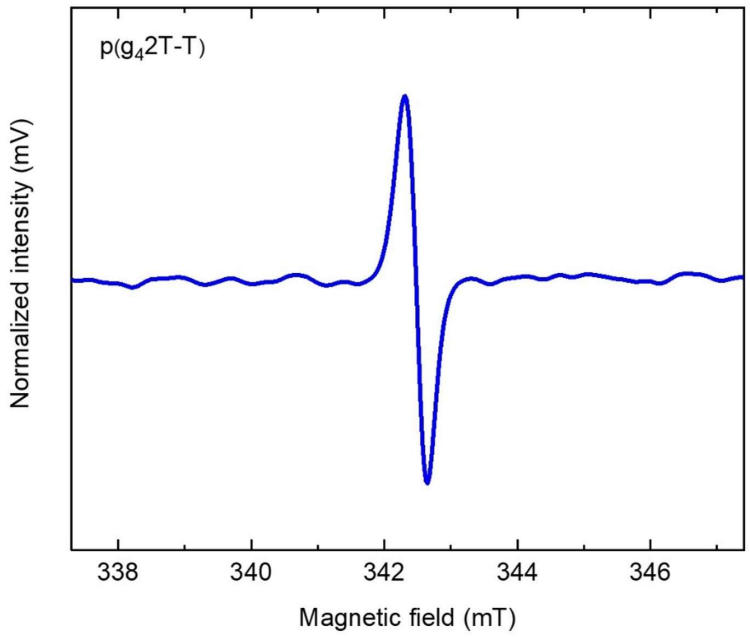

Figure 4.5. EPR spectra of p($g_4$2T-T) doped by atmospheric oxygen. The EPR measurement and data processing were conducted by Dr. Till Biskup, Saarland University.

In the context of molecular doping of conjugated polymers, EPR is a powerful tool for detecting the presence of species containing unpaired electron spins within a sample and offering a quantitative evaluation of their abundance. These encompass radical cations, radical anions, and various paramagnetic entities arising during the doping process.[119, 120] For example, polarons, which serve as potential charge carriers in conjugated polymers, are unpaired electron spins coupled with an associated lattice deformation and hence, EPR is a valuable instrument for both detecting and quantifying polarons.[64, 120] Figure 4.6 shows an EPR spectrum of the conjugated polymer p($g_4$2T-T), which has been oxidized by atmospheric oxygen. The spectrum shows a clear absorption feature centered at a magnetic field of 342.2 mT, for a microwave frequency of 9.6 GHz, arising from the polarons introduced through oxidation. If the magnetic field at which the polaron absorbs is known, it is possible to calculate the electron g-factor. However, sometimes knowing the magnetic field at which absorption occurs is sufficient to distinguish between different species. The signal area of the absorption obtained by double integration of the EPR spectrum is proportional to the number of detected spins. While this allows for an absolute quantification of the number of spins, the process can

be challenging due to the difficulty of evaluating the parameters that influence spectrometer signal.[121] Instead, a common approach involves comparing the spectrum of the sample with an unknown number of spins with the spectrum of a sample with a known number of spins.[64, 120, 121] Beyond polaron analysis, EPR can be used to detect the dopant anion formed upon doping with the polymer — a paramagnetic species with an unpaired spin.

4.5 Other techniques for studying the polaron density

There are other methods that can be used to reveal information about the carrier density in conjugated polymers. For example, Hall effect measurements can be used to assess the polaron density.[7, 77] The technique utilizes the Lorentz Force, which is the force felt by a charge when moving through a magnetic field. For a p-doped sample, the magnetic field pushes positive charges (holes) to one side of the sample. The resulting Hall voltage and current can then be used to extract the carrier density. However, it is only the charges that are mobile that will be quantified, i.e. the charges that are able to dissociate.

Another technique which is used to gain information about the charge carriers is Raman spectroscopy. Raman spectroscopy, utilizing light scattering to examine molecular vibrations, becomes a robust tool when paired with electrochemical techniques. This combination is particularly effective in studying molecular changes in polymers under different electrochemical conditions. It allows for distinguishing between neutral and charged species in materials, providing insights into interactions with charge carriers. While Raman spectroscopy yields valuable qualitative information about the charge carrier population, extracting quantitative details like charge density may require additional methods.[84, 122] Ultra-fast transient absorption spectroscopy and THz spectroscopy are valuable tools to analyze the carrier population in doped samples.[70-72] Although they are not used for quantitative analysis of the polaron density, they can provide valuable information about the relative amount of free and bound polarons.

4.6 Aims of the thesis

The aim of this thesis is to advance the understanding of doped polymers through a comparison of various methods that can be employed to assess the polaron density. These methods fall into two major categories, electric techniques, and spectroscopic techniques, both capable of estimating polaron density. This thesis places a primary focus on the application of spectroscopic techniques. This choice is grounded in the straightforward nature of spectroscopy. Through detecting changes in the

electronic structure of materials, these techniques enable the identification and quantification of electronic states.

Utilizing different spectroscopic methods to estimate polaron density, the thesis aims to address the following questions:

- Can optical methods effectively estimate polaron density?
- To what extent does chemical doping affect the mechanical properties of conjugated polymers?
- Is the concept of multiple electron transfer between the dopant and the conjugated polymer a universally applicable concept?

Chapter 5

COMPARISON OF AND EPR SPECTROSCOPY AND SPECTRO-ELECTROCHEMISTRY

In Section 4.1 of this thesis, I describe how the combination of spectro-electrochemistry and chronoamperometry can be used as a tool for estimating ε_{p2} in conjugated polymers. In paper I, this methodology is used for an in-depth investigation of the oxidation of conjugated polymer PDPP-3T (chemical structure in Fig 1.1), and the corresponding experimental results are presented in Figure 5.2.

The experimental configuration for the spectro-electrochemical measurements was consistent with the setup in Figure 4.1. A thin film of PDPP-3T was cast on top of an ITO/glass slide, which served as the working electrode. Initially, cyclic voltammetry was employed to identify the onset of polymer oxidation (Fig. 5.1a). Subsequently, chronoamperometry measurements were conducted by applying static positive potentials above the oxidation threshold, inducing partial polymer oxidation and generating a transient current *I(t)* (Fig. 5.1b). The integration of this transient current over time, as expressed in Equation 4.1, facilitated the determination of the total number of charges, Q, introduced in the sample. Upon normalizing Q by the sample volume, the resulting charge carrier density Q_v was obtained. Following the completion of the oxidation reaction at each potential, an absorbance spectrum was recorded which was normalized by the sample thickness (Fig. 5.1c). Analysis of the absorbance spectrum revealed the P2 polaron peak for PDPP-3T at around 1200 nm. The difference in absorbance between the doped and pristine PDPP-3T at this wavelength was plotted against the calculated Q_v (Fig. 5.1d). The resulting linear trend suggests that there is only one absorbing species at this wavelength, attributed to polarons, with the slope representing ε_{p2}. The ε_{P2} for PDPP-3T was then used to estimate the polaron density for PDPP-3T chemically doped with the dopant Magic Blue, which yielded a polaron density of $N_v^{UV-vis} = (3.4 \pm 0.3)\cdot 10^{26}$ m^{-3} (Fig. 5.2a). As a comparison, EPR spectroscopy was also used to assess the number of charges which resulted in a value of N_v^{EPR} = (1.4 ± 0.3)·10^{26} m^{-3} (Fig. 5.2b). Both methods yield comparable values on the order of 10^{26} m^{-3}, which are typical for highly doped conjugated polymers.

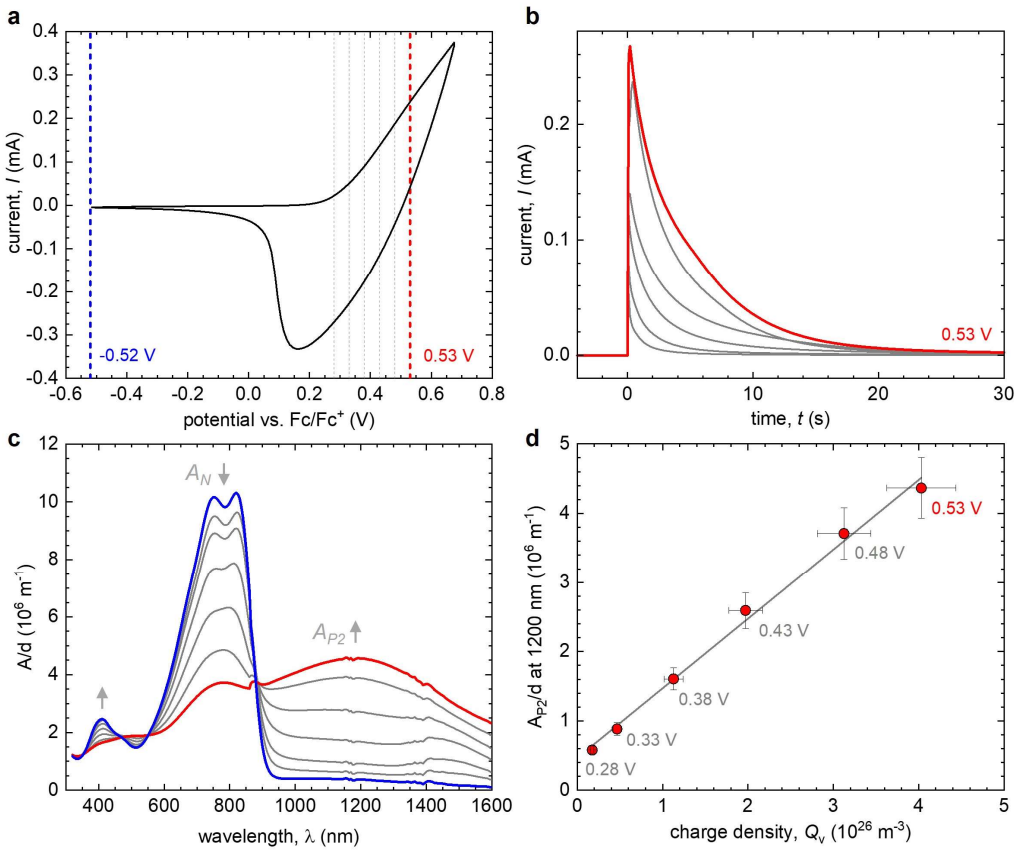

Figure 5.1. Cyclic voltammogram of PDPP-3T; b) electrochemical transient currents and c) UV-vis absorption spectra recorded at different constant electrochemical potentials; and d) the thickness-normalized absorbance A_{P2}/d at 1200 nm versus the charge density Q_v calculated by integration of the electrochemical transient currents and normalized with regard to the sample volume. Reprinted with permission from Ref. 64. CC BY 4.0. All spectro-electrochemical measurements and data processing was performed by Dr. Anna I. Hofmann.

Extending this exploration, I conducted a similar comparison for P3HT doped with Magic Blue, leading to analogous findings (Fig. 5.3). A thin film of P3HT was fabricated through spin-coating and sequentially doped by immersing the film in a Magic Blue solution (experimental details in Appendix I). The carrier density was determined from the optical spectra by utilizing ε_{p2} for P3HT at 800nm, determined by Untilova et. al. through the same spectro-electrochemical method as described above.[96] This analysis resulted in a polaron density of N_v^{UV-vi} = (4.1 ± 0.3)·10^{26} m^{-3} (Fig. 5.3a). A concurrent evaluation using EPR spectroscopy for the same sample yields a value of N_v^{EPR} = (1.9 ± 0.3)·10^{26} m^{-3} (Fig. 5.3b). Consistent with the results obtained for doped PDPP-3T, both methods yield

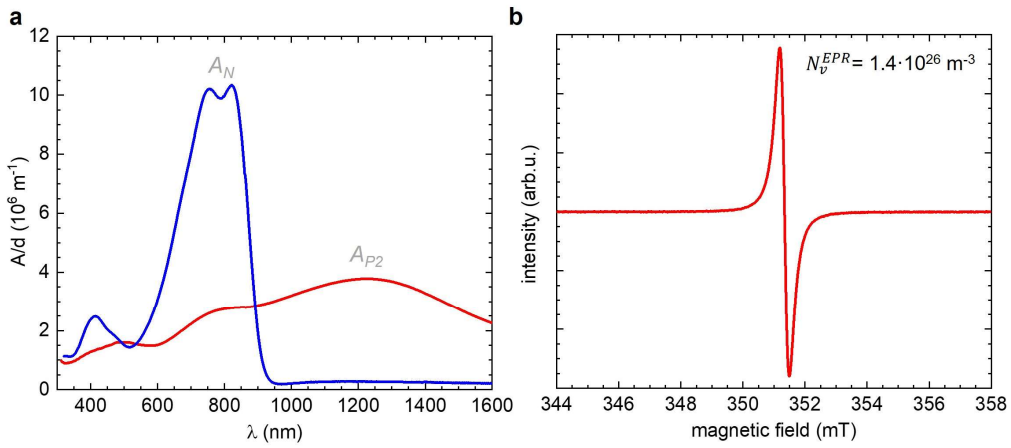

Figure 5.2. a) UV–vis spectrum showing the thickness normalized absorbance A/d of a 149 nm thin PDPP-3T film displaying only absorbance by the neat polymer A_{Nn} (blue), and a 126 nm thin PDPP-3T film sequentially doped with Magic Blue, dominated by the polaronic absorbance A_{P2} (red) and b) EPR spectrum of the same doped PDPP-3T film. Reprinted with permission from Ref. 64. CC BY 4.0. The EPR measurement and data processing were conducted by Dr. Till Biskup, Saarland University.

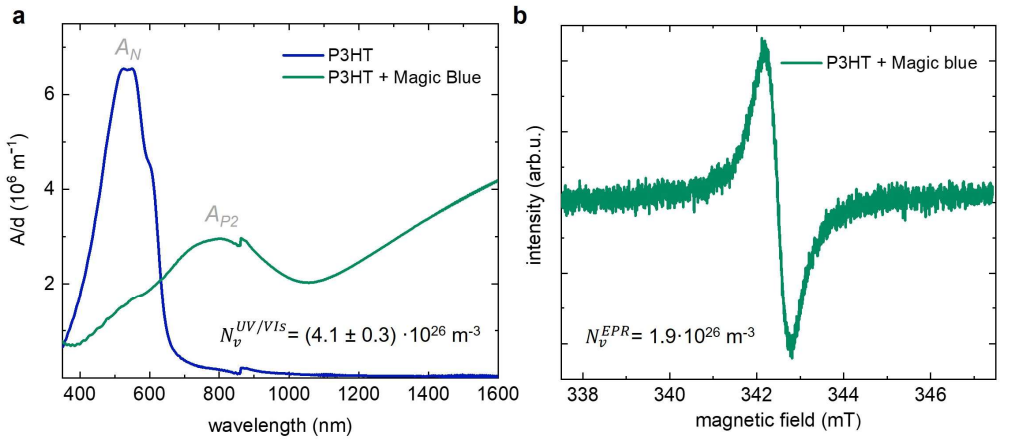

Figure 5.3. Unpublished data. a) UV–vis spectrum of a 47 nm thin P3HT film showing only absorbance by the neat polymer A_N (blue), and the same P3HT film sequentially doped with Magic Blue, dominated by the polaronic absorbance A_{P2} (green) and b) EPR spectrum of the same doped P3HT film. The EPR measurement and data processing were conducted by Dr. Till Biskup, Saarland University.

comparable values of the polaron density for doped P3HT. However, for both PDPP-3T and P3HT doped with Magic Blue, EPR analysis consistently indicates lower polaron densities compared to those obtained using ε_{p2}. The lower carrier densities measured by EPR spectroscopy might be attributed to the dependence of the method on measurements relative to a sample with a known carrier concentration.

Chapter 6

EXTINCTION COEFFICIENT IN THE VISIBLE REGION

This chapter focuses on the determination of carrier density using the optical absorption of the P2 polaron peak and its molar extinction coefficient. Specifically, I examine the absorption characteristics of p($g_4$2T-T), considering data from Paper IV and Paper VI.

Neat p($g_4$2T-T) demonstrates an absorption peak at approximately 600 nm, with additional shallow absorption features at higher wavelengths attributed to slight doping by atmospheric oxygen (Fig. 6.1a and 6.1b). As the degree of oxidation increases upon doping, the peak at 600 nm diminishes, while two polaronic absorption bands emerge around 900 nm and in the near infrared region. As introduced in Chapter 4, the carrier density in conjugated polymers can be estimated by comparing the difference in absorption between the neat and the doped polymer using the $\varepsilon_{P2.}$ For estimation of the polaron density in p($g_4$2T-T), I used $\varepsilon_{P2} = (4.1 \pm 0.2) \cdot 10^3$ m^2 mol^{-1}, a value determined for electrochemically oxidized P3HT by Untilova et. al., given that both polymers share the same backbone.[96] Notably, carrier density determination using the P2 polaron peak is valid only if there are exclusively polarons absorbing in the system. Therefore, ensuring the absence of other absorbing species is crucial. To verify this, the crossover between the spectra of the neutral polymer and the oxidized polymer is monitored. The presence of an isosbestic point suggests the presence of only two absorbing species, the neutral polymer and polarons, and thus the presence of bipolarons/polaron pairs can be ruled out.[89, 123]

Figure 6.1 displays the absorption spectra of p($g_4$2T-T) doped with varying concentrations of H-TFSI or Mo(tfd-$COCF_3$)$_3$ (Fig. 6.1a and 6.1b, respectively). For both dopants, the P2 polaron absorption initially increases until reaching a certain dopant concentration, after which it begins to decrease. Simultaneously, the absorption in the NIR continues to rise. An isosbestic point at 700 nm is observed for up to 10 mol% H-TFSI, indicating the presence of two major species: neat backbone segments that are increasingly replaced by oxidized segments with one positive charge (polarons). A second isosbestic point emerges at 1170 nm for higher concentrations of H-TFSI, suggesting the presence of both polarons and bipolarons/polaron pairs upon further oxidation.[85] Similar behavior is observed for doping with Mo(tfd-$COCF_3$)$_3$, where the isosbestic point is observed at 700 nm up to a dopant

concentration of 8 mol %. However, due to a narrower concentration span, the emergence of a second isosbestic point at higher wavelengths is not visible and would require more spectra of the polymer doped with higher concentration of Mo(tfd-$COCF_3$)$_3$ to confirm its presence. Spectra that feature an isosbestic point at 900 nm, p($g_4$2T-T) doped with H-TFSI up to 10 mol % and Mo(tfd-$COCF_3$)$_3$ up to 8 mol %, were used to determine the carrier density in these samples. The estimation yielded a carrier density of 1.5 – 2.8 · 10^{26} m^3 for p($g_4$2T-T) doped with H-TFSI, while doping with Mo(tfd-$COCF_3$)$_3$ resulted in carrier densities ranging from 0.5 – 2.7 · 10^{26} m^3. For samples where the charge carriers exclusively consist of polarons, the electrical conductivity increases with carrier density (Fig. 6.1c). For

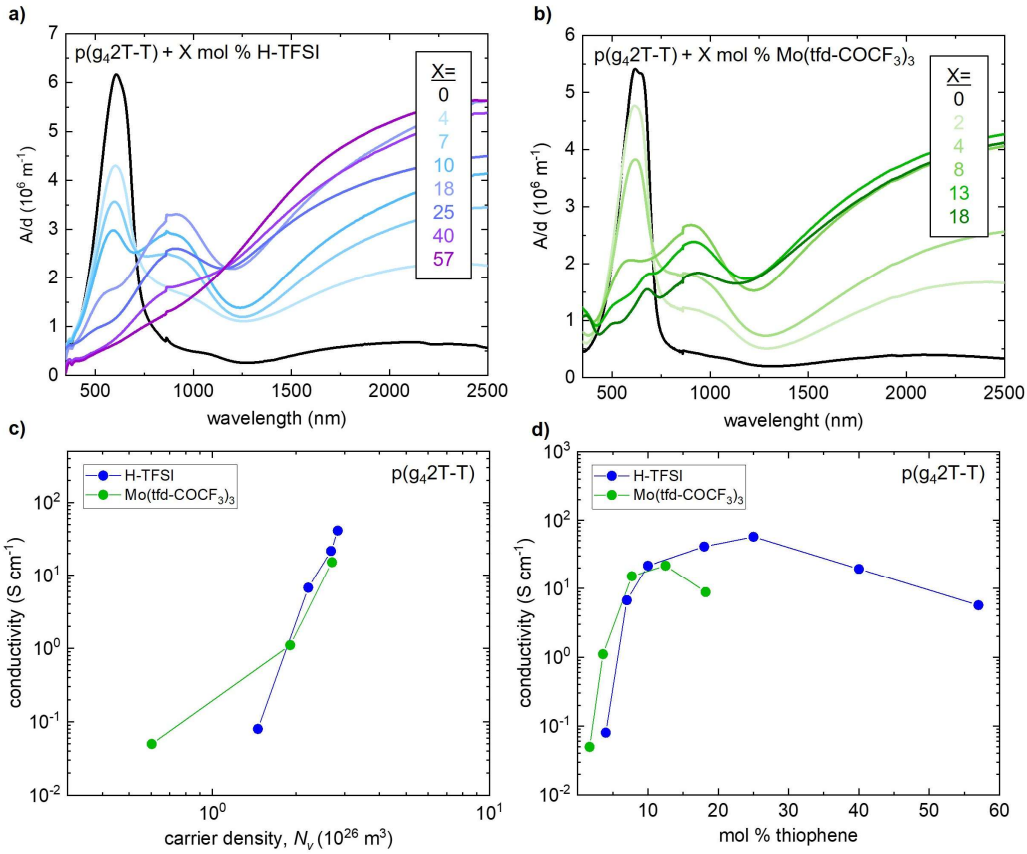

Figure 6.1. a) and b), thickness normalized UV-Vis-NIR absorbance spectra of p($g_4$2T-T) doped with H-TFSI and Mo(tfd-$COCF_3$)$_3$, respectively. c) electrical conductivity versus mol % dopant and d) electrical conductivity versus carrier density for p($g_4$2T-T) doped with H-TFSI and Mo(tfd-$COCF_3$)$_3$. The dopant concentration is calculated per thiophene unit of p($g_4$2T-T).

p($g_4$2T-T) doped with Mo(tfd-$COCF_3$)$_3$, the data align with the power law trend introduced in Chapter 3. However, a notable deviation occurs for p($g_4$2T-T) doped with H-TFSI. The slope of this data indicates a more pronounced increase in conductivity with charge density, suggesting that the charges in the samples doped with H-TFSI have higher mobility. A potential explanation for this difference in mobility could be attributed to variations in the doping process. While doping with Mo(tfd-$COCF_3$)$_3$ involves direct electron transfer with the polymer, leading to the formation of charge carriers and the dopant counterion, H-TFSI, being an acid may at least in part lead to protonation of the backbone of p($g_4$2T-T). However, the primary doping mechanism is to mediate redox doping of the polymer through atmospheric oxygen, in line with the observations made by Hofmann et. al.[98], indicating that high electrical conductivity is only achieved when the material is exposed to air. Another plausible explanation could be related to the energy levels of Mo(tfd-$COCF_3$)$_3$, which facilitates double charge transfer with p($g_4$2T-T) (Chapter 8) which results in the formation of dianions. Since dianions act as stronger Coulomb traps than monoanions, this could lead to lower carrier mobilities in p($g_4$2T-T) doped with Mo(tfd-$COCF_3$)$_3$. However, it is important to consider that Mo(tfd-$COCF_3$)$_3$ has a larger size than H-TFSI, which might reduce the Coulomb binding to some extent. Moreover, differences in sample processing should not be overlooked. While both dopants were co-processed with the polymer, the films of p($g_4$2T-T):H-TFSI were prepared through wire-bar coating, whereas p($g_4$2T-T):Mo(tfd-$COCF_3$)$_3$ were cast using spin coating. Examining the neat spectra of p($g_4$2T-T) in Figure 6.1a and 6.1b reveals structural differences, suggesting that the microstructure induced in p($g_4$2T-T): H-TFSI through wire-bar coating may be advantageous for carrier mobility.

When comparing the electrical conductivity and the dopant concentration, an interesting observation emerges. The conductivity increases up to a certain dopant concentration but then starts to decrease. For p($g_4$2T-T) doped with H-TFSI, the electrical conductivity rises with dopant concentration up to 25 mol % H-TFSI, reaching a value of (58 ± 3) S cm^{-1}. Intriguingly, despite a further increase in oxidation level, as evidenced by UV-vis spectroscopy (Fig. 6.1d), the conductivity drops to (20 ± 1) S cm^{-1} at 40 mol % H-TFSI and further decreases to (6 ± 1) S cm^{-1} at 57 mol%. The same trend is apparent for p($g_4$2T-T) doped with Mo(tfd-$COCF_3$)$_3$. Examination of the UV-vis spectra indicates a clear increase in oxidation level with increasing in dopant concentration. However, despite the increasing oxidation level, the conductivity initially increases, reaching a peak value of (22 ± 2) S cm^{-1} at 13 mol % dopant. Beyond this point, the conductivity begins to decline, reaching (9.0 ± 0.2) S cm^{-1} at 18 mol%. This observed decline in conductivity could be attributed to the formation of bipolarons/polaron pairs in the system, as they tend to be less mobile.[84] Another contributing factor might be a change of the microstructure in the samples or dopant aggregates disrupting the film nanostructure. For p($g_4$2T-T):Mo(tfd-$COCF_3$)$_3$, electron tomography analysis reveals dopant clustering with increasing dopant concentration. As the

dopant concentration increases, the clusters become larger, and form elongated structures. Notably, the shape of these clusters allows all dopant molecules to remain in contact with the surrounding polymer matrix, ensuring they are not spatially prevented from engaging in electron-transfer reactions with the polymer, despite clustering. In line with these results, the oxidation level of the polymer increases with dopant concentration as evident from the UV-vis spectra. However, the presence of these clusters might have adverse effects on the nanostructure of the polymer film and, consequently, its conductivity. In case of p($g_4$2T-T) doped with H-TFSI, GIWAXS analysis underscores that co-processing with small amounts, 4 and 7 mol % H-TFSI, induces a significant increase in order within the polymer through π-stacking. However, the order within the polymer film is progressively diminishing as the concentration increases further, with almost no π-stacking observed at 40%. This shift in polymer order is considered a potential contributor to the observed decrease in conductivity.

In summary, this study provides valuable insights into the interplay of doping, carrier density, and conductivity in p($g_4$2T-T), shedding light on the nuanced factors influencing the electronic properties of doped conjugated polymers. These findings contribute to the broader understanding of organic semiconductor behavior and pave the way for optimizing their performance in electronic devices.

Chapter 7

EXTINCTION COEFFICIENT IN THE INFRA-RED REGION

The central focus of this chapter is on determining the carrier density in p($g_4$2T-T) doped with F_4TCNQ and F_2TCNQ, achieved through the analysis of CN-stretch absorption peaks in the IR spectral region. Utilizing the estimated carrier densities, I explore the intricate interplay between molecular doping, the generation of mono- or divalent counterions, and their collective impact on the mechanical behavior of the polymer.

The glycolated polymer p($g_4$2T-T) exhibits a low ionization energy (IE^0 ≈ 4.6 eV)[124], which enables double doping by F_4TCNQ. This implies that the polymer can undergo electron transfer with both neutral F_4TCNQ (EA^0 ≈ 5.2 eV) and its anion (EA^- ≈ 4.7 eV), giving rise to the formation of F_4TCNQ dianions.[65] In contrast**,** when considering the energy levels of F_2TCNQ (EA^0 ≈ 5.1 eV, EA^- ≈ 4.5 eV), it becomes evident that only single electron transfer is feasible with p($g_4$2T-T).[65] Consequently, this only leads to the formation of anions. As previously introduced in Chapter 4, the anions of the dopants F_4TCNQ and F_2TCNQ exhibit absorption features within the same spectral region where the P2 polaron peak of the polymer conventionally emerges upon doping. Consequently, estimating the polaron density using ε_{P2} for polymers doped with F_4TCNQ, F_2TCNQ is challenging. However, the CN-stretch in F_4TCNQ and F_2TCNQ results in distinctive absorption peaks on top of the P1 polaron peak, detectable through FTIR spectroscopy. The characteristics of these absorption features depend on the molecular state of the dopant — neutral, anionic or dianionic. These peaks, along with their molar extinction coefficients, can be employed to estimate the polaron density.

In order to use the CN-stretch features, it is essential to correct the FTIR spectra by removing the underlying polaron signal. This correction process involves interpolating a baseline line to data points located just outside the CN-stretch peak area, as illustrated in Figure 7.1. Subsequently, for facilitating quantitative analysis, the resulting absorption is normalized by the sample thickness. To estimate the polaron density utilizing the CN-stretch peaks, it is essential that the polymer and dopant are co-processed from the same solution, ensuring that the dopant concentration is a known quantity. Figure 7.2a depicts the combination of UV-vis and FTIR spectra of thin film samples of p($g_4$2T-T) doped with

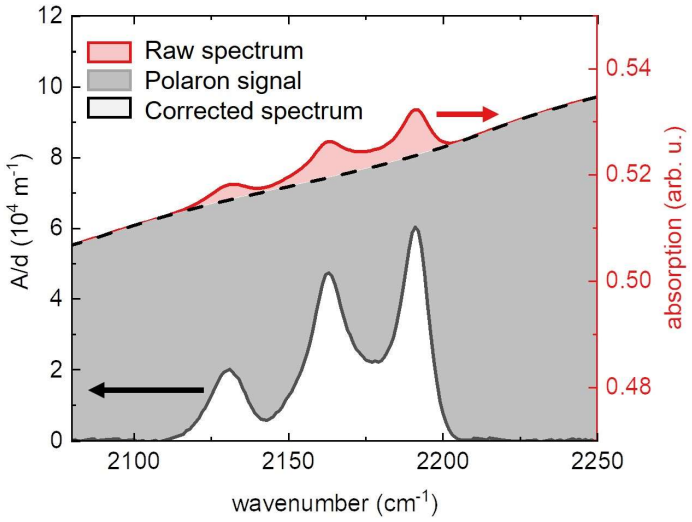

Figure 6.1. Raw FTIR spectrum of p($g_4$2T-T) film doped with 6 mol% F_4TCNQ (red), baseline (black, dashed) by interpolating a baseline line to data points just outside the peak area and spectra corrected for the underlying polaron signal where the absorption is normalized by sample thickness (black).

increasing concentrations of F_4TCNQ. The corresponding corrected FTIR spectra, specifically highlighting the CN-stretch vibrations are presented in Figure 7.2b. At low dopant concentrations (3 mol % and 6 mol %), the FTIR spectra display features from both the dianion (2130 cm^{-1}) and the anion (2155 cm^{-1}) (see Section 4.3). I assumed that, at these concentrations, each dopant molecule undergoes electron transfer with the polymer (single or double). To assess the relative proportion of dianions to anions, a comparison was made between the absorption peak intensities and their corresponding molar extinction coefficients obtained from FTIR signals recorded for solutions of lithium and dilithium salts of F_4TCNQ, which are depicted in Figure 4.4a. As a result, it was determined that in the p($g_4$2T-T) samples doped with 3 mol % and 6 mol % F_4TCNQ, 87 % and 37% of the dopant molecules were present as dianions, respectively. Utilizing this information and the number of added dopant molecules, the value of N_v was calculated for these samples. For higher dopant concentrations (10-30 mol %), the assumption that all dopants undergo electron transfer could not be made. However, these samples displayed CN stretch features solely attributed to F_4TCNQ^-, indicating the absence of dianions. In this scenario, with knowledge of the number of anions in the 3 mol % and 6 mol % samples, N_v was estimated by comparing the relative peak heights of the anion peak. Thus, in samples with 10-30 mol% dopant, N_v was estimated by comparing the intensity of the CN-stretch absorption around 2190 cm^{-1} with the intensity recorded for 6 mol% dopant, where the number of anions was known. A

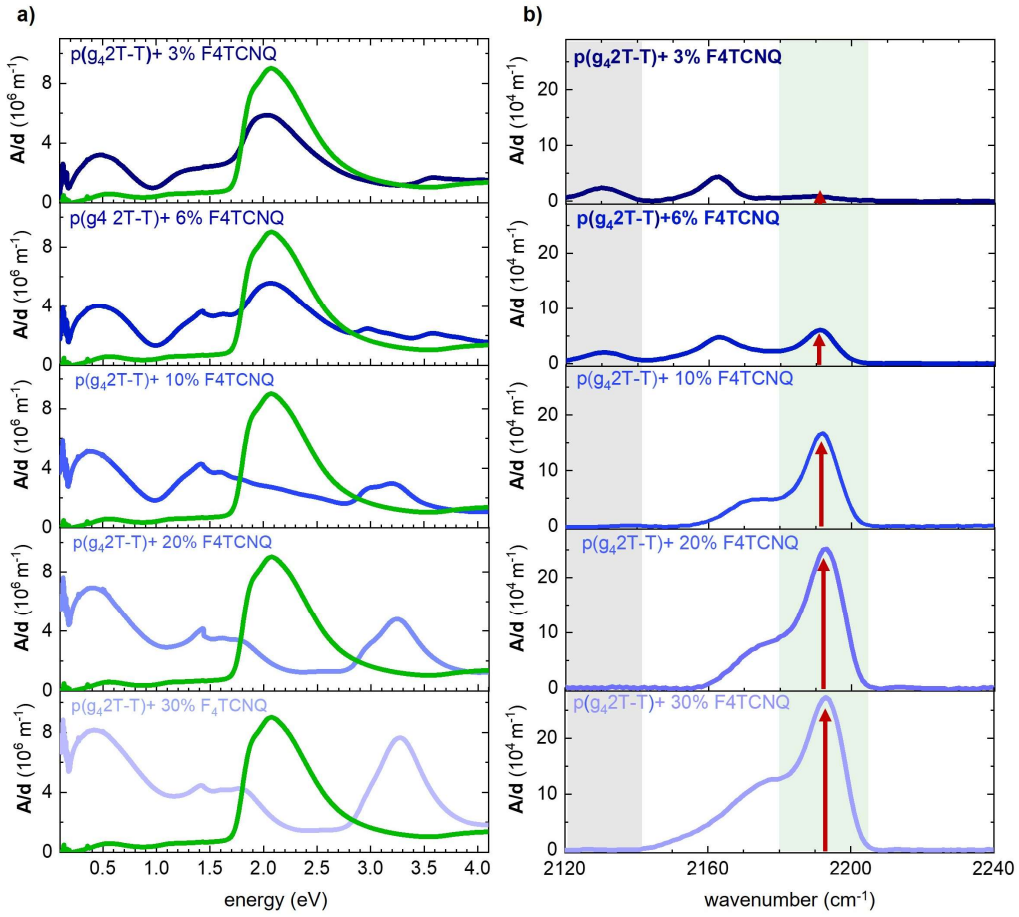

Figure 7.2. a) Uv-vis + FTIR absorbance spectra and (b) corrected FTIR absorbance spectra, with the absorbance A normalized by the film thickness d, of p($g_4$2T-T) before (green) and after doping with 3 mol %, 6 mol %, 10 mol %, 20 mol % and 30 mol % F_4TCNQ (blue). Reproduced from Ref. 101 with permission from the Royal Society of Chemistry.

similar methodology was employed to estimate N_v in samples doped with F_2TCNQ, with the distinction that, since F_2TCNQ only forms anions, a 100% ionization efficiency was assumed for dopant concentrations of 3% and 6%. The combination of UV-vis and FTIR spectra of thin film samples of p($g_4$2T-T) doped with increasing concentrations of F_2TCNQ and the corresponding corrected FTIR, specifically highlighting the CN-stretch vibrations, are presented in Figure S8 of Paper II[101]. Subsequently, N_v was utilized to calculate the oxidation level (O_{ox}), i.e., the number of charges per thiophene ring in percent, and the ionization efficiency (η_{ion}) in all samples (Table 7.1). Determining the oxidation level provides an avenue to investigate how doping influences the material properties.

The polymer p($g_4$2T-T) has a low elastic modulus of only ~8 MPa. For conjugated polymers characterized by low stiffness, the potential of molecular doping extends beyond electrical properties.

Doping can also impact their mechanical properties, particularly the elastic modulus.[125, 126] Furthermore, a significant aspect to consider in terms mechanical stiffness is the presence of counterions within conjugated polymer-based materials. Previous studies have suggested that multivalent counterions can induce ionic-type cross-linking of the polymer chains, which subsequently influences the elastic modulus.[127, 128] Hence, based on the determined oxidation level, we explored the generation of multivalent counterions, and their collective impact on the mechanical behavior of the polymer.

Table 7.1. Electrical and mechanical properties of p($g_4$2T-T) doped with F_4TCNQ or F_2TCNQ: Oxidation level O_{ox}, Young's modulus E, strain at break ε_b, electrical conductivity σ, total number of charges N_v, total number of dopant molecules N_{dopant} and ionization efficiency $\eta_{ion} = N_v/N_{dopant}$. Reproduced from Ref. 101 with permission from the Royal Society of Chemistry. Young's modulus E and strain at break ε_b were measured and calculated by Dr. Sepideh Zokaei.

mol % dopant	O_{ox} (%)	E (MPa)	ε_b (%)	σ (S cm^{-1})	N_v (10^{26} m^{-3})	N_{dopant} (10^{26} m^{-3})	η_{ion} (%)
p($g_4$2T-T)							
0	0	8 ± 2	130 ± 43	-	-	-	-
p($g_4$2T-T) + F_4TCNQ							
3	5.7 ± 0.1	24 ± 4	30 ± 5	0.3 ± 0.1	1.6	0.85	183
6	8.7 ± 0.1	53 ± 6	29 ± 8	5.0 ± 0.3	2.4	1.75	137
10	11 ± 0.2	148 ± 20	30 ± 2	30.4 ± 2.1	3.1	3.05	100
20	16.8 ± 0.3	207 ± 6	24 ± 3	42.2 ± 1.1	4.6	6.86	67
30	18.2 ± 0.3	232 ± 16	54 ± 3	51.8 ± 2.9	5.0	10.3	43
p($g_4$2T-T) + F_2TCNQ							
3	3.1± 0.1	8 ± 2	93 ± 20	0.1 ± 0.1	0.85	0.85	100
6	6.4 ± 0.1	31 ± 2	50 ± 10	1.4 ± 0.1	1.75	1.75	100
10	8.4 ± 0.1	138 ± 28	17 ± 3	9.4 ± 0.3	2.3	3.05	76
20	11.9 ± 0.2	377 ± 85	35 ± 10	25.9 ± 6.9	3.3	6.86	48
30	13.5 ± 0.2	212 ± 44	12 ± 1	12.3 ± 0.1	3.7	10.3	32

According to the data presented in Table 7.1, a dopant concentration of 3 mol% F_4TCNQ resulted in an ionization efficiency of 187%, indicating that the majority of dopant molecules generated two polarons, resulting in an O_{ox} of approximately 5.8%. In contrast, a dopant concentration of 6 % F_2TCNQ, assuming a 100% ionization efficiency, yielded an estimated O_{ox} of 6.4%. As a result of having samples with comparable O_{ox} , we were able to directly compare the mechanical properties of doped p($g_4$2T-T) compensated with counterions carrying a charge of -1 (F_2TCNQ anions) or -2 (F_4TCNQ dianions) (Fig. 7.3). Interestingly, the tensile deformation resulted in a comparable Young's modulus for both samples, suggesting that the charge of the counterion does not affect the stiffness of the polymer. However, the results from the tensile deformation tests reveal that p($g_4$2T-T) doped with F_2TCNQ exhibits a much larger strain at break ε_b ≈ (50 ± 10) % compared to doping with F_4TCNQ, where ε_b ≈ (30 ± 5) %. This implies that the higher concentration of monoanions, in contrast to dianions, positively influenced the toughness of p($g_4$2T-T). A comparable phenomenon was observed in a study by Murray et. al.[129] involving electrochemically doped polypyrrole (PPy) compensated with either monovalent Na^+ or divalent Mg^{2+} counterions from the electrolyte. Initially, at high oxidation level, both PPy samples displayed brittle behavior. However, upon reduction, the PPy sample compensated with Na^+

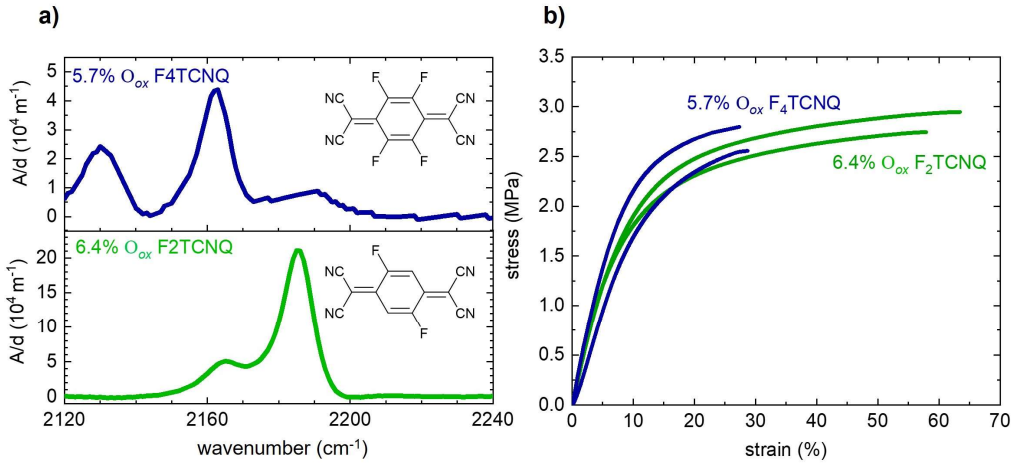

Figure 7.3. a) Transmission FTIR absorbance spectra, with the absorbance normalized by the film thickness A/d, of p($g_4$2T-T) doped with 3 mol% F_4TCNQ (blue; O_{ox} = 5.7%) and 6 mol% F_2TCNQ (green; O_{ox} = 6.4%); (b) stress–strain curves recorded at room temperature by tensile deformation of freestanding samples of p($g_4$2T-T) doped with 3 mol% F_4TCNQ (blue) and 6 mol% F_2TCNQ (green). Reproduced from Ref. 101 with permission from the Royal Society of Chemistry. The mechanical analysis was performed by Dr. Sepideh Zokaei.

demonstrated a transition to ductile behavior while the PPy that took up Mg^{2+} remained brittle. The authors attributed the difference in behavior between the samples to the effect of ionic crosslinking in the sample compensated with divalent counterions. Doping does not only alter the mechanical properties of the polymer in its solid state but also influences the characteristics of the solution during co-processing. Notably, I have observed a correlation between increasing dopant concentration and the viscosity of a solution of p($g_4$2T-T). At high dopant concentration, the solutions display gel-like behavior. This viscosity trend is consistent in both p($g_4$2T-T) doped with F_4TCNQ and F_2TCNQ, prompting an exploration into the underlying mechanisms governing this behavior. The key questions revolve around whether the increase in viscosity is a result of the stiffening of polymer chains upon oxidation, and whether the presence of multivalent anions contributes to this phenomenon. To investigate the effect of dopant concentration on the mechanical characteristics of a co-processed solution, oscillatory shear rheometry was conducted for solutions of p($g_4$2T-T) and F_4TCNQ or F_2TCNQ. The initial results are displayed in Figure 7.4. As a comparison, a solution of neat p($g_4$2T-T) with the same polymer concentration as in the polymer/dopant solutions was also measured. The experimental details can be found in Appendix I. Initially, the progression of the increase in viscosity was examined by monitoring the storage modulus (*G'*) as a function of time, starting 30 seconds post mixing of the stock solutions of the polymer and the dopant. The results indicate a significantly higher *G'* for solutions of p($g_4$2T-T) co-processed with F_4TCNQ or F_2TCNQ compared to the solution of only p($g_4$2T-T) (Fig 7.4a). The increase in *G'* appears nearly instantaneously and remains constant with only a minor increase during the measurement time. Moreover, the increase in storage modulus seams to depend

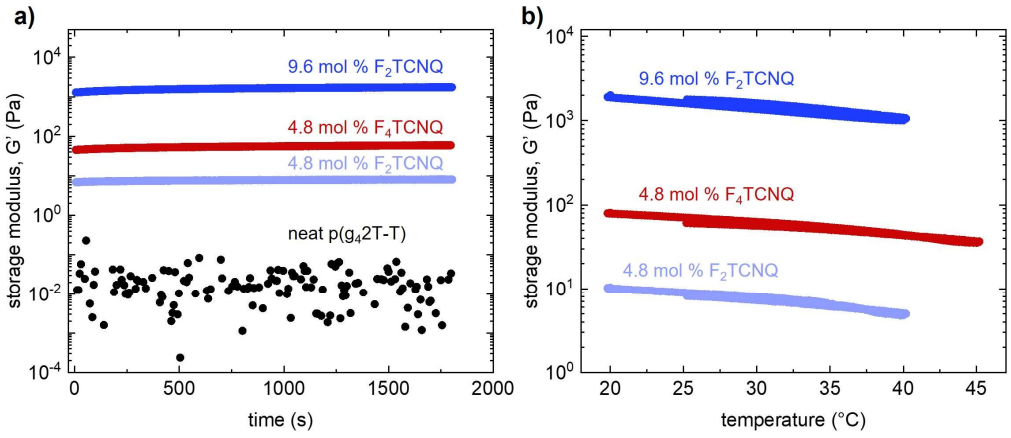

Figure 7.4. Unpublished data. The storage modulus, *G',* versus (a) time and (b) temperature for solutions of p($g_4$2T-T) doped with F_4TCNQ (4.8 mol %) and F_2TCNQ (4.8 and 9.6 mol %) in AcN:$CHCl_3$ (1:1, v/v).

on the dopant concentration. For solutions of p($g_4$2T-T) and F_2TCNQ, *G'* increases by two orders of magnitude going from a dopant concentration of 4.8 mol % to 9.6 mol %. A comparison between p($g_4$2T-T) solutions containing the same molar concentration (4.8 mol %) of F_4TCNQ and F_2TCNQ reveals a one order of magnitude higher *G'* for the solution co-processed with F_4TCNQ. Evident from the FTIR spectra in Figure 7.2b, a solid-state sample of p($g_4$2T-T) doped with 4.8 mol % F_4TCNQ displays some degree of dianion formation. Since the FTIR spectra in Figure 7.3b suggest some degree of dianion formation in a solid-state sample of p($g_4$2T-T) doped with 4.8 mol % F_4TCNQ, the presence of divalent ions in the solution can be anticipated, which could potentially explain the higher *G'*. However, confirmation of the presence of dianions in this solution is needed to arrive at a more conclusive determination. It is noted that the increase in *G'* is not solely dependent on counterion valency, as *G'* also increases with dopant concentration for F_2TCNQ, which forms only monovalent anions. The stiffening of the polymer backbone upon oxidation is proposed as a explanation for the observed increase in *G'*. Additionally, *G'* of co-processed solutions was studied as a function of temperature (Fig. 7.4b). Transitioning from 20 to 40 °C, all solutions exhibited a minor decrease in modulus with almost no hysteresis upon cooling the solutions back down to 25 °C. These results suggest that the mechanical characteristics of the polymer:dopant solutions are not significantly influenced within the temperature window of 20 – 40 °C.

I have also examined the impact of p($g_4$2T-T) concentration on the formation of F_4TCNQ anions/dianions in polymer:dopant solutions, utilizing FTIR spectroscopy to analyze the CN-stretch peaks. The spectra reveal a certain degree of dianion formation in the solutions. Interestingly, the relative amounts of F_4TCNQ^- and $F4TCNQ^{2-}$ remain consistent across a range of polymer concentrations, varying between 10 and 25 g L^{-1} in the solution (Fig. 7.5a). As the polymer concentration increases, there is a corresponding decrease in the molar concentration of F_4TCNQ, dropping from 14 mol% per thiophene unit at a p($g_4$2T-T) concentration of 10 g L^{-1} to 6 mol% at a p($g_4$2T-T) concentration of 25 g L^{-1}. The observed independence of the relative amounts of F_4TCNQ^- and F_4TCNQ^{2-} on polymer concentration argues against the influence of dianions on storage modulus as there is no significant amount of dianions present in the samples.

Analyzing a thin film of p($g_4$2T-T) co-processed with 5 mol % F_4TCNQ using temperature-variable FTIR spectroscopy reveals a temperature dependence in the relative amounts of F_4TCNQ^- and F_4TCNQ^{2-} in the film (Fig. 7.5b). At -100 °C, the FTIR spectrum predominantly displays CN-stretch features arising from F_4TCNQ dianions, a pattern consistent up to 20 °C. However, upon heating the sample to 100 °C, the spectra show characteristics of CN-stretch vibrations from both anions and dianions. A change in equilibrium toward anions would result in a decrease in oxidation level, due to a decrease in charge

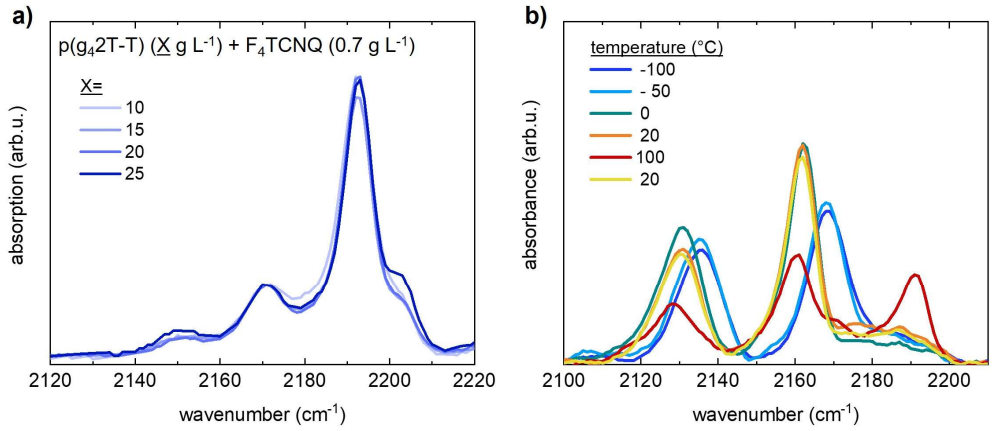

Figure 7.5. Unpublished data. a) Transmission FTIR absorbance spectra of solutions containing 0.7 g L^{-1} F_4TCNQ and p($g_4$2T-T) with a concentration ranging between 10 – 25 g L^{-1}. b) FTIR spectra of a thin film of p($g_4$2T-T) doped with 5 mol % F_4TCNQ measured at temperatures ranging between -100 and 100 °C.

carriers in the polymer. Consequently, this would lead to a decrease in conductivity. However, analyzing whether this decrease in carrier density affects the electrical conductivity of the sample is challenging, given that an increase in temperature typically results in increased carrier mobility. Reflecting on the discussions of the results presented in Figure 7.3, the transition from divalent to monovalent counterions might contribute to increased ductility in the material. It is worth noting that F_4TCNQ tends to sublime above 40 °C. Notably, based on the spectra presented in Figure 7.5b, this does not seem to be the case, as the spectra for 20 °C look the same before and after heating the sample up to 100 °C. This observation indicates the thermal stability in terms of sublimation of F_4TCNQ when incorporated into p($g_4$2T-T), a finding which has also been confirmed by Kroon et.al.[130] Looking ahead, considering dopant stability, it might be advantageous to explore ion exchange doping. In this scenario, the F_4TCNQ counterion is replaced with another counterion that is unable of undergoing electron transfer with the polymer and only serves to counterbalance the positive charge of the polarons in the polymer. This approach could potentially result in a system that is more stable with temperature.

In conclusion, this comprehensive but incomplete exploration sheds light on the intricate relationships between doping, electronic structure, and mechanical behavior of p($g_4$2T-T). The findings offer valuable insights for future material design, emphasizing the multifaceted impact of doping on electronic, rheological, and mechanical characteristics.

Chapter 8

EPR SPECTROSCOPY AND DOUBLE DOPING

As introduced in Chapter 2, certain dopant-polymer combinations can facilitate two electron transfer events between the polymer and the same dopant molecule, a phenomenon known as double doping. In the case of p-doping, charge transfer occurs from the polymer to the neutral dopant molecule and the dopant anion. Double doping offers an opportunity to significantly enhance the ionization efficiency, reaching a maximum of η_{ion} = 200% if each dopant contributes two charges. This has been observed for low-IE conjugated polymers doped with quinodimethane type dopants such as F_4TCNQ.[65] The benefit of this type of double doping is that two polarons can be created without increasing the size of the dopant.

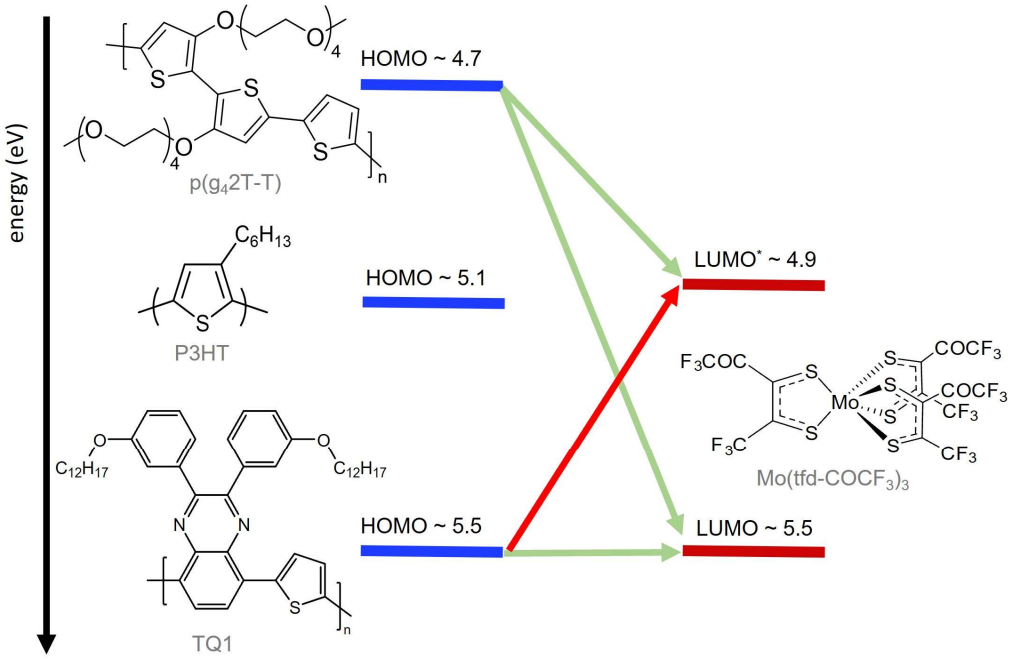

Figure 7.1. Energy diagram depicting the energy levels that are involved in the charge transfer process from the polymers p($g_4$2T-T), P3HT and TQ1 to the p-type dopant Mo(tfd-$COCF_3$)$_3$. Reprinted with permission from Ref. 131, CC-BY 4.0

There are other dopants, such as specific 19-electron organometallic sandwich compounds or benzoimidazoline radicals, capable of generating more than one polaron.[59] In addition, there are also multivalent radical cation salts, featuring two or four triphenylamine units, that can accept two or even four electrons from a conjugated polymer.[59, 63, 90] However, their larger molecular volume, at least twice that of related monomeric dopants, reduces the advantages of double doping by increasing the overall counterion volume. I believe that the most effective approach to achieve double doping involves avoiding an increase in the size of the dopant. This method requires adding fewer dopant molecules to achieve a specific polaron density, minimizing the risk of dopant aggregation, and reducing the impact of doping on the nanostructure of the polymer.

This chapter delves into the exploration of double doping and specifically investigates whether double doping, without the necessity of increasing the dopant size, is limited to monomeric quinodimethane-type dopants. The primary aim is to determine if this type of pf double doping extends as a more universal concept, demonstrating broader applicability to other chemical species. To address this question, I studied doping with the molybdenum-based dithiolene complex Mo(tfd-$COCF_3$)$_3$ (Fig. 8.1).[132, 133] This complex is capable of existing in both an anionic and a dianionic state, allowing it to undergo two charge transfer events. The neutral complex possesses an electron affinity of $\mathrm{EA}_{\mathrm{Mo(tfd-COCF_3)_3}}$ = 5.5 eV, while the anion exhibits an $\mathrm{EA}^{-}_{\mathrm{Mo(tfd-COCF_3)_3}}$ = 4.9 eV. The investigation extended to doping of three polymers, namely p($g_4$2T-T), P3HT and TQ1. The polymer p($g_4$2T-T), with a low ionization energy of $\mathrm{IE}_{\mathrm{p(g_4 2T-T)}}$ = 4.7 eV[124], was predicted to support two electron transfer events with Mo(tfd-$COCF_3$)$_3$, whereas TQ1, with a substantial $\mathrm{IE}_{\mathrm{TQ1}}$ = 5.5 eV, should only be able to accommodate a single electron transfer (Fig. 8.1). The ionization efficiency of P3HT, is reported to be $\mathrm{IE}_{\mathrm{P3HT}}$ = 5.1 eV.[111, 134-138] This value is comparable to the electron affinity of the Mo(tfd-$COCF_3$)$_3$ anion. This similarity implies that P3HT has the potential to undergo two electron transfer events with Mo(tfd-$COCF_3$)$_3$.

UV-vis-NIR spectroscopy of neutral Mo(tfd-$COCF_3$)$_3$ as well as its anion and dianion salt, [Mo(tfd-$COCF_3$)$_3$]$^-$$Et_4N^+$ and [Mo(tfd-$COCF_3$)$_3$]$^{2-}$(Et_4N^+)$_2$ (Fig. 8.2a), revealed absorption features at wavelengths coinciding with those typically observed for neat p($g_4$2T-T), P3HT and TQ1 or where polaronic absorbance peaks emerge upon doping (see Section 2.7 and Fig. 2.5). Consequently, the different species could not be conclusively distinguished using optical spectroscopy. To determine the presence of distinct species, I instead turned to EPR spectroscopy, which is a technique that can be used to identify unpaired spins, for example in polarons and anions, as described in Section 4.4. The unpaired electron spin in the Mo(tfd-$COCF_3$)$_3$ anion and the polaron experience different electronic environments. This could potentially lead to different electron g-factors. If the anion and the polaron

exhibit different g_e, it implies that they respond differently to an external magnetic field. As a result, they would absorb at different magnetic fields in the spectroscopic analysis. This divergence in absorption at different magnetic fields can be used as evidence to confirm the occurrence of double doping events.

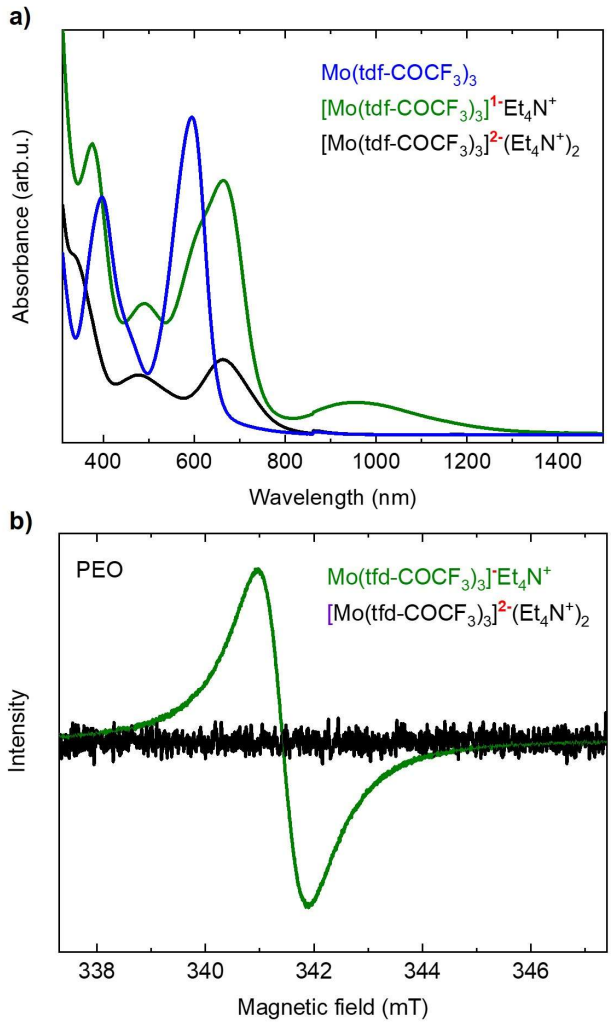

Figure 8.2. (a) UV-vis spectra of $Mo(tfd\text{-}COCF_3)_3$, $[Mo(tfd\text{-}COCF_3)_3]^-Et_4N^+$ and $[Mo(tfd\text{-}COCF_3)_3]^{2-}(Et_4N^+)_2$ in dichloromethane (DCM). (b) EPR spectra of $[Mo(tfd\text{-}COCF_3)_3]^-Et_4N^+$ and $[Mo(tfd\text{-}COCF_3)_3]^{2-}(Et_4N^+)_2$ dispersed in a polyethylene oxide (PEO) matrix. Reprinted with permission from ref. 131, CC-BY 4.0. The measurement of the EPR spectra and data processing was conducted by Dr. Till Biskup at Saarland University.

In an initial experiment, EPR spectra were recorded for the anion and dianion salts $[Mo(tfd\text{-}COCF_3)_3]^-Et_4N^+$ and $[Mo(tfd\text{-}COCF_3)_3]^{2-}(Et_4N^+)_2$ (Fig. 8.2b). The anion salt revealed a signal at 341.4 mT, confirming that the anion could be detected with EPR, while the dianion salt was spin silent. Doping of TQ1 was subsequently explored. Given its high IE, I anticipated only a single charge transfer with $Mo(tfd\text{-}COCF_3)_3$, resulting in the formation of $[Mo(tfd\text{-}COCF_3)_3]^-$, which is detectable through EPR. In addition, the dopant Magic Blue (chemical structure in Fig. 2.1) was introduced to the study, featuring the cation tris(4-bromophenyl)ammoniumyl with a notably high singly occupied HOMO of 5.7 eV, thereby allowing for doping of TQ1. Upon accepting an electron, this cation transitions into a neutral state and becomes spin silent, and due to the octet rule it cannot accept a second electron, consequently not generating an EPR signal. Therefore, the EPR spectrum of TQ1 doped with Magic Blue should exclusively feature the polaron signal. UV-vis-NIR spectroscopy confirmed that both $Mo(tdf\text{-}COCF_3)_3$ and Magic Blue could undergo charge transfer with TQ1, as evidenced by the polaron absorption band at 900 nm (Fig. 8.3a). EPR spectra of TQ1 doped with $Mo(tdf\text{-}COCF_3)_3$ exhibited two signals: one at 342.2 mT and another one at a lower magnetic field (Fig. 8.3b). The signal at 342.2 mT, appeared in the same position as the signal observed for TQ1 doped with Magic Blue (Fig. 8.3c). Consequently, the signal at 342.2 mT was assigned to the polaron. On the other hand, the signal at the lower magnetic field was assigned to the $Mo(tfd\text{-}COCF_3)_3$ anion, as it was coinciding with the position of the signal observed for $[Mo(tfd\text{-}COCF3)_3]^-Et_4N^+$ (Fig. 8.3b).

Having identified the absorption positions of the $Mo(tfd\text{-}COCF_3)_3$ anion, $[Mo(tfd\text{-}COCF_3)_3]^-$, and the polaron, I proceeded to investigate p($g_4$2T-T) doped with neutral $Mo(tfd\text{-}COCF_3)_3$ and its anion salt $[Mo(tfd\text{-}COCF_3)_3]^-Et4N^+$. UV-vis-NIR spectroscopy demonstrated the capability of both species to dope p($g_4$2T-T), as evidenced by the emergence of polaron absorption bands at 900 nm (Fig. 8.4a). The capability of p($g_4$2T-T) to undergo charge transfer with the anion salt suggests the potential for double doping in this system. This implies that the anion formed during the initial doping with the neutral complex may undergo a second charge transfer, further enhancing the doping effects. Nonetheless, doping with the neutral complex resulted in more prominent polaron absorption bands at 900 nm and enhanced electrical conductivity (σ = 19.6 ± 0.6 S cm^{-1}) in contrast to doping with the anion salt (σ = 11.9 ± 0.3 S cm^{-1}). As shown in Chapter 2, an increase in the P2 polaron absorption is indicative of a higher charge carrier concentration (Fig. 2.5), which would explain the difference in conductivity. The higher carrier density observed in the sample doped with $Mo(tfd\text{-}COCF_3)_3$ further implies the neutral complex can undergo double doping with p($g_4$2T-T). The EPR spectra of neat p($g_4$2T-T) as well as p($g_4$2T-T) sequentially doped with neutral $Mo(tfd\text{-}COCF_3)_3$ and $[Mo(tfd\text{-}COCF_3)_3]^-Et_4N^+$all revealed a polaron signal at 342.2 mT (Fig. 8.4b). In the case of neat p($g_4$2T-T), the signal can be attributed to oxidation by atmospheric oxygen. For p($g_4$2T-T) doped with the neutral complex, the recorded spectra exhibited a

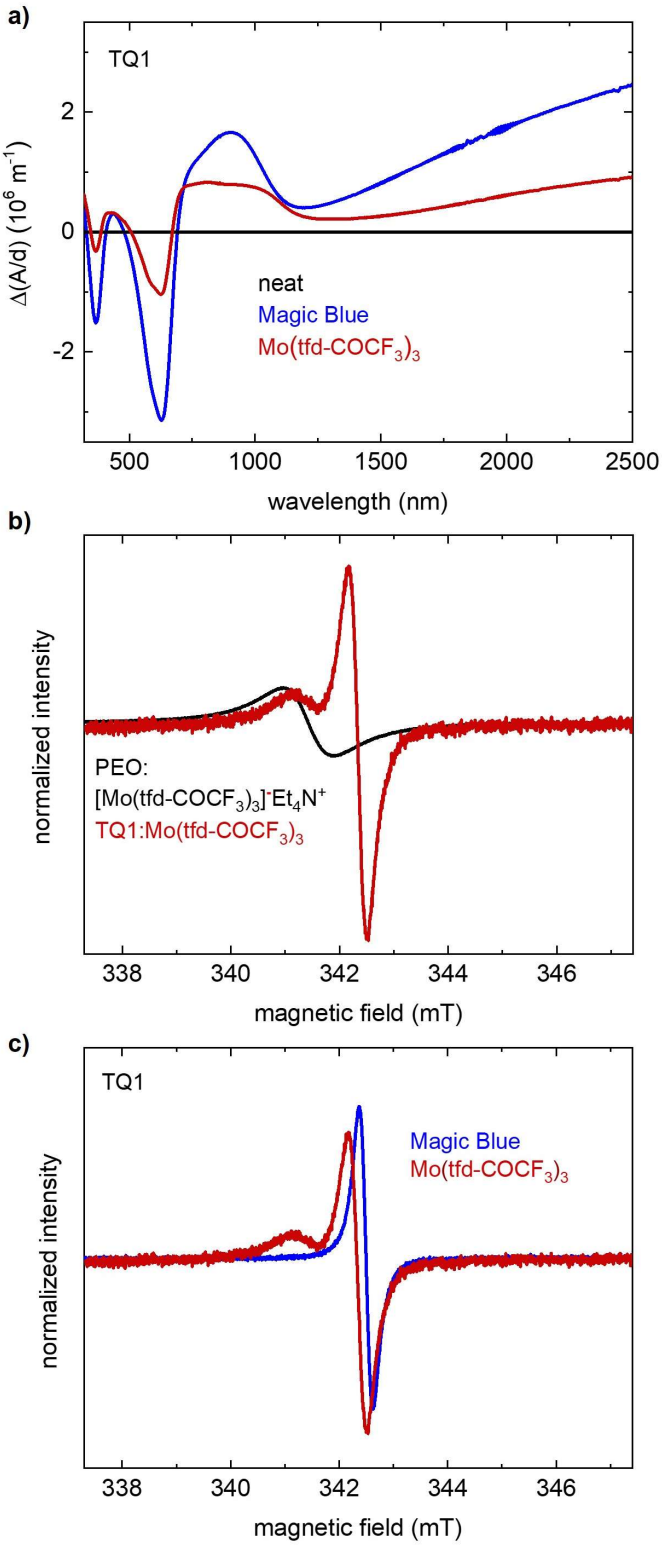

Figure 8.3. a) UV−vis−NIR absorbance spectra displaying the difference in thickness normalized absorbance Δ(A/d) between the spectra of pristine TQ1 and TQ1 doped with Magic Blue or $Mo(tfd\text{-}COCF_3)_3$. b) EPR spectra of $[Mo(tfd\text{-}COCF_3)_3]^-Et_4N^+$ dispersed in a PEO matrix and TQ1 doped with $Mo(tfd\text{-}COCF_3)_3$, normalized to the maximum in the field range [338, 341.5] mT. c) EPR spectra of TQ1 doped with Magic Blue or $Mo(tfd\text{-}COCF_3)_3$, normalized to the same amplitude. Reprinted with permission from Ref. 131, CC-BY 4.0. The measurement of the EPR spectra and data processing were conducted by Dr. Till Biskup at Saarland University.

broad shoulder around 341 mT. Since EPR spectra of $[Mo(tfd\text{-}COCF_3)_3]^-Et_4N^+$ revealed a signal in this field range, it is likely that EPR signal for p($g_4$2T-T) doped with the neutral complex is the superposition of the polaron and the dopant anion signals. The broadening towards lower magnetic fields is thus an indication of the presence of $[Mo(tfd\text{-}COCF_3)_3]^-$, suggesting that not every dopant underwent two electron transfers. The EPR spectra of p($g_4$2T-T), sequentially doped with the anion salt $[Mo(tfd\text{-}COCF_3)_3]^-Et_4N^+$, displayed a signal at a comparable position to that of the neat sample. This implies that there is no significant presence of $[Mo(tfd\text{-}COCF_3)_3]^-$. This is attributed to that a majority of monoanions accepted an electron and became spin-silent dianions. Additionally, I investigated p($g_4$2T-T) that was co-processed with varying amounts of neutral $Mo(tfd\text{-}COCF_3)_3$. The EPR spectra of these co-processed samples displayed a signal centered at 342.2 mT, the position associated with polarons (Fig. 8.4c). Notably, no broad shoulder at a lower magnetic field was observed, indicating the absence of a significant number of monoanions. Given that it is primarily the monoanion absorbing at the same wavelengths as the P2 polaron peak of p($g_4$2T-T) and considering the relatively low molar concentration of the dopant in the co-processed samples, I assumed that the charge density could be estimated from the P2 polaron peak in the UV-vis-NIR spectra by using ε_{P2}, as described in Chapter 4. The estimation of charge density yielded an ionization efficiency of more than 100% for all studied samples. Specifically, for samples with 5 mol % and 10 mol % dopant, η_{ion} approached 200 %. This substantial degree of double doping provides an explanation for the absence of any clear features of the monoanion in the EPR spectra of p($g_4$2T-T) co-processed with $Mo(tfd\text{-}COCF_3)_3$.

Additionally, I studied sequential doping of P3HT with Magic Blue, the neutral complex $Mo(tfd\text{-}COCF_3)_3$ and its anion salt $[Mo(tfd\text{-}COCF_3)_3]^-Et_4N^+$. UV-vis-NIR spectroscopy revealed that P3HT is susceptible to doping with Magic Blue and the neutral complex, as indicated by the emergence of absorption bands at 800 nm (Fig. 8.5a). In contrast, doping with $[Mo(tfd\text{-}COCF_3)_3]^-Et_4N^+$ only resulted in only minor electron transfer, with hardly any polaronic absorption features in this sample. EPR spectra of P3HT doped with Magic Blue exhibited a signal at 342.2 mT, coinciding with the positions of neat p($g_4$2T-T) and for TQ1 doped with Magic blue (Fig 8.5b). The spectra for P3HT doped with the monoanion salt displayed a broadening towards lower magnetic fields, indicating the presence of monoanions. Since UV-vis spectroscopy revealed minimal doping between P3HT and $[Mo(tfd\text{-}COCF_3)_3]^-Et_4N^+$, this broadening was attributed to monoanions that did not undergo charge transfer. In the EPR spectra for P3HT doped with the neutral complex the broadening of the signal towards lower magnetic fields is less pronounced as for doping with the monoanionic salt, suggesting a limited presence of anions. Despite this, the UV-vis spectra indicate a more substantial charge transfer between P3HT, and the neutral complex compared to doping with the monoanionic salt. Given that $[Mo(tfd\text{-}COCF_3)_3]^-Et_4N^+$ results in minor doping of P3HT, single electron transfer between P3HT and the neutral complex was

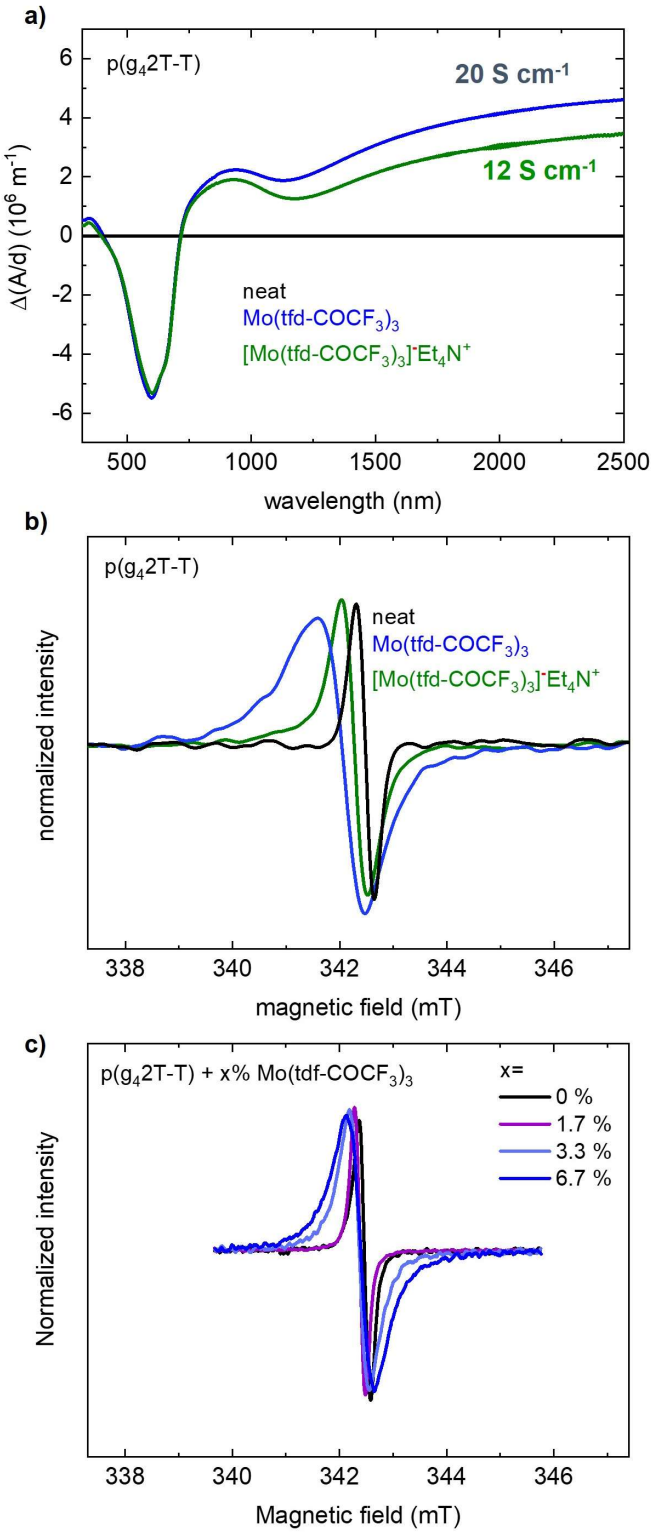

Figure 8.4. a) UV–vis–NIR absorbance spectra displaying the difference in thickness normalized absorbance Δ(A/d) between the spectra of pristine p($g_4$2T-T) and p($g_4$2T-T) sequentially doped with Mo(tfd-$COCF_3$)$_3$ or [Mo(tfd-$COCF_3$)$_3$]$^-$Et4N$^+$. b) EPR spectra of pristine p($g_4$2T-T) and p($g_4$2T-T) sequentially doped with Mo(tfd-$COCF_3$)$_3$ or [Mo(tfd-$COCF_3$)$_3$]$^-$Et$_4$N$^+$. c) EPR spectra of co-processed p($g_4$2T-T):Mo(tfd-$COCF_3$)$_3$ films. Reprinted with permission from Ref. 131, CC-BY 4.0. The measurement of the EPR spectra and data processing were conducted by Dr. Till Biskup at Saarland University.

expected. However, the absence of a significant number of monoanions in the EPR spectra suggests an alternative explanation: the neutral complex underwent a second charge transfer, transforming into spin-silent dianions. When comparing the EPR spectra of P3HT, p($g_4$2T-T) doped with Mo(tfd-$COCF_3$)$_3$, the lack of broadening in P3HT became more evident (Fig. 8.5c). The spectra for P3HT exhibits a slightly broader shoulder than for TQ1. However, the oxidation level in P3HT indicated by UV-vis spectroscopy suggests a more pronounced presence of monoanions in case of single electron transfer with Mo(tfd-$COCF_3$)$_3$. These findings imply that double charge transfer occurs upon doping with the neutral complex but not with the monoanion salt. It raises questions about the potential influence of the first electron transfer on the dielectric environment, possibly facilitating a second charge transfer from the monoanion. Alternatively, the first charge transfer might induce an increase in ordered domains in P3HT, lowering the IE, and thus facilitating the second charge transfer.

In conclusion, the findings in this chapter highlight the capability of the investigated dopant, Mo(tfd-$COCF_3$)$_3$, to undergo two charge transfer events with the conjugated polymer p($g_4$2T-T). This showcases the feasibility of double doping without necessitating an increase in dopant size, suggesting that double doping is a universal concept with broader applicability to other chemical species. The data also suggest the potential for double doping in P3HT with Mo(tfd-$COCF_3$)$_3$. However, further investigation is required to ascertain whether double charge transfer indeed occurs between P3HT and Mo(tfd-$COCF_3$)$_3$.

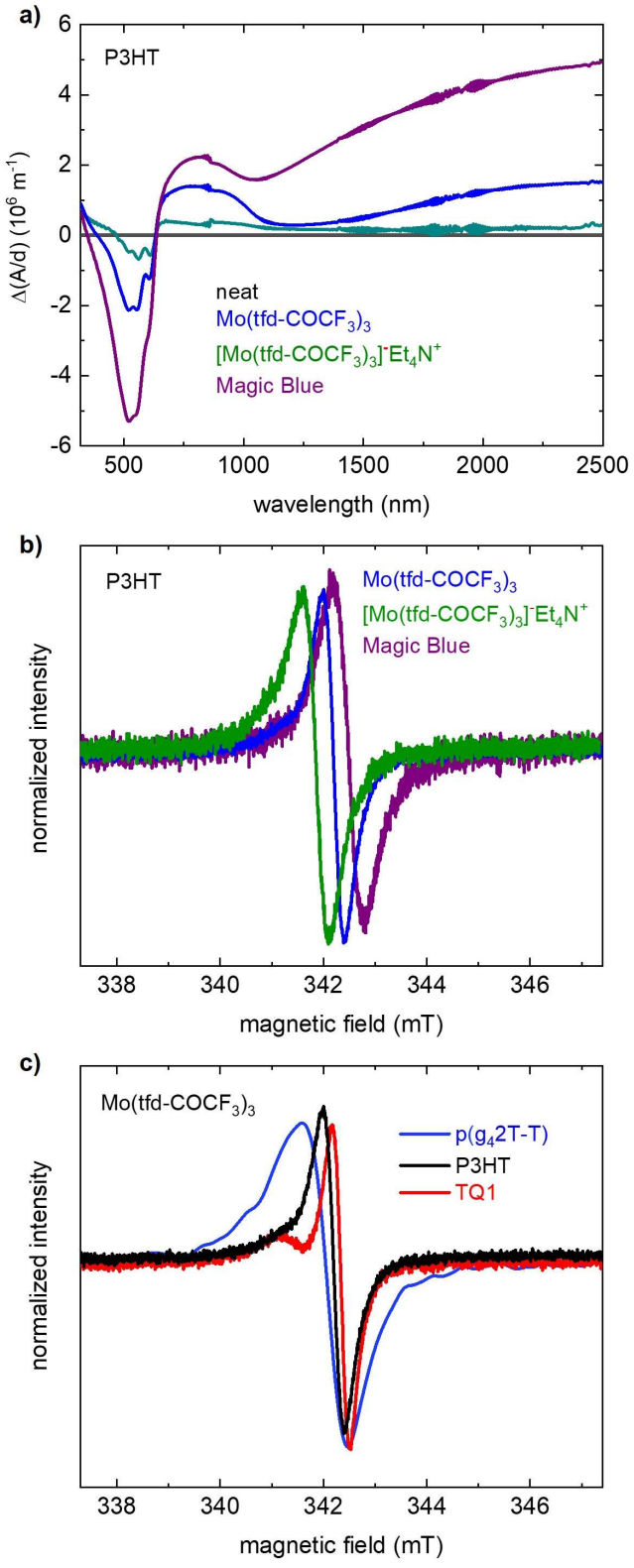

Figure 8.5. Unpublished data. a) UV−vis−NIR absorbance spectra displaying the difference in thickness normalized absorbance Δ(A/d) between the spectra of neat P3HT and P3HT doped with Magic Blue, $Mo(tfd\text{-}COCF_3)_3$ and $[Mo(tfd\text{-}COCF_3)_3]^-Et_4N^+$. b) EPR spectra P3HT doped with Magic Blue, $Mo(tfd\text{-}COCF_3)_3$ and $[Mo(tfd\text{-}COCF_3)_3]^-Et_4N^+$, normalized to the same amplitude. c) EPR spectra of $p(g_42T\text{-}T)$, P3HT and TQ1 doped with $Mo(tfd\text{-}COCF_3)_3$. The measurement of the EPR spectra and data processing were conducted by Dr. Till Biskup at Saarland University.

Chapter 9

COMPARISON OF THE EXTINCTION COEFFICIENT AND THE LANGMUIR ISOTHERM

This chapter delves into the comprehensive analysis of charge carrier density in conjugated polymers, comparing the data accumulated in this thesis with existing literature. In this thesis, the determination of charge carrier density was based on the intensity of absorption using the molar extinction coefficient. Primarily, a comparison of the intensity of polaron absorption and the intensity of the absorption of the neutral polymer at the identical wavelength, utilizing the molar extinction coefficient ε_{P2} (Chapter 6). In cases where carrier density was evaluated in polymers doped with quinodimethane-based dopants like F_4TCNQ and F_2TCNQ, the molar extinction coefficient of the CN-stretch was applied (Chapter 7). The findings from this thesis align closely with the carrier densities measured by Moulé et al [83] (Fig. 9.1). Their method is also based on the optical spectra but instead of studying the difference in absorption intensity they study the difference in absorption peak area. Their method revolves around determining the polaron mole fraction, Θ, by comparing peak areas for absorption of neutral polymer segments and oxidized polymer segments. The subsequent determination of carrier density is based on Θ, utilizing a Langmuir isotherm as introduced in Chapter 4. Both methods assume the absence of bipolarons/polaron pairs and rely on optical absorption spectra for determining carrier density.

Accurate estimation of carrier density is through analysis of the intensity of absorption requires precise measurement of sample thickness, and errors associated with the determined carrier densities in this thesis are primarily attributed to variations in thickness. Notably, Moulé et. al. employs an alternative approach that places less emphasis on thickness, as their measurements are relative for peaks within the same sample. To determine the absorption contribution arising from the neutral polymer and the polarons, they fitted the spectra with gaussians assuming that the sum of the total spectral area for the neutral and polaron component remain constant. However, the integral of polaron absorbance is found to be 0–50 % greater than that of the neutral sites. Consequently, the data is adjusted through normalization using a correction factor to address the enhanced absorption observed in the polaronic

state. Interestingly, despite these nuances, both methods yield similar results, underscoring the reliability of measuring carrier density through optical absorption spectra.

It is important to note that polymer:dopant systems studied by Moulé et. al. are different from the systems that I have studied in this thesis. This is particularly interesting given the diverse array of dopant molecules in terms of energy levels, size, and structure, coupled with variations in polymer energy levels, side chains, dielectric constant, and degree of order. Notably, the data aligns well despite these diverse factors. As depicted in Figure 9.1, a compelling trend emerges as carrier density increases, conductivity data converges for all studied conjugated polymers and dopants. This convergence strongly suggests that carrier density stands out as the dominant variable in influencing electrical transport. Consequently, it implies that carrier density plays a significant and pivotal role in controlling the electrical properties of the studied systems.

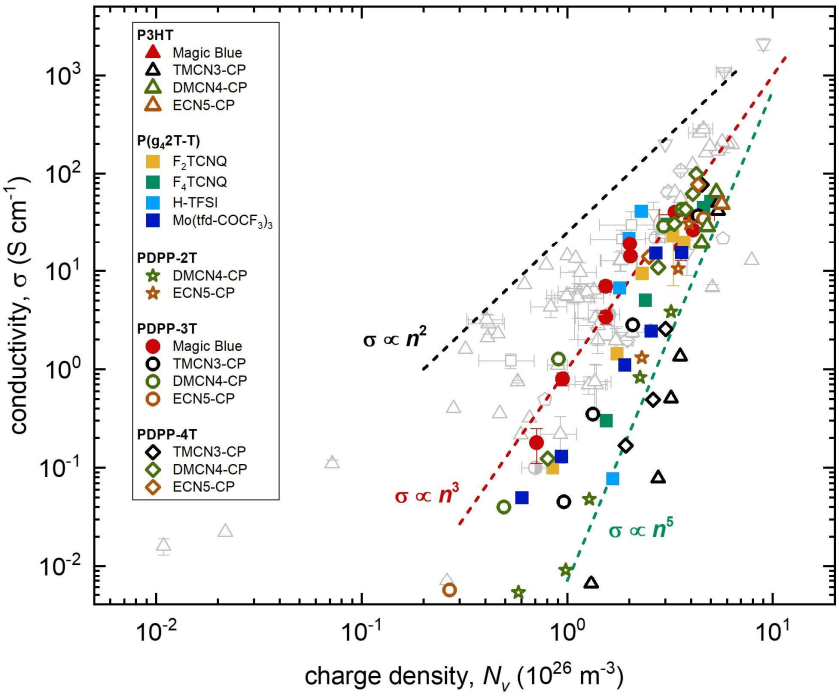

Figure 8.1. Conductivity σ as a function of charge density molecularly doped conjugated polymers. The closed colored symbols represent data from this thesis work. Open colored symbols represent data determined by Moulé et al.[83] Faded gray symbols were collected from literature (for references, see paper VI of this thesis). The dashed lines are power laws of varying slopes that were added to guide the eye. Reprinted with permission from Ref. 108, CC-BY 4.0.

Chapter 10

CONCLUSION AND OUTLOOK

This thesis has advanced the understanding of doped polymers by exploring various methods for assessing polaron density. By conducting a comprehensive examination of electric and spectroscopic techniques, valuable insights have been gained with respect to the estimation of the number of charges in these materials. A central focus has been on spectroscopic techniques, in particular UV-vis spectroscopy, FTIR spectroscopy and EPR spectroscopy. By employing these spectroscopic methods, this thesis aimed to address the following questions:

- Can optical methods effectively estimate polaron density?
- To what extent does chemical doping affect the mechanical properties of conjugated polymers?
- Is the concept of multiple electron transfer between the dopant and the conjugated polymer a universally applicable concept?

The study of spectroscopic methods revealed promising avenues for estimating polaron density. Through analysis of optical spectra, it was shown that the polaron density in chemically doped conjugated polymers can efficiently be determined using the molar extinction coefficient of the P2 polaron peak. However, this method is not without limitations. At low levels of polymer oxidation, the low intensity of polaron absorption leads to decreased sensitivity. Furthermore, the presence of bipolarons/polaron pairs in the system poses a challenge, limiting the determination of carrier density at high polymer oxidation. In polymers doped with the quinodimethane-type dopants F_4TCNQ and F_2TCNQ, the carrier concentration could be determined utilizing the molar extinction coefficient of CN-stretch. It is noteworthy that the findings of this thesis closely align with the carrier densities measured through optical methods by Moulé et al, underscoring the reliability of measuring carrier density through optical absorption spectra.

Looking ahead, it is essential to address the challenges posed by the presence of bipolarons/polaron pairs when estimating the carrier density using optical spectra. Developing a method capable of accounting for bipolaron/polaron pair formation would greatly enhance our understanding of the

carrier density in doped polymers. One potential approach could involve utilizing spectro-electrochemistry in combination with chronoamperometry across a wider potential span, encompassing potentials where bipolaron/polaron pair formation occurs. In this approach, spectra displaying absorption features solely from polaron absorption, along with the number of injected charges, would be used to calculate the molar extinction coefficient of the polaron. By knowing the molar extinction coefficient for the polaron and the number of injected charges from chronoamperometry, it may be possible to extract information about the number of bipolarons/polaron pairs. Building upon methodologies such as approaches for spectral fitting proposed by the research groups of Natalie Banerji, Frank Spano, Adam Moulé, and Benjamin Schwartz holds promise in this endeavor, providing a pathway to enhance the precision and reliability of carrier density measurements in doped polymer systems.[70, 83-85]

Regarding mechanical properties, particularly in polymers with low modulus, chemical doping has been shown to significantly increase the stiffness of the polymer p($g_4$2T-T). Additionally, the valency of the dopant counterions has been identified as a significant factor affecting the ductility of the polymer, with monovalent anions enhancing ductility compared to divalent anions. Furthermore, preliminary results suggest that chemical doping notably influences the rheological properties of polymer/dopant systems in solution, with an increase in storage modulus observed with increasing dopant concentration. However, further investigation is needed to understand to which extent the valency of the dopant influences the rheological response. In a continued examination of polymer:dopant systems in solution, it is relevant to compare solutions of p($g_4$2T-T) and F_4TCNQ/F_2TCNQ with similar oxidation levels at dopant concentrations where F_4TCNQ display some degree of dianion formation. If the valency of the dopant counterion influences the rheological properties, it would be intriguing to broaden this investigation to include other polymer:dopant systems in solution.

A notable aspect of this study has been the concept of double doping without an increase in dopant size. It has been confirmed as a universal concept with broader applicability beyond quinodimethane-type dopants. The investigated dopant, Mo(tfd-$COCF_3$)$_3$, was shown to be able to undergo two electron transfer events with the conjugated polymer p($g_4$2T-T). Additionally, the results also indicate double doping in P3HT with Mo(tfd-$COCF_3$)$_3$, although further investigation is required to confirm this. Double doping presents a significant advantage by enabling an increase in carrier density without a corresponding rise in the number of dopant molecules. Looking ahead, it would be interesting to explore other polymer-dopant combinations that utilize this strategy. Such investigations would offer further insights into tuning the carrier density of conjugated polymers while minimizing the need for

additional dopant molecules. This approach does not only lead to greater control over the electronic properties of materials, but it does also reduce the influence on the nanostructure of the material.

However, this study has also unveiled the influence of double doping on the mechanical properties of the polymer, attributed to the formation of dianions. Specifically, the presence of dianions tends to make the material more brittle compared to monoanions. In a recent publication by our group, in-plane drift of counterions in moderate electric fields was employed to create lateral doping gradients in p($g_4$2T-T):F_4TCNQ films.[53] It was demonstrated that the counterion drift was slower at low dopant concentrations where F_4TCNQ display dianion formation compared to high dopant concentration where mainly anions are formed. This suggests that the higher charge of the dianion results in stronger Coulomb binding, leading to slower drift in an applied electric field. While this stronger Coulomb binding may not be beneficial in terms of counterion drift, it may hold potential advantages in terms of dopant stability, a factor worthy of further investigation.

In future research, exploring the stability of polymer:dopant systems where multivalent counterions are formed presents an intriguing avenue. In a study by Koch et al., it was demonstrated that an n-type polymer doped with a tetrafunctional dopant, resulted in the formation of tetravalent counterions, leading to a highly stable system.[139] The stability was attributed to the strong Coulomb interaction between the dopant and the polymer, enhancing the diffusion resistance. Extending the investigation of double electron transfer, or even multiple electron transfer, to other polymer:dopant systems would provide an opportunity to explore methods for enhancing doping efficiency without increasing the number of dopant molecules. Simultaneously, it would allow for the examination of how the presence of multivalent counterions influences doping stability. This comprehensive approach could lead to valuable insights into optimizing doping processes in polymer systems while ensuring their stability under various conditions. In summary, this thesis represents a step forward in unraveling the complexities of doped polymer systems. By addressing key questions and laying the groundwork for future exploration, it contributes to the ongoing advancement of this exciting field of research.

BIBLIOGRAPHY

1. H. Shirakawa, E. J. Louis, A. G. C. MacDiarmid, Chwan K. and A. J. Heeger, *Journal of the Chemical Society, Chemical Communications*, **1977**, 16, 578-580.
2. B. Nordén and E. Krutmeijer, *Journal*, 2000.
3. OLED-info, https://www.oled-info.com/oled-lighting, (accessed 2024-02-19).
4. A. Salehi, X. Fu, D.-H. Shin and F. So, *Adv. Funct. Mater.*, **2019**, 29, 1808803.
5. A. J. Campbell, R. Rawcliffe, A. Guite, J. C. D. Faria, A. Mukherjee, M. A. McLachlan, M. Shkunov and D. D. C. Bradley, *Adv. Funct. Mater.*, **2016**, 26.
6. B. Lüssem, C.-M. Keum, D. Kasemann, B. Naab, Z. Bao and K. Leo, *Chem. Rev.*, **2016**, 116, 13714-13751.
7. A. D. Scaccabarozzi, A. Basu, F. Aniés, J. Liu, O. Zapata-Arteaga, R. Warren, Y. Firdaus, M. I. Nugraha, B.-Y. Lin, M. Campoy-Quiles, N. Koch, C. Müller, L. Tsetseris, M. Heeney and T. D. Anthopoulos, *Chem. Rev.*, **2021**, 122, 4420–4492.
8. J. Rivnay, S. Inal, A. Salleo, R. M. Owens, M. Berggren, G. G. Malliaras, J. Rivnay, S. Inal, A. Salleo, R. M. Owens, M. Berggren and G. G. Malliaras, *Nat. Rev. Mater.*, **2018**, 3, 17086.
9. O. J. Sandberg, M. Nyman, S. Dahlström, S. Sandén, B. Törngren, J.-H. Smått and R. Österbacka, *Appl. Phys. Lett.*, **2017**, 110, 153504
10. I. E. Jacobs and A. J. Moulé, *Adv. Mater.*, **2017**, 29, 1703063.
11. R. Kroon, D. A. Mengistie, D. Kiefer, J. Hynynen, J. D. Ryan, L. Yu and C. Müller, *Chem. Soc. Rev.*, **2016**, 45.
12. R. Noriega, J. Rivnay, K. Vandewal, F. P. V. Koch, N. Stingelin, P. Smith, M. F. Toney and A. Salleo, *Nat. Mater.*, **2013**, 12, 1038–1044.
13. A. Köhler and H. Bässer, *Electronic Processes in Organic Semiconductors*, Wiley-VCH, 2015.
14. A. D. McNaught and A. Wilkinson, *Journal*, DOI: 10.1351/goldbook.S05591.
15. M. C. Scharber and N. S. Sariciftci, *Adv. Mater. Technol.*, **2021**, 6, 2000857.
16. H. Arı and Z. Büyükmumcu, *Comput. Mater. Sci.*, **2017**, 138, 70-76.
17. J. L. Brédas, *J. Chem. Phys.*, **1985**, 82, 3808-3811.
18. v. Mullekom, H.A.M., Technische Universiteit Eindhoven, 2000.
19. G. F. Knoll, *Radiation Detection and Measurement* John Wiley & Sons, 2010.
20. J. Brebels, J. V. Manca, L. Lutsen, D. Vanderzande and W. Maes, *J. Mater. Chem. A*, **2017**, 5, 24037-24050.
21. W. C. Dunlap and R. L. Watters, *Physical Review*, **1953**, 92, 1396-1397.

22. H.-W. Chen, J.-H. Lee, B.-Y. Lin, S. Chen, S.-T. Wu, H.-W. Chen, J.-H. Lee, B.-Y. Lin, S. Chen and S.-T. Wu, *LSA*, **2017**, 7, 17168.

23. S. Jadoun and U. Riaz, in *Polymers for Light‐Emitting Devices and Displays*, Scrivener Publishing LLC, 2020, DOI: 10.1002/9781119654643.ch4.

24. A. R. Murad, A. Iraqi, S. B. Aziz, S. N. Abdullah and M. A. Brza, *Polymers* **2020**, 12, 2627.

25. M. Pfeiffer, K. Leo, J. Huang, M. Hofmann, A. Werner and J. Blochwitz-Nimoth, *Org. El.*, **2003**, 4, 89-103.

26. T. Sekitani, U. Zschieschang, H. Klauk, T. Someya, T. Sekitani, U. Zschieschang, H. Klauk and T. Someya, *Nat. Mater.*, **2010**, 9, 1015–1022.

27. K. Liu, B. Ouyang, X. Guo, Y. Guo and Y. Liu, *npj Flex. Electron.*, **2022**, 6.

28. C. B. Nielsen, A. Giovannitti, D.-T. Sbircea, E. Bandiello, M. R. Niazi, D. A. Hanifi, M. Sessolo, A. Amassian, G. G. Malliaras, J. Rivnay and I. McCulloch, *J. Am. Chem. Soc.*, **2016**, 138, 10252–10259.

29. B. Ding, G. Kim, Y. Kim, F. D. Eisner, E. Gutiérrez-Fernández, J. Martín, M.-H. Yoon and M. Heeney, *Angew. Chem. Int. Ed.*, **2021**, 60, 19679.

30. A. Marks, S. Griggs, N. Gasparini and M. Moser, *Adv. Mater. Interfaces*, **2022**, 9, 2102039.

31. B. D. Choudhury, B. Ibarra, F. Cesano, Y. Mao, M. N. Huda, A. R. Chowdhury, C. Olivares and M. J. Uddin, *Sol. Ener.*, **2020**, 201, 28-44.

32. E. K. Solak and E. Irmak, *RSC Adv.*, **2023**, 13, 12244-12269.

33. W. Zhao, J. Ding, Y. Zou, C.-a. Di and D. Zhu, *Chem. Soc. Rev.*, **2020**, 49, 7210-7228.

34. G.-H. Kim, L. Shao, K. Zhang, K. P. Pipe, G.-H. Kim, L. Shao, K. Zhang and K. P. Pipe, *Nat. Mater.*, **2013**, 12, 719–723.

35. J. Hynynen, D. Kiefer and C. Müller, *RSC Adv.*, **2018**, 8, 1593-1599.

36. R. Kroon, J. D. Ryan, D. Kiefer, L. Yu, J. Hynynen, E. Olsson and C. Müller, *Adv. Funct. Mater.*, **2017**, 27, 1704183.

37. J. A. Lee, A. E. Aliev, J. S. Bykova, M. J. de Andrade, D. Kim, H. J. Sim, X. Lepró, A. A. Zakhidov, J.-B. Lee, G. M. Spinks, S. Roth, S. J. Kim and R. H. Baughman, *Adv. Mater.*, **2016**, 28, 5038-5044.

38. M. Liu, X. Pu, C. Jiang, T. Liu, X. Huang, L. Chen, C. Du, J. Sun, W. Hu and Z. L. Wang, *Adv. Mater.*, **2017**, 29, 1703700.

39. W. Fan, Q. He, K. Meng, X. Tan, Z. Zhou, G. Zhang, J. Yang and Z. L. Wang, *Sci. Adv.*, **2020**, 6, eaay2840.

40. A. Lund, N. M. van der Velden, N.-K. Persson and M. M. M. Hamedi, Christian *Mater. Sci. Eng., R*, **2018**, 126, 1-29.

41. D. Yuan, W. Liu, X. Zhu, D. Yuan, W. Liu and X. Zhu, *Chem. Soc. Rev.*, **2023**, 52, 3842-3872.
42. K. Pei, *Surf. Interfaces*, **2022**, 30, 101887.
43. I. Salzmann and G. Heimel, *J. Electron Spectros. Relat. Phenomena*, **2015**, 204, 208-222.
44. G. Hong, X. Gan, C. Leonhardt, Z. Zhang, J. Seibert, J. M. Busch and S. Bräse, *Adv. Mater.*, **2021**, 33, 2005630.
45. J. Yi, G. Zhang, H. Yu, H. Yan, J. Yi, G. Zhang, H. Yu and H. Yan, *Nat. Rev. Mater.*, **2023**, 9, 46–62.
46. J. Yu, Y. Zheng, J. Huang, J. Yu, Y. Zheng and J. Huang, *Polymers* **2014**, 6, 2473-2509.
47. T. P. Le, Z. Shang, L. Wang, N. Li, S. V. Kesava, J. W. O'Connor, Y. Chang, C. Bae, C. Zhu, A. Hexemer, E. W. Gomez, A. Salleo, M. A. Hickner and E. D. Gomez, *Macromolecules*, **2015**, 48, 5162–5171.
48. B. Kippelen and J.-L. Brédas, *Energy Environ. Sci.*, **2009**, 2, 251-261.
49. Y. Firdaus, V. M. Le Corre, J. I. Khan, Z. Kan, F. Laquai, P. M. Beaujuge and T. D. Anthopoulos, *Adv. Sci.*, **2019**, 6, 1802028.
50. R. G. Khanapure, A. A. Ghanwat, S. K. Awate, U. S.Gawali, R. J. Kavade, P. H. Salunkhe and S. V. Patil, *Polym. Bull.* , **2022**, 80, 3183–3195.
51. D. Scheunemann, E. Järsvall, J. Liu, D. Beretta, S. Fabiano, M. Caironi, M. Kemerink and C. Müller, *Chem. Phys. Rev.*, **2022**, 3, 021309
52. M. Craighero, J. Guo, S. Zokaei, S. Griggs, J. Tian, J. Asatryan, J. Kimpel, R. Kroon, K. Xu, J. S. Reparaz, J. Martín, I. McCulloch, M. Campoy-Quiles and C. Müller, *ACS Appl. Electron. Mater.*, **2023**, XXXX, XXX-XXX.
53. J. Liu, M. Craighero, V. K. Gupta, D. Scheunemann, S. H. K. Paleti, E. Järsvall, Y. Kim, K. Xu, J. S. Reparaz, L. J. A. Koster, M. Campoy-Quiles, M. Kemerink, A. Martinelli and C. Müller, *Adv. Funct. Mater.*, **2024**, DOI: 10.1002/adfm.202312549, 2312549.
54. B. Russ, A. Glaudell, J. J. Urban, M. L. Chabinyc and R. A. Segalman, *Nat. Rev. Mater.*, **2016**, 1, 16050.
55. J. Liu, B. van der Zee, R. Alessandri, S. Sami, J. Dong, M. I. Nugraha, A. J. Barker, S. Rousseva, L. Qiu, X. Qiu, N. Klasen, R. C. Chiechi, D. Baran, M. Caironi, T. D. Anthopoulos, G. Portale, R. W. A. Havenith, S. J. Marrink, J. C. Hummelen and L. J. A. Koster, *Nat. Commun.*, **2020**, 11, 5694.
56. S. Chen and M. P. Jonsson, *ACS Photonics*, **2023**, 10, 571–581.
57. M. Massetti, F. Jiao, A. J. Ferguson, D. Zhao, K. Wijeratne, A. Würger, J. L. Blackburn, X. Crispin and S. Fabiano, *Chem. Rev.*, **2021**, 121, 12465–12547.
58. D. Beretta, N. Neophytou, J. M. Hodges, M. G. Kanatzidis, D. Narducci, M. Martin- Gonzalez, M. Beekman, B. Balke, G. Cerretti, W. Tremel, A. Zevalkink, A. I. Hofmann, C. Müller, B. Dörling, M. Campoy-Quiles and M. Caironi, *Mater. Sci. Eng R Rep.*, **2019**, 138, 100501.

59. I. Salzmann, G. Heimel, M. Oehzelt, S. Winkler and N. Koch, *Acc. Chem. Res.*, **2016**, 49, 370–378.

60. B. Yurash, D. X. Cao, V. V. Brus, D. Leifert, M. Wang, A. Dixon, M. Seifrid, A. E. Mansour, D. Lungwitz, T. Liu, P. J. Santiago, K. R. Graham, N. Koch, G. C. Bazan and T.-Q. Nguyen, *Nat. Mater.* , **2019**, 18, 1327–1334.

61. R. J. Mammone and A. G. MacDiarmid, *J. Chem. Soc., Faraday Trans. 1*, **1985**, 81, 105-112.

62. C. C. Han and R. L. Elsenbaumer, *Synthetic Metals*, **1989**, 30, 123-131.

63. M. Goel, M. Siegert, G. Krauss, J. Mohanraj, A. Hochgesang, D. C. Heinrich, M. Fried, J. Pflaum and M. Thelakkat, *Adv. Mater.*, **2020**, 32, 2003596.

64. A. I. Hofmann, R. Kroon, S. Zokaei, E. Järsvall, C. Malacrida, S. Ludwigs, T. Biskup and C. Müller, *Adv. Electron. Mater.*, **2020**, 6, 2000249.

65. D. Kiefer, R. Kroon, A. I. Hofmann, H. Sun, X. Liu, A. Giovannitti, D. Stegerer, A. Cano, J. Hynynen, L. Yu, Y. Zhang, D. Nai, T. F. Harrelson, M. Sommer, A. J. Moulé, M. Kemerink, S. R. Marder, I. McCulloch, M. Fahlman, S. Fabiano and C. Müller, *Nat. Mater.*, **2019**, 18, 149–155.

66. W. C. Tsoi, S. J. Spencer, L. Yang, A. M. Ballantyne, P. G. Nicholson, A. Turnbull, A. G. Shard, C. E. Murphy, D. D. C. Bradley, J. Nelson and J.-S. Kim, *Macromolecules*, **2011**, 44, 2944–2952.

67. M. Arvind, C. E. Tait, M. Guerrini, J. Krumland, A. M. Valencia, C. Cocchi, A. E. Mansour, N. Koch, S. Barlow, S. R. Marder, J. Behrends and D. Neher, *J. Phys. Chem. B*, **2020**, 124, 7694-7708.

68. I. E. Jacobs, C. Cendra, T. F. Harrelson, Z. I. Bedolla Valdez, R. Faller, A. Salleo and A. J. Moulé, *Mater. Horiz.*, **2018**, 5, 655-660.

69. A. E. Mansour, R. Warren, D. Lungwitz, M. Forster, U. Scherf, A. Opitz, M. Malischewski and N. Koch, *ACS Appl. Mater. Interfaces*, **2023**, 15, 46148–46156.

70. D. Tsokkou, P. Cavassin, G. Rebetez and N. Banerji, *Mater. Horiz.*, **2022**, 9, 482-491.

71. M. G. Voss, D. T. Scholes, J. R. Challa and B. J. Schwartz, *Faraday Discuss.*, **2019**, 216, 339-362.

72. D. Tsokkou, C.-Y. Cheng, N. Krainova, S. Mukhopadhyay, N. C. Giebink and N. Banerji, *J. Phys. Chem. C*, **2021**, 125, 7086–7096.

73. K. H. Chan and S.-K. So, *JPE*, **2011**, 1, 011112.

74. N. D. Nguyen, M. Schmeits and H. P. Loebl, *Phys. Rev. B*, **2007**, 75, 075307.

75. M. Schmeits, *J. Appl. Phys.*, **2007**, 101, 084508.

76. Z. Ge, L. Wang, D. Gu and T. Zhang, *Org. Electron.*, **2024**, 126, 106996.

77. H. T. Yi, Y. N. Gartstein, V. Podzorov, H. T. Yi, Y. N. Gartstein and V. Podzorov, *Sci. Rep.* , **2016**, 6, 23650.

78. S. W. Tsang, S. K. So and J. B. Xu, *J. Appl. Phys.*, **2006**, 99, 013706.

79. M. L. Tietze, J. Benduhn, P. Pahner, B. Nell, M. Schwarze, H. Kleemann, M. Krammer, K. Zojer, K. Vandewal, K. Leo, M. L. Tietze, J. Benduhn, P. Pahner, B. Nell, M. Schwarze, H. Kleemann, M. Krammer, K. Zojer, K. Vandewal and K. Leo, *Nat. Commun.*, **2018**, 9, 1182.
80. S. Winkler, P. Amsalem, J. Frisch, M. Oehzelt, G. Heimel and N. Koch, *Mater. Horiz.*, **2015**, 2, 427-433.
81. G. Heimel, *ACS Cent. Sci.*, **2016**, 2, 309–315.
82. R. Warren, E. Cho, H. Li, J.-L. Bredas and N. Koch, *ACS Materials Lett.*, **2022**, 4, 2051–2057.
83. T. L. Murrey, M. Berteau-Rainville, G. Gonel, J. Saska, N. E. Shevchenko, A. S. Fergerson, R. M. Talbot, N. L. Yacoub, F. Zhang, A. Kahn, M. Mascal, I. Salzmann and A. J. Moulé, *J. Mater. Chem. C*, **2023**, 11, 14884-14895.
84. M. G. Voss, J. R. Challa, D. T. Scholes, P. Y. Yee, E. C. Wu, X. Liu, S. J. Park, O. L. Ruiz, S. Subramaniyan, M. Chen, S. A. Jenekhe, X. Wang, S. H. Tolbert and B. J. Schwartz, *Adv. Mater.*, **2021**, 33, 2000228.
85. M. B. Qarai, R. Ghosh and F. C. Spano, *J. Phys. Chem. C*, **2021**, 125, 24487–24497.
86. A. J. Moulé, G. Gonel, T. L. Murrey, R. Ghosh, J. Saska, N. E. Shevchenko, I. Denti, A. S. Fergerson, R. M. Talbot, N. L. Yacoub, M. Mascal, A. Salleo and F. C. Spano, *Adv. Electron. Mater.*, **2022**, 8, 2100888.
87. P. Cavassin, I. Holzer, D. Tsokkou, O. Bardagot, J. Réhault and N. Banerji, *Adv. Mater.*, **2023**, 35, 2300308.
88. O. Bardagot and N. Banerji, *Chimia*, **2022**, 76.
89. C. Enengl, S. Enengl, S. Pluczyk, M. Havlicek, M. Lapkowski, H. Neugebauer and E. Ehrenfreund, *Chem. Phys. Chem.*, **2016**, 17, 1439-4235.
90. G. Krauss, A. Hochgesang, J. Mohanraj and M. Thelakkat, *Macromol. Rapid Commun.*, **2021**, 42, 2100443.
91. M. Lögdlund, R. Lazzaroni, S. Stafström, W. R. Salaneck and J.-L. Brédas, *Phys. Rev. Lett.*, **1989**, 63, 1841-1844.
92. X. Lin, G. E. Purdum, Y. Zhang, S. Barlow, S. R. Marder, Y.-L. Loo and A. Kahn, *Chem. Mater.*, **2016**, 28, 2677–2684.
93. C. Gaul, S. Hutsch, M. Schwarze, K. S. Schellhammer, F. Bussolotti, S. Kera, G. Cuniberti, K. Leo and F. Ortmann, *Nat. Mater.*, **2018**, 17, 439–444.
94. K. Xu, H. Sun, T.-P. Ruoko, G. Wang, R. Kroon, N. B. Kolhe, Y. Puttisong, X. Liu, D. Fazzi, K. Shibata, C.-Y. Yang, N. Sun, G. Persson, A. B. Yankovich, E. Olsson, H. Yoshida, W. M. Chen, M. Fahlman, M. Kemerink, S. A. Jenekhe, C. Müller, M. Berggren and S. Fabiano, *Nat. Mater.*, **2020**, 19, 738-744.

95. D. Kim and I. Zozoulenko, *The Journal of Physical Chemistry B*, **2019**, 123, 5160-5167.

96. V. Untilova, J. Hynynen, A. I. Hofmann, D. Scheunemann, Y. Zhang, S. Barlow, M. Kemerink, S. R. Marder, L. Biniek, C. Müller and M. Brinkmann, *Macromolecules*, **2020**, 53, 6314–6321.

97. J. Liu, L. Qiu, R. Alessandri, X. Qiu, G. Portale, J. Dong, W. Talsma, G. Ye, A. A. Sengrian, P. C. T. Souza, M. A. Loi, R. C. Chiechi, S. J. Marrink, J. C. Hummelen and L. J. A. Koster, *Adv. Mater.*, **2018**, 30, 1704630.

98. A. I. Hofmann, R. Kroon, L. Yu and C. Müller, *J. Mater. Chem. C*, **2018**, 6, 6905-6910.

99. P. Y. Yee, D. T. Scholes, B. J. Schwartz and S. H. Tolbert, *J. Phys. Chem. Lett.*, **2019**, 10, 4929–4934.

100. S. Hultmark, M. Craighero, S. Zokaei, D. Kim, E. Järsvall, F. Farooqi, S. Marina, R. Kroon, J. Martin, I. Zozoulenko and C. Müller, *J. Mater. Chem. C*, **2023**, 11, 8091-8099.

101. S. Zokaei, D. Kim, E. Järsvall, A. M. Fenton, A. R. Weisen, S. Hultmark, P. H. Nguyen, A. M. Matheson, A. Lund, R. Kroon, M. L. Chabinyc, E. D. Gomez, I. Zozoulenko and C. Müller, *Mater. Horiz.*, **2022**, 9, 433-443.

102. T. L. Murrey, M. A. Riley, G. Gonel, D. D. Antonio, L. Filardi, N. Shevchenko, M. Mascal and A. J. Moulé, *J. Phys. Chem. Lett.*, **2021**, 12, 1284-1289.

103. D. Yuan, E. Plunkett, P. H. Nguyen, D. Rawlings, M. L. Le, R. Kroon, C. Müller, R. A. Segalman and M. L. Chabinyc, *Adv. Func. Mater.*, **2023**, 33, 2300934.

104. Y. Yamashita, J. Tsurumi, M. Ohno, R. Fujimoto, S. Kumagai, T. Kurosawa, T. Okamoto, J. Takeya, S. Watanabe, Y. Yamashita, J. Tsurumi, M. Ohno, R. Fujimoto, S. Kumagai, T. Kurosawa, T. Okamoto, J. Takeya and S. Watanabe, *Nature* **2019**, 572, 634–638

105. S. Olthof, S. Mehraeen, S. K. Mohapatra, S. Barlow, V. Coropceanu, J.-L. Brédas, S. R. Marder and A. Kahn, *Phys. Rev. Lett.*, **2012**, 109, 176601.

106. M. Schwarze, C. Gaul, R. Scholz, F. Bussolotti, A. Hofacker, K. S. Schellhammer, B. Nell, B. D. Naab, Z. Bao, D. Spoltore, K. Vandewal, J. Widmer, S. Kera, N. Ueno, F. Ortmann and K. Leo, *Nat. Mater.*, **2019**, 18, 242–248.

107. M. Koopmans, M. A. T. Leiviskä, J. Liu, J. Dong, L. Qiu, J. C. Hummelen, G. Portale, M. C. Heiber and L. J. A. Koster, *ACS Appl. Mater. Interfaces*, **2020**, 12, 56222–56230.

108. D. Derewjanko, D. Scheunemann, E. Järsvall, A. I. Hofmann, C. Müller and M. Kemerink, *Adv. Funct. Mater.*, **2022**, 32, 2112262.

109. J. M. Winfield, C. L. Donley and J.-S. Kim, *J. Appl. Phys.*, **2007**, 102, 063505.

110. M. Campoy-Quiles, P. G. Etchegoin and D. D. C. Bradley, *Phys. Rev. B*, **2005**, 72, 045209.

111. I. E. Jacobs, E. W. Aasen, J. L. Oliveira, T. N. Fonseca, J. D. Roehling, J. Li, G. Zhang, M. P. Augustine, M. Mascal and A. J. Moulé, *J. Mater. Chem. C*, **2016**, 4, 3454-3466.

112. A. Carrington and A. D. MacLachlan, *Introduction to Magnetic Resonance: With Applications to Chemistry and Chemical Physics*, Harper & Row, 1969.
113. N. M. Atherton, *Principles of Electron Spin Resonance*, Ellis Horwood, 1993.
114. J. A. Weil and J. R. Bolton, *Electron Paramagnetic Resonance: Elementary Theory and Practical Applications*, John Wiley & Sons, 2007.
115. M. Brustolon and E. Giamello, *Electron Paramagnetic Resonance: A Practitioners Toolkit*, John Wiley & Sons, 2009.
116. V. Chechik, E. Carter and D. Murphy, *Electron Paramagnetic Resonance*, Oxford University Press, 2016.
117. D. Goldfarb and S. Stoll, *EPR Spectroscopy: Fundamentals and Methods*, John Wiley & Sons, 2018.
118. E. Duin, Electron Paramagnetic Resonance Theory, https://webhome.auburn.edu/~duinedu/epr/1_theory.pdf, (accessed 2024-02-20).
119. T. Biskup, *Front. Chem.*, **2019**, 7.
120. T. Biskup, *Appl. Phys. Lett.*, **2021**, 119, 010503
121. G. R. Eaton, S. S. Eaton, D. P. Barr and R. T. Weber, *Quantitative EPR*, Springer Vienna, 1 edn., 2010.
122. C. L. Brosseau, A. Colina, J. V. Perales-Rondon, A. J. Wilson, P. B. Joshi, B. Ren and X. Wang, *Nat. Rev. Methods Primers*, **2023**, 3.
123. I. Sahalianov, J. Hynynen, S. Barlow, S. R. Marder, C. Müller and I. Zozoulenko, *J. Phys. Chem. B*, **2020**, 124, 11280–11293.
124. S. Zokaei, R. Kroon, J. Gladisch, B. D. Paulsen, W. Sohn, A. I. Hofmann, G. Persson, A. Stamm, P.-O. Syrén, E. Olsson, J. Rivnay, E. Stavrinidou, A. Lund and C. Müller, *Adv. Sci.*, **2021**, 8, 2002778.
125. J. Moulton and P. Smith, *Synth. Met.*, **1991**, 40, 13-22.
126. J. Moulton and P. Smith, *Polymer*, **1992**, 33, 2340-2347.
127. L. Pan, A. Chortos, G. Yu, Y. Wang, S. Isaacson, R. Allen, Y. Shi, R. Dauskardt, Z. Bao, L. Pan, A. Chortos, G. Yu, Y. Wang, S. Isaacson, R. Allen, Y. Shi, R. Dauskardt and Z. Bao, *Nat. Commun.*, **2014**, 5, 3002.
128. S. Ghosh, J. Rasmusson and O. Inganäs, *Adv. Mater.*, **1998**, 10, 1097-1099.
129. P. Murray, G. M. Spinks, G. G. Wallace and R. P. Burford, *Synth. Met.*, **1998**, 97, 117-121.
130. R. Kroon, D. Kiefer, D. Stegerer, L. Yu, M. Sommer and C. Müller, *Adv. Mater.*, **2017**, 29, 1700930.

131. E. Järsvall, T. Biskup, Y. Zhang, R. Kroon, S. Barlow, S. R. Marder and C. Müller, *Chem. Mater.*, **2022**, 34, 5673-5679.

132. S. A. Paniagua, J. Baltazar, H. Sojoudi, S. K. Mohapatra, S. Zhang, C. L. Henderson, S. Graham, S. Barlow and S. R. Marder, *Mater. Horiz.*, **2014**, 1, 111-115.

133. S. K. Mohapatra, Y. Zhang, B. Sandhu, M. S. Fonari, T. V. Timofeeva, S. R. Marder and S. Barlow, *Polyhedron*, **2016**, 116, 88-95.

134. J. Hynynen, D. Kiefer, L. Yu, R. Kroon, R. Munir, A. Amassian, M. Kemerink and C. Müller, *Macromolecules*, **2017**, 50, 8140-8148.

135. E. Lim, K. A. Peterson, G. M. Su and M. L. Chabinyc, *Chem. Mater.*, **2018**, 30, 998-1010.

136. H. Méndez, G. Heimel, S. Winkler, J. Frisch, A. Opitz, K. Sauer, B. Wegner, M. Oehzelt, C. Röthel, S. Duhm, D. Többens, N. Koch and I. Salzmann, *Nat. Commun.*, **2015**, 6, 8560.

137. D. T. Scholes, P. Y. Yee, J. R. Lindemuth, H. Kang, J. Onorato, R. Ghosh, C. K. Luscombe, F. C. Spano, S. H. Tolbert and B. J. Schwartz, *Adv. Funct. Mater.*, **2017**, 27, 1702654.

138. K. E. Watts, B. Neelamraju, E. L. Ratcliff and J. E. Pemberton, *Chemistry of Materials*, **2019**, 31, 6986-6994.

139. F. Saeedifard, D. Lungwitz, Z.-D. Yu, S. Schneider, A. E. Mansour, A. Opitz, S. Barlow, M. F. Toney, J. Pei, N. Koch and S. R. Marder, *ACS Appl. Mater. Interfaces*, **2022**, 14, 33598–33605.